

**LABORATORY AND FIELD CHARACTERIZATION OF
HYDRATE BEARING SEDIMENTS - IMPLICATIONS**

A Thesis
Presented to
The Academic Faculty

by

Marco Terzariol

In Partial Fulfillment
of the Requirements for the Degree
Doctor of Philosophy in the
School of Civil and Environmental Engineering

Georgia Institute of Technology
May 2015

COPYRIGHT © 2015 BY MARCO TERZARIOL

**LABORATORY AND FIELD CHARACTERIZATION OF
HYDRATE BEARING SEDIMENTS - IMPLICATIONS**

Approved by:

Dr. J. Carlos Santamarina, Advisor
School of Civil and Environmental
Engineering
Georgia Institute of Technology

Dr. J. David Frost
School of Civil and Environmental
Engineering
Georgia Institute of Technology

Dr. Paul W. Mayne
School of Civil and Environmental
Engineering
Georgia Institute of Technology

Dr. Robert C. Bachus
Geosyntec Consultants / CEE
Georgia Institute of Technology

Dr. Guillermo H. Goldsztein
School of Mathematics
Georgia Institute of Technology

Date Approved: Dec. 10th 2014

[To freethinking]

ACKNOWLEDGEMENTS

I would like to thank my advisor, Dr. Santamarina, for the opportunity to work and study in his group. His patience, dedication and insightful comments were the keystone for the success of this thesis. Also, I would like to thank to my thesis committee: Dr. Frost, Dr. Mayne, Dr. Bachus and Dr. Goldsztein for their comments, suggestions and exceptional courses taught at Georgia Tech.

I want to express my gratitude to the PMRL current and former students for their support and discussions that enriched this thesis: Cesar Pasten, Jaewong Jang, D. Nicolas Espinoza, Minsu Cha, Aswathy Sivaram, Sheng Dai, Seunghee Kim, Song hun Chong, Junbong Jang, Shahrazad Roshankhah, Efthymios Papadopoulos, Liang Lei, Seth Mallett, Junghee Park, Zhonghao Sun, Qi Liu, Adrian Garcia, Yuanjie Shen, Antonella Ungari, Nicolas Ausburger and David Rhodes. Also, PMRL visitors: William Waite, Bill Winters, Alessio Savioli, Norimasa Yoshimoto, Xingwei Ren, Stefanos Athanasopoulos, Lucio Cruz, Enrique Asanza Izquierdo, Miriam Martin-Ruiz and Charles Leigh.

Personal friends and colleagues, thanks for their support and long discussions: Matthieu C. Leibovici, Chloe A. Fabien, Remi Chou, Spyridon Pavlidis, Stef Alexopoulos, Katie Taladay, Alejandro Martinez, David Manuel Gutierrez Estevez, Nortey Yeboah, Nicole Caruso, Xenia Wirth, Cameron Troxel, Joshua Mendez and Randy Pettyjohn; and Civil and Environmental Engineering staff: Andy Udell, Crystal Hanson, Lisa Tuttle, Jenny Eaton and Carol Maddox.

Thanks to my family, for they made all this possible: Roberto Enrique Terzariol, Viviana Lilia Rodriguez, Luca Terzariol and Marina Terzariol.

TABLE OF CONTENTS

	Page
ACKNOWLEDGEMENTS	IV
LIST OF TABLES	X
LIST OF FIGURES	XI
SUMMARY	XIX
 <u>CHAPTER</u>	
1 CHAPTER 1: INTRODUCTION	1
1.1 Methane Hydrate Bearing Sediments	1
1.2 Energy Geo-technology	2
1.3 Reservoir Characterization	3
1.4 Thesis Organization	5
2 CHAPTER 2: SAMPLING LIMITATIONS DURING PRESSURE CORING	7
2.1 Introduction	7
2.2 Literature Review	7
2.2.1 Plugging	9
2.2.2 Sampler Dimensions Effect	11
2.3 Pressure Coring	13
2.4 Coring Disturbances	16
2.4.1 Cemented Soils: Radial Expansion	16
2.4.2 Non-cemented Soils: Plugging	19
2.5 Guidelines for Coring and Sampling Tool Design	22
2.5.1 Optimal Gap	22
2.5.2 Maximum Recoverable Length (un-cemented sediments)	24

2.6	Experimental Study	25
2.7	Conclusions	28
3	CHAPTER 3: PRESSURE CORE CHARACTERIZATION TOOLS FOR HYDRATE-BEARING SEDIMENTS	29
3.1	Introduction	29
3.2	Pressure Core Technology: Overview	30
3.3	Pressure Core Characterization Tools	31
3.3.1	Manipulator (MAN)	32
3.3.2	Sub-sampling (CUT)	34
3.3.3	Instrumented Pressure Testing Chamber (IPTC)	34
3.3.4	Effective Stress Chamber (ESC)	35
3.3.5	Direct Shear Chamber (DSC)	36
3.3.6	Sub-sampling Tool for Bio-Studies (BIO)	37
3.3.7	Controlled Depressurization Chamber (CDC)	37
3.4	Measurements of Physical Properties	38
3.4.1	Tool Position Control	38
3.4.2	Sensors	39
3.5	Monitoring Dissociation – Gas Production	40
3.6	Discussion: Comprehensive Characterization Approach	41
3.7	Conclusions	43
4	CHAPTER 4: PHYSICAL PROPERTIES OF METHANE HYDRATE BEARING SEDIMENTS: NANKAI TROUGH DEPLOYMENT	44
4.1	Introduction	44
4.2	Direct Shear Chamber: Design	45
4.2.1	Design	45
4.2.2	Calibration	47

4.3 Experimental Study: Nankai Trough	48
4.3.1 Procedure	48
4.3.2 Specimens	49
4.3. Test Sequence	51
4.4 Results	52
4.4.1 Methane Hydrate Bearing Sediments	53
4.4.1.1 Shear Strength	53
4.4.1.2 P-waves	54
4.4.1.3 Relaxation Test	56
4.4.2 Methane Gas Dissociation	58
4.4.3 Post Dissociation Sediments Response	59
4.4.3.1 Shear Strength	59
4.4.3.1 Compressibility	60
4.4.4 Summary	61
4.5 Discussion: Comparison with Published Data	63
4.6 Conclusions	64
5 CHAPTER 5: BOREHOLE TOOL FOR THE COMPREHENSIVE CHARACTERIZATION OF HYDRATE BEARING SEDIMENTS	66
5.1 Introduction	66
5.2 Offshore Exploration – Current Technology	66
5.2.1 Remotely Operated Vehicles ROVs	67
5.2.2 Dragged Devices	69
5.2.3 Wireline Logging and Borehole Operations	69
5.2.4 Penetrometers	72
5.3 Design of an In-situ Tool for Hydrate Bearing Sediments Characterization	76

5.3.1	Tip Module: Insertion Forces and Temperature	82
5.3.1.1	Design	82
5.3.1.2	Mechanical Verification	83
5.3.1.3	Calibration	84
5.3.2	Hydraulic Cond., Fluid Sampler and Mini Production Test	86
5.3.2.1	Design	86
5.3.2.2	Verification	88
5.3.2.3	Calibration	90
5.3.3	Electrical Resistivity	92
5.3.3.1	Design	92
5.3.3.2	Calibration	93
5.3.4	Sediment Sampling	93
5.3.4.1	Design	93
5.3.4.2	Field Verification	94
5.4	Future Modules	94
5.4.1	Thermal Conductivity, Stiffness, Video and Frictional Sleeve	94
5.5	Conclusions	97
6	CHAPTER 6: MAXIMUM RECOVERABLE GAS FROM HYDRATE BEARING SEDIMENTS	98
6.1	Introduction	98
6.2	Analytical Solution	104
6.2.1	Thin or Deep Reservoir Condition	105
6.2.2	Homogeneous Formation: Spherical Flow Condition	105
6.2.3	Layered Formation: Axisymm. Flow with Leak-in Condition	108
6.3	Discussion	113
6.4	Recoverable Gas: Energy	114

6.5 Comparison with Literature	116
6.6 Discussion: Real Case Scenario	119
6.7 Conclusions	121
7 CHAPTER 7: CONCLUSIONS	122
REFERENCES	125

LIST OF TABLES

		Page
Table 2.1	Specific recovery ratio	10
Table 2.2	Typical drill bit dimensions for currently available coring techniques for bottom hole sampling (from Kubo et al., 2014; Peuchen, 2007; Kolk and Wegerif, 2005; Kawasaki et al., 2006; iodp.org; Huey, 2009; Zhu et al. 2013; Fugro.com)	14
Table 4.1	Summary of results gathered using the direct shear chamber DSC	62
Table 5.1	Selected ROVs (Note: additional information in: www.marum.de)	68
Table 5.2	Summary of available information for scientific cruises (iodp.ldeo.columbia.edu)	70
Table 5.3	Full flow penetrometers (Randolph 2012; Lunne et al. 2011)	73
Table 5.4	Evolution in Cone Penetration Test CPT developed for marine sediment characterization (modified and updated from Boggess and Robertson, 2011; Lunne, 2010 and Peuchen, 2013)	74
Table 5.5	Critical parameters needed for the engineering of gas hydrate production from hydrate bearing sediments.	77
Table 6.1	Selected reservoirs gas volume estimation.	99
Table 6.2	Well tests summary in chronological order	100
Table 6.3	Summary of selected parameter used in numerical simulations	102
Table 6.4	Profit analysis	115
Table 6.5	Data input for equations for selected cases	117
Table 6.6	Summary of parameters for the example in Figure 6.9	120

LIST OF FIGURES

	Page	
Figure 1.1	Natural methane hydrate systems: Methane hydrate stability zone thickness in marine sediments (Piñero et al., 2013).	1
Figure 1.2	Phase boundaries for methane hydrate and ice (Sloan and Koh 2007).	2
Figure 1.3	Energy geo-technology: (a) Energy and quality of life (Pasten and Santamarina, 2011). (b) Energy use per capita. (c) Energy consumption (data from World Bank, 2013). Note: Fossil fuel = coal, oil, petroleum and gas products; Alternative = non-carbohydrate energy (hydropower and nuclear, geothermal and solar); Renewable = solid and liquid biomass, biogas, industrial waste and municipal waste.	3
Figure 1.4	Hydrate Bearing Sediments: Geotechnical implications and impact. (a) Production implications. (b) Environmental impact.	4
Figure 1.5	Comprehensive characterization of methane hydrate bearing sediments.	5
Figure 2.1	Ideal sampling: Point A is in-situ state of stress, B is the isotropic state of stress (modified from Baligh et al., 1987).	8
Figure 2.2	Sampler diameters and definitions.	11
Figure 2.3	Pressure corers: (a) Fugro Pressure Corer and HYACE (modified from Peuchen, 2007; Kolk and Wegerif, 2005; iodp.org). (b) Typical cross section of a drilling bit for: cutting shoe and face bit type.	13
Figure 2.4	Typical X-ray images from the pressure cores recovered at the Nankai Trough, Japan (with permission JOGMEC). Samples were obtained using a 53.6mm (ID) liner and 51.4mm cutting shoe (JOGMEC corer).	15
Figure 2.5	Soil expansion due to confinement release.	16

Figure 2.6	General geometry for the analysis of the sampler-soil interaction. (a) General solution. (b) Soil expansion against the sampler.	17
Figure 2.7	Non-cemented soils: Forces involved in plugging.	20
Figure 2.8	Interface interaction coefficient β .	22
Figure 2.9	Optimal gap: Design chart for a linear elastic soil.	23
Figure 2.10	Example of a plastic liner sampler computation for a frictional soil for the case of hydrate bearing sediments in Nankai Trough. Insert: large scale to accommodate soil and sampler behavior.	24
Figure 2.11	Maximum expected recoverable core length: Design chart for frictional soil.	25
Figure 2.12	Core recovery with small sampler – Field study: (a) Continuous push schematics. (b) Dynamic driving. (c) Picture at the site. (d) Samplers dimensions.	26
Figure 2.13	Core recovery with small sampler – Results: (a) Sampled length (distance measured before removing the sampler from the ground). (b) Penetration force vs. depth. There is no clear evidence of significant differences between the two samplers.	27
Figure 3.1	Pressure core manipulation. (a) The manipulator MAN couples with the storage chamber and fluid pressures are equalized at the target pressure p_0 before opening the ball valve. (b) The manipulator captures the core and transfers it into the temporary storage chamber. (c) Ball valves are closed and the depressurized storage chamber is separated. (d) The selected characterization tool is coupled to the manipulator and is pressurized to p_0 . (e) Ball valves are opened and the core is pushed into the characterization tool; stand-alone characterization tools may be detached after retrieving the rest of the core and closing valves. Note: the cutter tool CUT is shown in panes d&e; it is attached in series to cut core to any desired length to meet tool requirements (for stand-alone ESC, DSC, CDP, and Bio tools).	33
Figure 3.2	Schematic diagrams of characterization chambers. (a) IPTC instrumented pressure testing chamber with P-T	34

control. (b) ESC effective stress chamber with σ' -P-T control. (c) DSC direct shear chamber with σ' - τ -P-T control. (d) CDP controlled depressurization chamber for sediment preservation and gas production. (e) BIO sampler for multiple bio-reactor chambers. Scale: the outside diameter of the large ball valve shown in all devices is OD = 220 mm.

- Figure 3.3 Tool Control. The displacement of sensors, subsampling tools and drills are controlled under pressure using a screw-based positioning system where the driver advances along the threaded guide while pushing the tool rod (shown in green). Transducers at the tip of the rod are wired through the central hole in the tool rod. 39
- Figure 3.4 Measurement tools and sensors. (a) Bender elements for S-wave generation and detection. (b) Piezocrystals for P-waves. (c) Penetrometer for strength measurement. (d) Pore fluid sampler. (e) Electrical needle probe for resistivity profiling. (f) Thermocouple instrumented tip. (g) Strain gauge for thermal conductivity determination (TPS – NETL; Rosenbaum et al. (2007)). 39
- Figure 3.5 Monitored gas production tests using IPTC: (a) Evolutions of pressure, temperature, electrical resistivity, and produced gas (Krishna-Godavari Basin, Yun et al. 2010); Typical wave signatures during gas production: P-wave signatures eventually fade out after gas production; S-waves detect the evolution of the skeleton shear stiffness during hydrate dissociation and gas production (Ulleung Basin, Yun et al. 2011). 41
- Figure 4.1 Direct Shear Chamber DSC. (a) Cross section. (b) Picture of the vertical plunger and the cap. (c) Transducers, internal ring and specimen. 46
- Figure 4.2 Instrumentation in the DSC. The same power supply is used for the LVDTs, load cells and pressure transducer (shared the ground). The datalogger reads output values which are stored in the computer. 47
- Figure 4.3 Calibration of the direct shear chamber DSC. (a) Typical shear test conducted on dry sand. (b) Typical LVDT calibration showing linear relationship and range of application. (c) Effective stress applied to the sample for each reading of the vertical load cell, with respect to water 48

pressure. Chamber capacity is also shown. (d) Leak test: minor leakage is common as reflected in this response vs. time for a water saturated DSC (Note: this depressurization rate may also reflect early dissolution of trapped gas bubbles).

Figure 4.4	Nankai Trough: location, hydrate saturation, coring interval and reservoir characteristics (after Fujii et al. 2013). Note: mbsl = meters below sea level.	50
Figure 4.5	X-ray images of tested specimens and properties.	51
Figure 4.6	Evolution of specimen vertical displacement during the complete loading history for core 20P. Sample initial length = 160 mm.	52
Figure 4.7	Hydrate bearing sediment shear test for the core 20P. The system is left to relax for each millimeter of imposed displacement. Shear strengths values, before and after relaxation are readily seen.	53
Figure 4.8	Shear test results for core 20P. (a) Shear stress vs. displacement. (b) Mobilized friction angle vs. displacement (assuming cohesion = 0).	54
Figure 4.9	P-wave monitoring results for hydrate bearing sediments under different applied vertical effective stress σ'_z for the hydrate bearing sample 10P. (a) P-wave signature cascade and trigger signal during loading. (b) P-wave velocities.	55
Figure 4.10	Relaxation test for the hydrate bearing sample 20P. (a) Measured stress and displacement. (b) Best match. The insert shows the first load response.	57
Figure 4.11	Dissociation test for core 20P under effective stress $\sigma'_v = 3$ MPa. (a) Flow control procedure. The ISCO pump extracts water at a constant rate of 60 ml/min, and the chamber pressure. Pressure and temperature are monitored at all times. (b) Pressure drop and volume contraction vs. time for the two systems: pressure control and flow control. (c) Dissociation test in PT space: hydrate stability boundaries in salt water and fresh water are shown for reference.	58
Figure 4.12	Shear test after dissociation for core 20P. (a) Shear test vs. displacement. (b) Mobilized friction angle vs.	60

displacement (assuming cohesion = 0).

Figure 4.13	Compressibility test after dissociation for core 20P. Data show a pre-consolidation stress of 3 MPa since during dissociation it was loaded to that effective stress.	61
Figure 4.14	Compilation of shear tests with and without hydrates on marine sediments of Nankai Trough for the sample 20P. Triangles represent peak values while squares are residual values. Red dots corresponds to the pre-relaxation behavior and green dots are for post-relaxation. Insert: hydrate bearing sediments shear strength.	62
Figure 4.15	Comparison with published data. (a) P-wave velocity gathered from DSC is shown in a thick black line while the logging while drilling data is grey from Matsumoto et al. (2004). (b) Shear strength values from this study are shown in a thick black line. Diamonds represents 1 MPa in confining stress, while squares and triangles are the markers for 3 and 5 MPa. Empty markers are for the case of Nankai Trough bearing sand and methane hydrate; filled markers for toyoura sand and methane hydrate. Shear strength from the literature was computed as half of the maximum deviatoric stress. Data compiled from (Hyodo et al. 2011; Miyazaki et al. 2011; Waite et al. 2009).	63
Figure 5.1	Worldwide progression of water depth capability for offshore exploration and production. Each point represents the depth of exploration and platform or floater (offshore-mag.com; Lunne, 2010).	67
Figure 5.2	Dragged devices. (a) NERIDIS III (Marum). (b) OmniMax anchor (Shelton 2007; delmarus.com).	69
Figure 5.3	Side wall samplers: coring and fluid sampling.	71
Figure 5.4	Penetrometers for offshore characterization on soft sediments (Kolk and Wegerif, 2005; fugro.com).	72
Figure 5.5	Cone penetrometers for shallow seabed characterization. (a) Free fall cone (marum.de). (b) Minirig (greggseafloordrill.com).	76
Figure 5.6	In-situ characterization tool: General view.	78

Figure 5.7	Coupling system used to lock the tool to the drill bit.	79
Figure 5.8	Overall mechanical design. (a) Maximum needed force. (b) Maximum tool length to satisfy buckling restrictions. (c) Tool longitudinal stress dependence between water pressure and undrained shear strength.	80
Figure 5.9	Data storage unit: Arduino UNO (arduino.cc).	81
Figure 5.10	Data storage unit: Resolution (a) Thermocouples. (b) Strain gauge. (c) Standard load cell. (d) Power consumption.	82
Figure 5.11	Tip module: parts, elements and wiring.	83
Figure 5.12	Tip module mechanical verification: Yield stress for SS316 is 200MPa.	84
Figure 5.13	Tip module calibration. Measured pressure using strain gauges vs. chamber water pressure.	85
Figure 5.14	Tip module: temperature effect. (a) Thermocouples response time. (b) Strain gage response to temperature change.	86
Figure 5.15	Hydraulic dual-system components: (a) Hydraulic conductivity measurement system. (b) Mini-production test	87
Figure 5.16	Hydraulic conductivity measurement system. (a) Pressure and volume vs. time. (b) Shape factor from numerical simulations. Note: u_0 is the reservoir water pressure and p_0 the initial water pressure in the container.	89
Figure 5.17	Hydraulic conductivity system verification. (a) Numerical model in COMSOL. (b) Comparison of the numerical model and the ideal spherical case. (c) Solution chart for a measured flow rate and water pressure change.	90
Figure 5.18	Porous filter calibration: (a) Setup of the two types of control tests: flow control and pressure control-based test. (b) Results for different porous filter. Lines represent results from numerical simulations and discrete points show measured values.	91
Figure 5.19	Complete hydraulic/fluid sampling test: (a) Setup.	92

	(b) Results for different porous filters.	
Figure 5.20	Electrical resistivity module and calibration.	93
Figure 5.21	Sediment piston sampler. (a) Position in tool. (b) Drawings. (c) Photographs. (d) Field test. e) Extrusion device.	94
Figure 5.22	Video capability prototype test. Image analysis of typical grain compares well with sieving analysis in coarse grains. Sphericity = area of particle projection / area of the circle with diameter equal to the longest length of the projection. Roundness = average radius of curvature of surface features / radius of maximum sphere that can be inscribed.	96
Figure 6.1	Estimation of global gas on the state of hydrate gas. From Sloan and Koh (2007); Boswell and Collett (2011). Notice conventional gas reserves are still orders of magnitude less than the worst of hydrate gas estimations.	98
Figure 6.2	General description of the problem. Below the seafloor, a hydrate layer is located immersed in a generic host sediment. As soon as the production pipe decreases the pressure to h_w , two zones can be defined. The first one from the well to the dissociation front and beyond the dissociation front; both with different permeability values. Note: sub-indices: w = well; far = far field; * = dissociation front	104
Figure 6.3	General description for the spherical dissociation front case.	106
Figure 6.4	Spherical dissociation front. Relationship between dissociation radius, permeabilities and pressure.	108
Figure 6.5	Leaky aquifer case. a) General description, where H = hydrate layer thickness, k_{sed} = sediment permeability, k_{hyd} = hydrate layer permeability, h_w = well water pressure, h^* = dissociation pressure, h_{far} = far field water pressure, r^* = dissociation front, r_w = well radius. b) General description for the double semi-confined aquifer.	110
Figure 6.6	Leaky aquifer case. Best fit for Bessel equation (Ko) for $r/B < 0.5$ and $r/B > 0.3$.	111

Note: $B = \sqrt{\frac{k H b}{k'}}$

Figure 6.7	Economical analysis. Profit per hydrate thickness with respect to dissociation front for selected potential locations.	115
Figure 6.8	Comparison with literature cases. Dissociation front computed tends to be larger than the values from the literature but contained in a 15% error area.	116
Figure 6.9	Example of gas hydrate production from a marine environment under depressurization strategy (Summary of parameters used can be found in Table 6.7).	120

SUMMARY

The amount of carbon trapped in hydrates is estimated to be larger than in conventional oil and gas reservoirs, thus methane hydrate is a promising energy resource. The high water pressure and the relatively low temperature needed for hydrate stability restrict the distribution of methane hydrates to continental shelves and permafrost regions. Stability conditions add inherent complexity to coring, sampling, handling, testing and data interpretation, and have profound implications on potential production strategies.

New guidelines are identified for sampling equipment and protocols. Then a novel technology is developed for handling, transferring, and testing of natural hydrate bearing sediments without depressurization in order to preserve the sediment structure. Natural samples from the Nankai Trough, Japan, are tested as part of this study.

In-situ testing prevents dissociation and the consequences of sampling and handling disturbance. A new multi-sensor in-situ characterization tool is designed and prototyped as part of this research. The tool includes advanced electronics and allows for automated stand-alone operation.

Finally, a robust analytical model is developed to estimate the amount of gas that can be recovered from hydrate bearing sediments using depressurization driven dissociation. Results highlight the complexity of gas extraction from deep sediments, and inherent limitations.

CHAPTER 1

INTRODUCTION

1.1 Methane Hydrate Bearing Sediments

Natural gas hydrates are crystalline compounds made of a hydrogen-bonded framework of water molecules. Gas molecules fill cages within the hydrate lattice structure (Carroll, 2009). Methane, ethane, propane, and carbon dioxide and their mixtures can also form hydrate. Natural gas hydrate can be found in continental shelves or in permafrost regions around the world (Figure 1.1). This research focuses on structure-I methane hydrates found in marine sediments along continental margins.

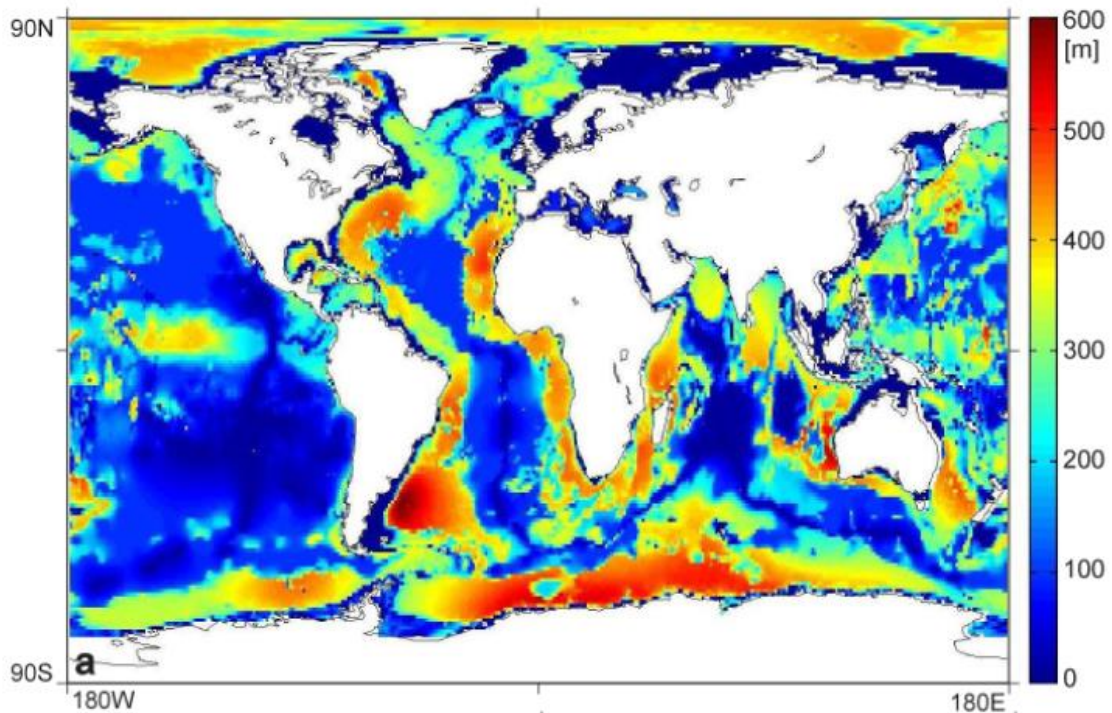


Figure 1.1. Natural methane hydrate systems: Methane hydrate stability zone thickness in marine sediments (Piñero et al., 2013).

Figure 1.2 shows the phase boundary for natural gas hydrate. The formation of gas hydrate may be water- or gas-limited. Then water-and-hydrate, ice-and-hydrate, or gas-and-hydrate might coexist.

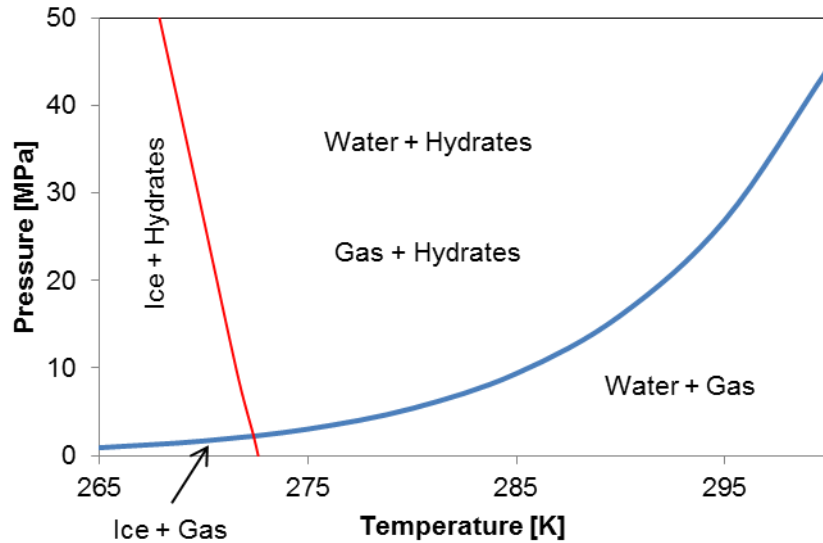


Figure 1.2. Phase boundaries for methane hydrate and ice (Sloan and Koh 2007).

Hydrate formation is hindered in small pores and by high pore water salinities. The total global inventory of carbon in methane hydrates is in the range of ~550GtC (gigatons of carbon; Piñero et al. 2013). Even the lowest estimates suggest that the amount of carbon in methane hydrate exceeds that of coal, oil and gas reserves (Sloan and Koh 2007; Boswell and Collett 2011).

1.2 Energy Geo-Technology

Let's define quality of life QL as a function of water access, life expectancy, infant mortality rate, and average years of schooling. Then, quality of life is strongly correlated with power consumption (Figure 1.3-a; Pasten and Santamarina, 2011).

Energy consumption per capita has increased consistently during the last century. Fossil fuels are the primary source of energy (about 80% of the total energy

consumption; Figure 1.3-b). The availability of petroleum and gas, and the advancement of drilling and fracking methods that made gas from shale viable in the 1990's have delayed field-scale studies of gas production from hydrate bearing sediments in the USA. On the other hand, countries like Japan, India and South Korea lack standard fuel reserves and have placed emphasis on hydrates.

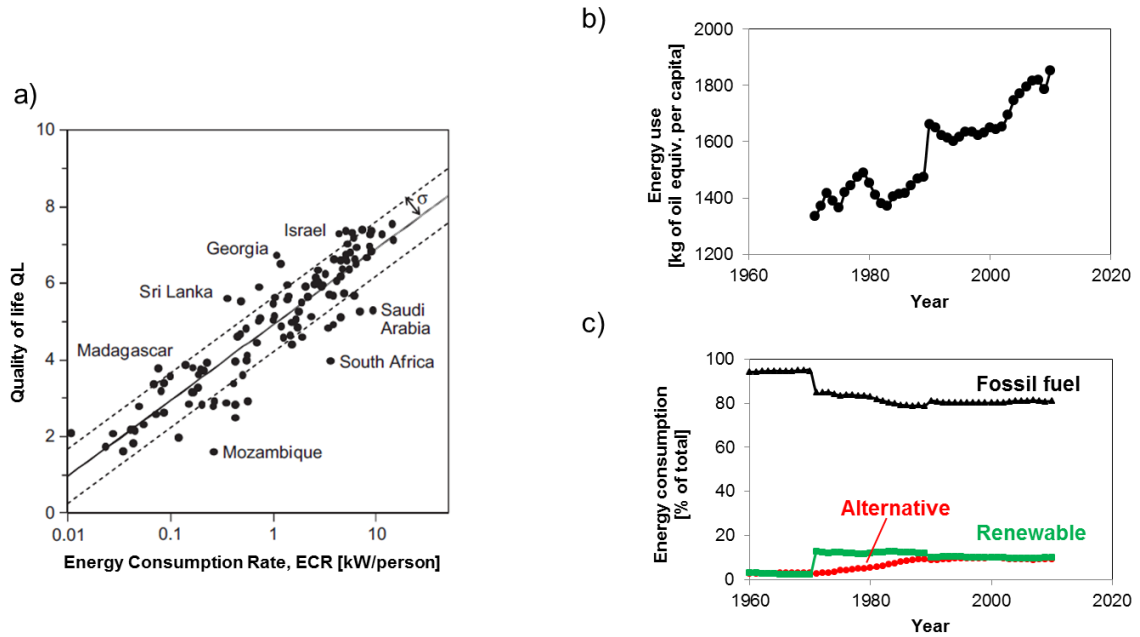


Figure 1.3. Energy geo-technology: (a) Energy and quality of life (Pasten and Santamarina, 2011). (b) Energy use per capita. (c) Energy consumption (data from World Bank, 2013). Note: Fossil fuel = coal, oil, petroleum and gas products; Alternative = non-carbohydrate energy (hydropower and nuclear, geothermal and solar); Renewable = solid and liquid biomass, biogas, industrial waste and municipal waste.

1.3 Reservoir Characterization

Gas production from methane hydrate reservoirs and seafloor instability caused by dissociation are geotechnical problems (Figure 1.4). The physical properties of hydrate bearing sediments determine production methods, well design, and are required for slope stability and bearing capacity analyses.

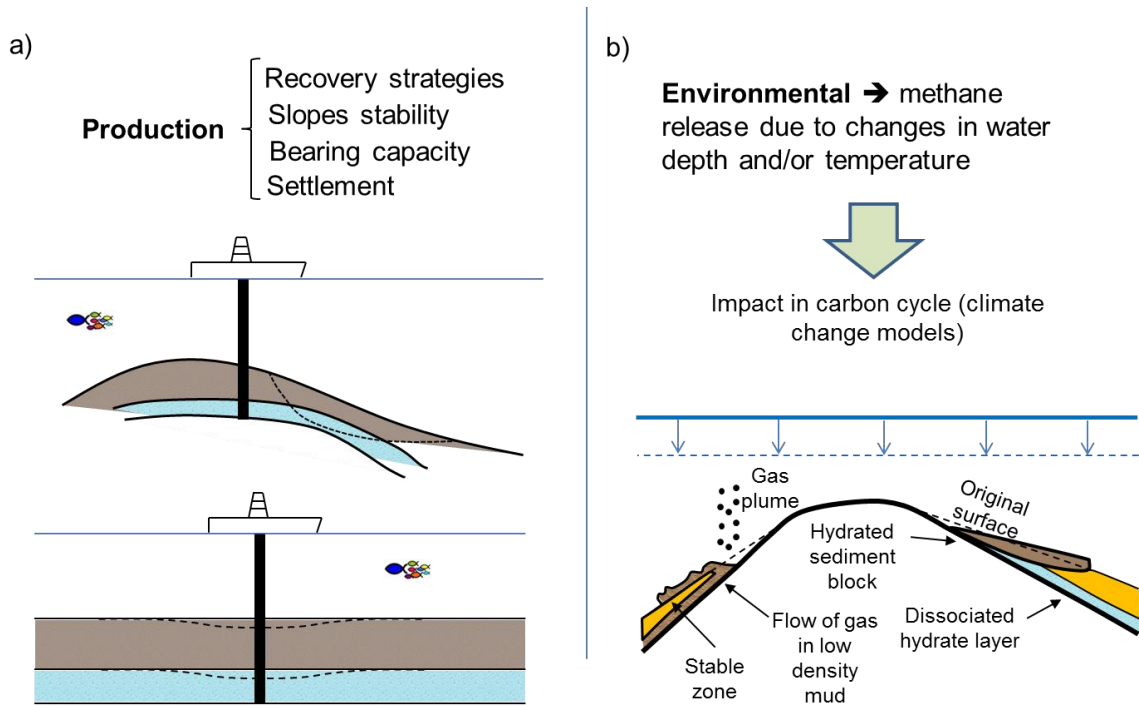


Figure 1.4. Hydrate Bearing Sediments: Geotechnical implications and impact. (a) Production implications. (b) Environmental impact.

The study of methane hydrate bearing sediments has involved disturbed samples and reformed hydrate in laboratory experiments (Figure 1.5). The introduction of pressure coring technology in the 1990's allowed the recovery of samples preserved within stability conditions. The need to test pressure cores led to a new set of tools able to manipulate and test samples without ever removing them from the stability field. These devices have been named Pressure Core Characterization Tools PCCTs (Chapter 3). The PCCTs were successfully deployed in Japan to test pressure cores from the Nankai Trough (Chapter 4).

Even when hydrate is preserved using PCCTs, coring and drilling disturb samples (Chapter 2). To avoid sampling, a new in-situ characterization tool was designed to gather field information and to measure properties in-situ (Chapter 5). Finally, Figure 1.5 shows that all parameters gathered from "undisturbed" PCCT's samples, post dissociation samples with reconstituted hydrate and with the in-situ

characterization tool can be processed and synthesized through an information-rich “IT tool” (not part of this research). Reservoir data and physical parameters are used in production analyses (Chapter 6).

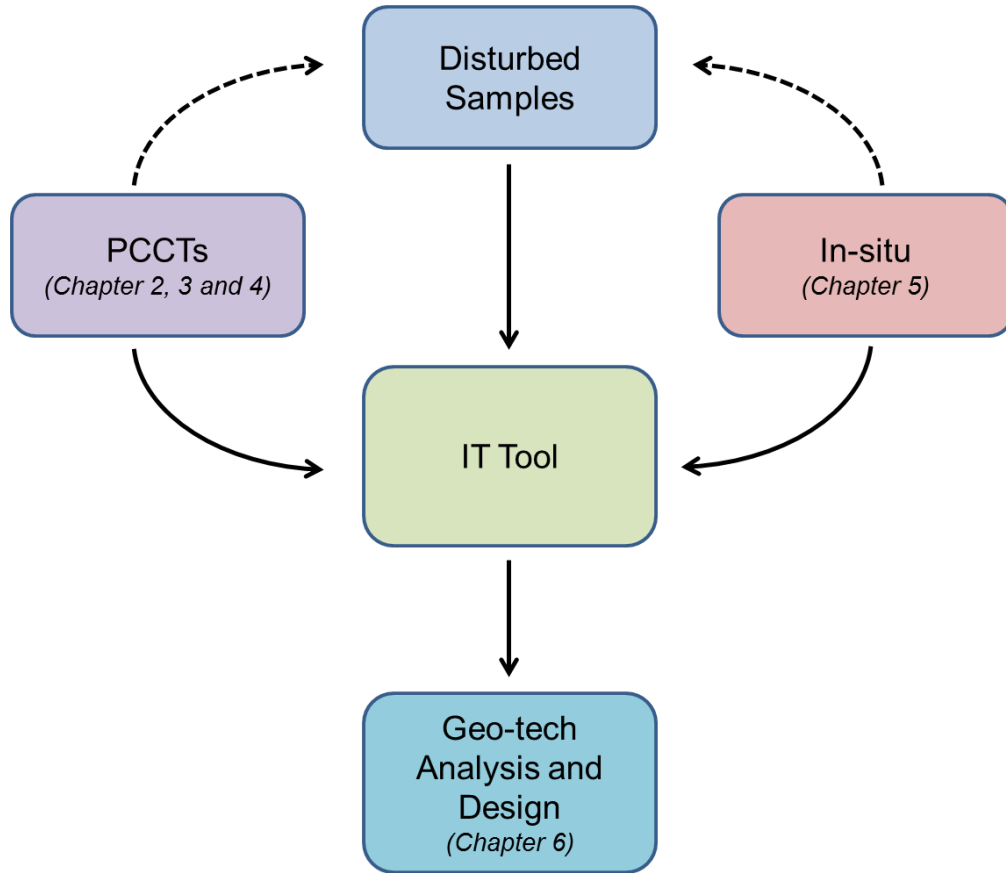


Figure 1.5. Comprehensive characterization of methane hydrate bearing sediments.

1.4 Thesis Organization

This thesis centers on the analysis and characterization of methane hydrate bearing sediments. The main chapters address the following critical issues:

- Chapter 2: sampling disturbance and guidelines for new sampling tools.
- Chapter 3: new tools for the characterization of pressure cores.
- Chapter 4: physical properties of pressure cores recovered from the Nankai Trough, Japan.

- Chapter 5: new in-situ characterization tool.
- Chapter 6: engineering analysis of production limits from hydrate bearing sediments by depressurization.

Finally, Chapter 7 summarizes the main conclusions and findings from this thesis.

CHAPTER 2

SAMPLING LIMITATIONS DURING PRESSURE CORING

2.1 Introduction

Sample disturbance during drilling, cutting and extraction limits the validity of geotechnical engineering analyses and design. Sampling implies the loss of effective stress and associated soil destructuring (Santagata and Germaine, 2005; Santagata and Germaine, 2002). When sampling changes the soil structure, the classical re-loading techniques will not reproduce the original stress-strain response (Ladd and Foott, 1974; Tanaka, 2000; Tanaka et al., 2002; Hird and Hajj, 1995).

Methane hydrate is stable at high water pressure and low temperature. Hydrate dissociation will result in free water and gas, and a 172 times expansion of the original hydrate volume. This expansion is particularly disruptive in the case of hydrate bearing sediments.

The proper design of sampling equipment and procedures plays a critical role on the accuracy of measured properties. This chapter summarizes soil sampling disturbance, and describes current sampling technology for marine sediments. Finally, it recommends guidelines for sampling equipment design.

2.2 Literature Review

Sample extraction can be classified into six categories (Hvorslev, 1949): displacement boring, wash boring, percussion drilling, rotary drilling, auger boring and continuous sampling. This classification can be extended to consider accessible exploration methods such as trenches, tunnels, and caissons among others. The associated degree of disturbance depends on soil type, cementation, particle diameter, and in-situ conditions.

Additional conditions for sampling disturbance occurs during sample handling

from the site to the laboratory, extrusion of the sample from the sampler, and trimming to prepare the sample to be tested (Baligh et al. 1987; Ladd and DeGroot, 2003).

The term “undisturbed sample” refers to specimens that have experienced minimal disturbance so that all properties after sampling are relevant to in-situ conditions (Hvorslev, 1949). “Ideal sampling” is used to describe conditions where the disturbances are only caused by stress relaxation (Figure 2.1). In this case, the stress path is known and sampling can be analyzed using the strain path method (Baligh et al., 1987; Ladd and DeGroot, 2003; Safaqah and Riemer, 2006). However, ideal sampling does not take into account the sampler insertion, shear stresses due to wall friction and sampler imperfections (Clayton and Siddique, 1999).

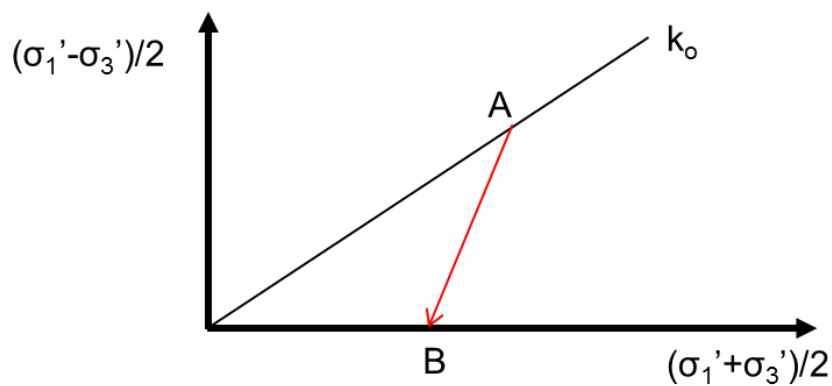


Figure 2.1. Ideal sampling: Point A is in-situ state of stress, B is the isotropic state of stress (modified from Baligh et al., 1987).

Sampling disturbance involves (Hvorslev, 1949; La Rochelle et al. 1981; Skempton and Sowa, 1963; Hird and Hajj, 1995; Santagata and Germaine, 2005; Santagata and Germaine, 2002; Horng et al. 2010; Li et al. 1997; Budhu and Wu, 1992; Clayton et al. 1998; Karim, 1984) change in stress, change in void ratio, change in degree of saturation, disturbance of soil structure, chemical changes, mixing and segregation of soil constituents, and altered conditions for bioactivity.

The consequences of sampling disturbance include (Budhu and Wu, 1992; Clayton and Siddique, 1999; Long, 2002; Long, 2003; Safaqah and Riemer, 2006;

Santagata and Germaine, 2002; Siddique et al. 1999):

- Reduction of pre-consolidation stress
- Reduction of initial stiffness
- Increase of post yield stiffness
- Increase of the strain at peak failure
- Increase of recompression index
- Decrease of the virgin compression index
- Reduction of shear modulus
- Destruction of the internal structure

The effects of sampling disturbance in fine-grained soils are less pronounced in soils with intermediate OCR than in normally consolidated soils (Santagata and Germaine, 2005; Siddique et al. 1999).

2.2.1 Plugging

Friction develops in the soil column as it enters the sampler. The sampler may plug and limit the length of recovered soil. Plugging can develop under all types of driving conditions (Iskander 2011), and the recovered sample is severely affected (Hvorslev, 1949; La Rochelle et al. 1981). An analogue condition develops during pile driving (Paikowsky 1990). Plugging has been studied using field tests (Brucy 1991; Paik et al. 2003), laboratory tests (de Nicola and Randolph 1998), and through analytical/numerical methods (Leong and Randolph 1991; Murff et al. 1990; Randolph et al. 1991).

Plugging results from the arching within the sediment as side friction develops between the wall and the soil (Paikowsky 1990; Paikowsky and Whitman 1990; Paikowsky et al. 1989; Randolph et al. 1991). The penetration resistance increases with depth: the plug forms when the resisting force exceeds the bearing capacity of the soil (Paikowsky and Whitman 1990). Inside the pipe, the soil becomes denser closer to the

tip and it may loosen away from it (Paikowsky 1990; de Nicola and Randolph 1997; Horng et al. 2010; Hvorslev, 1949).

Plugging typically develops when the insertion depth is 10 to 20 times the diameter of the pipe in clayey soils, and 25 to 35 times the diameter of the pipe in sandy soils (Paikowsky and Whitman 1990). The specific recovery ratio γ is defined as the increment in sample length corresponding to a unit increment of sampler penetration, and can be used as an indicator for plugging (Paikowsky et al. 1989): the soil ahead of the cutting shoe enters the sampler when $\gamma > 1$ but plugs when $\gamma < 1$. A value $0 < \gamma < 1$ indicates partial plugging (Table 2.1). The recovery ratio is $R = L_{\text{recovered}}/L_{\text{sampler}}$.

Table 2.1: Specific recovery ratio

Influence factor		Driving method	γ [%]	Soil	Reference
Ca	79 %	Slow jacking	30	Soft varved clay	Hvorslev (1949)
	10%		45		
Ci	0%	Shooting	10	Clayey sandy silt partially saturated	
	1.8%		80%		
	4.8%		185% (sample lost)		
Sampler	1" Porter (Ci=5%, Co=12.2%, Ca=147%)	Hammering	40%	Soft varved clay	
		Slow jacking	20%		
		Fast pushing	75%		
		Hammering	40%		
Sampler	2" Brass (Ci=-1.6%, Co=0%, Ca=6.6%)	Fast pushing	40%	Soft varved clay	
		Hammering	35%		
		Single blow	30%		
		Hammering	30%		
Sampler	2" Steel (Ci=1.2%, Co=0%, Ca=10%)	Slow jacking	45%	Soft varved clay	
		Fast pushing	90% (constant decrease)		
		Hammering	95%		
		Slow jacking	100% (almost always > 100%)		
Sampler	4 3/4" Mohr (Ci=2.9%, Co=4.6%, Ca=4.4%)	Fast pushing	110% (almost always > 100%)	Soft varved clay	
		Hammering	95%		
		Slow jacking	100% (almost always > 100%)		
		Fast pushing	110% (almost always > 100%)		
--		Hammering	77.5%	Sand	Paik et al. (2003)

2.2.2 Sampler Dimensions Effects

A larger ratio between the tube diameter and its thickness, and a sharper edge result in fewer disturbances (Clayton and Siddique 1999; Horng et al. 2010; Long 2002; DeGroot 2003). The soil close to the wall experiences the most disturbance (Baligh et al. 1987).

Figure 2.2 shows a typical sampler. The dimensionless “inside clearance” C_i controls the inside friction, the “outside clearance” C_o the outside friction, and the “area ratio” C_a represents the volume of the displaced soil relative to the sampled volume. The area ratio should be $C_a < 13\%$ (Hvorslev, 1949; Karim 1984) but often exceeds 30% (Clayton et al. 1995). The C_a value is limited by structural requirements (buckling).

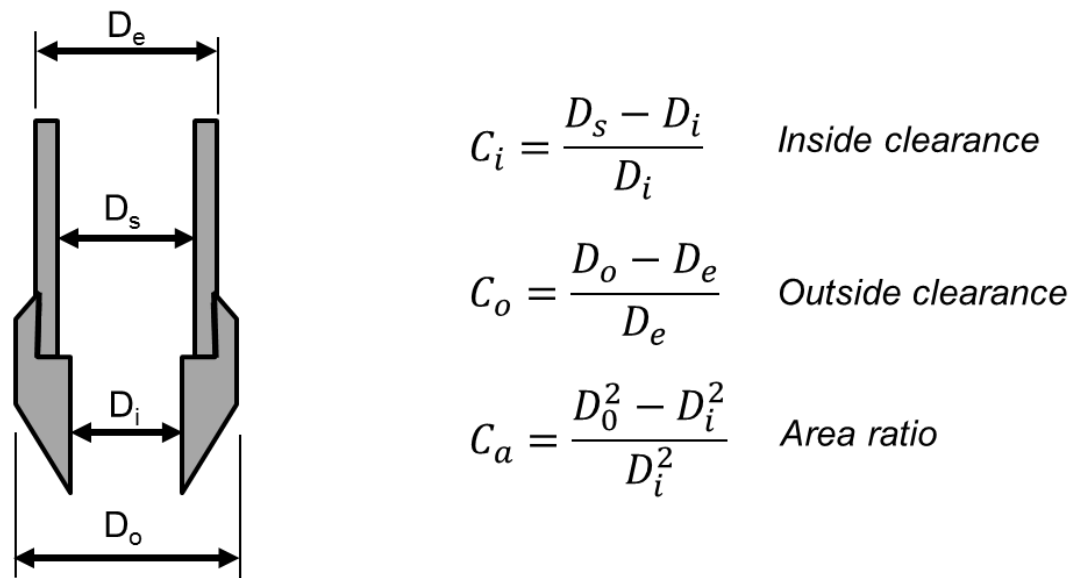


Figure 2.2. Sampler diameters and definitions.

The taper angle and the area ratio combine to minimize disturbance. In particular, a lower taper angle α results in less disturbance (Clayton et al. 1998; Horng et al. 1998; La Rochelle et al. 1981; Horng et al. 2010; Budhu and Wu 1992). Preferred ranges go from an angle $\alpha = 15^\circ$ for $C_a = 5\%$ to $\alpha = 4^\circ$ for $C_a = 80\%$ (Clayton et al. 1995).

The sampler wall prevents the lateral relaxation of the sample. As the inside

clearance decreases, the probability of tension developing above the tip decreases (Clayton and Siddique 1999). Some samplers for normally consolidated or slightly over-consolidated clays have no inside clearance, $C_i = 0$ (La Rochelle et al. 1981), but it is not recommended for over-consolidated clays (Clayton et al. 1995). Inside clearance ranges from $C_i = 0.75\%$ and 1.5% for long samples (Clayton and Siddique 1999; Hvorslev 1949) and smaller clearance $C_i = 0$ to 0.5% is acceptable for short samples (Hvorslev, 1949; see also ISSMEFE Report of the Subcommittee on Problems and Practices in Soil Sampling). The thin-wall sampler proposed by ASTM (D6519-08) has an inside clearance $C_i = 1\%$.

A fast penetration hinders the development of static friction; therefore continuous fast pushing and even explosives can be used for fast insertion (Hvorslev 1949; Clayton and Siddique 1999). Conversely, friction will increase significantly if coring is interrupted even for a few seconds (Lunne and Long 2006). Suggested penetration rates vary widely:

- ASTM (D6519-08 and D1587-08) does not specify the rate of penetration but suggests: “Advance the sampler without rotation by a continuous relatively rapid downward motion ...”
- Hvorslev, (1949) recommended a penetration speed of more than 15 mm/sec.
- Schmertmann and Palacios (1979) computed the speed for SPT sampler and concluded that in common practice it varies from 980 mm/sec to 1400 mm/sec.
- La Rochelle et al. (1981) suggested a rate of 0.138 mm/sec (0.5 m/hr) for up to 20 m for the Laval sampler.
- Budhu and Wu (1992) concluded that the rate of penetration should exceed $\sim 0.4\text{mm/sec}$.

Sampling extraction from the sampler may be a major source of disturbance, often due to the unnecessary tensile and rotational stresses applied onto the sediment to detach it from the sampler. Lower perturbation is caused by sliding the specimen in the

same direction as it went inside the sampler. Alternatively, the sampler can be used as the test chamber itself. This approach has been developed and extensively used at the Particulate Media Research Lab. Limited results show significantly lower loss in stiffness (Unpublished).

2.3 Pressure Coring

Core recovery from sediments subjected to high in-situ water pressure can experience severe disturbance if gas dissolution or hydrate dissociation take place. In this case specimens must be recovered using pressure core technology, to prevent exsolution or dissociation.

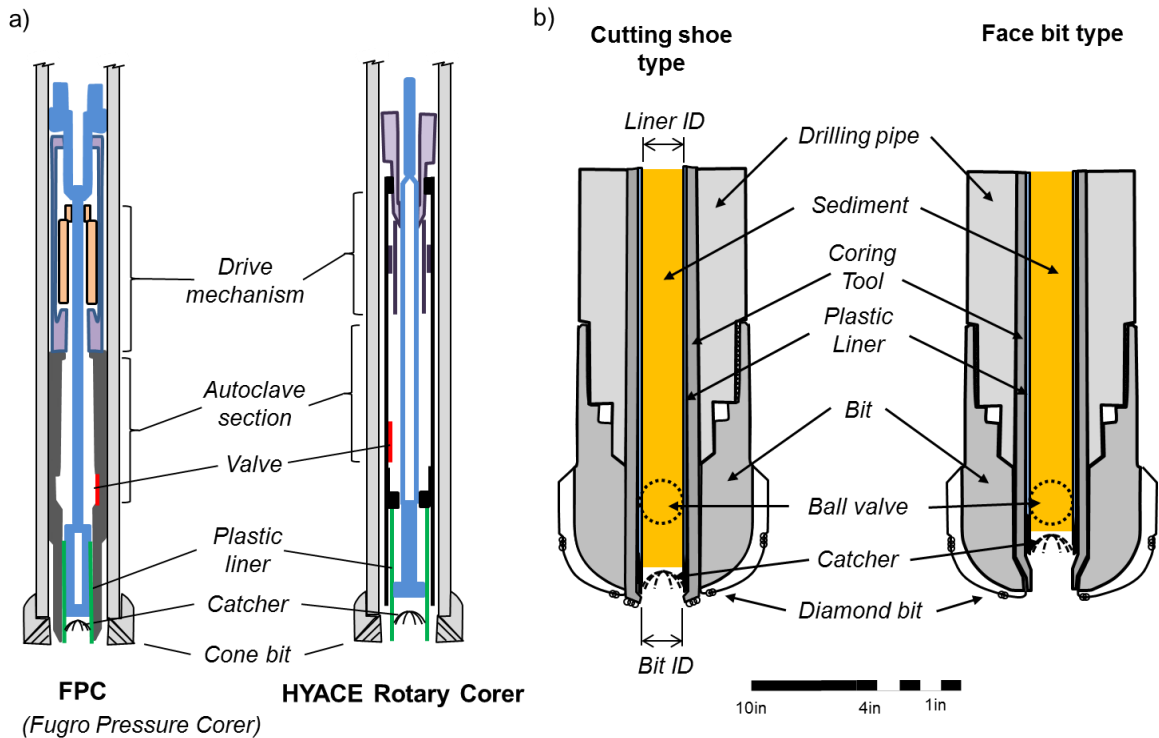


Figure 2.3. Pressure corers: (a) Fugro Pressure Corer and HYACE (modified from Peuchen, 2007; Kolk and Wegerif, 2005; iodp.org). (b) Typical cross section of a drilling bit for: cutting shoe and face bit type.

A typical drilling and coring system for deep marine sediments is shown in Figure 2.3. It consists of a drive mechanism, the autoclave section, a plastic liner with a

catcher and a valve to maintain the internal water pressure. The Fugro Pressure Corer FPC uses a percussion system to drive the tool, while the HYACE Rotary Corer relies on an Inverse Moineau Motor driven by mud circulation (Kolk and Wegerif 2005; Huey 2009). Once the specimen slides into the plastic liner and is trapped by the catcher, the tool can be lifted from the recovery hook. The specimen remains housed in the autoclave section and the ball valve is closed to maintain internal water pressure. Figure 2.3-b shows a detailed close-up of the drilling bit and two types of cutting bits: cutting shoe and face bit type. Typical dimensions are listed in Table 2.2. The core length can reach 3.5 m for deep sediments (Kubo et al., 2014; Abegg et al, 2008).

Table 2.2: Typical drill bit dimensions for currently available coring techniques for bottom hole sampling (from Kubo et al., 2014; Peuchen, 2007; Kolk and Wegerif, 2005; Kawasaki et al., 2006; iodp.org; Huey, 2009; Zhu et al. 2013; Fugro.com)

Coring system	Drill Pipe Diameter [mm]	Core Bit ID [mm]	Liner ID [mm]	Max Pressure [MPa]
IODP		41.9	(*)	69
Fugro FPC	127 to 139.7	50.4	58.0	35
Fugro HYACE		50.4	52.3	35
Aumann		51.4	53.6	35
JOGMEC PTCS	168.3	66.6	66.6	24
CDEX hybrid PCS	127 to 139.7	50.4	(**)	35

(*) No plastic liner utilized

(**) Not reported

Note: Hybrid PCS is also named PCTB

Pressure cores have been recovered from hydrate bearing sediments in China, India, Japan, Korea, Taiwan and USA (Koh et al. 2012; Schultheiss et al 2009). The recovery success ratio rarely exceeds 60-70% (Yamamoto et al. 2012).

Even the best quality pressure cores share all other sampling difficulties listed for shallow cores in the previous sections. X-ray images taken of all the cores in the Japan expedition readily show sampling effects such as: edge shear, friction, sample expansion, core rotation, gaps or extensional separation (Figure 2.4).

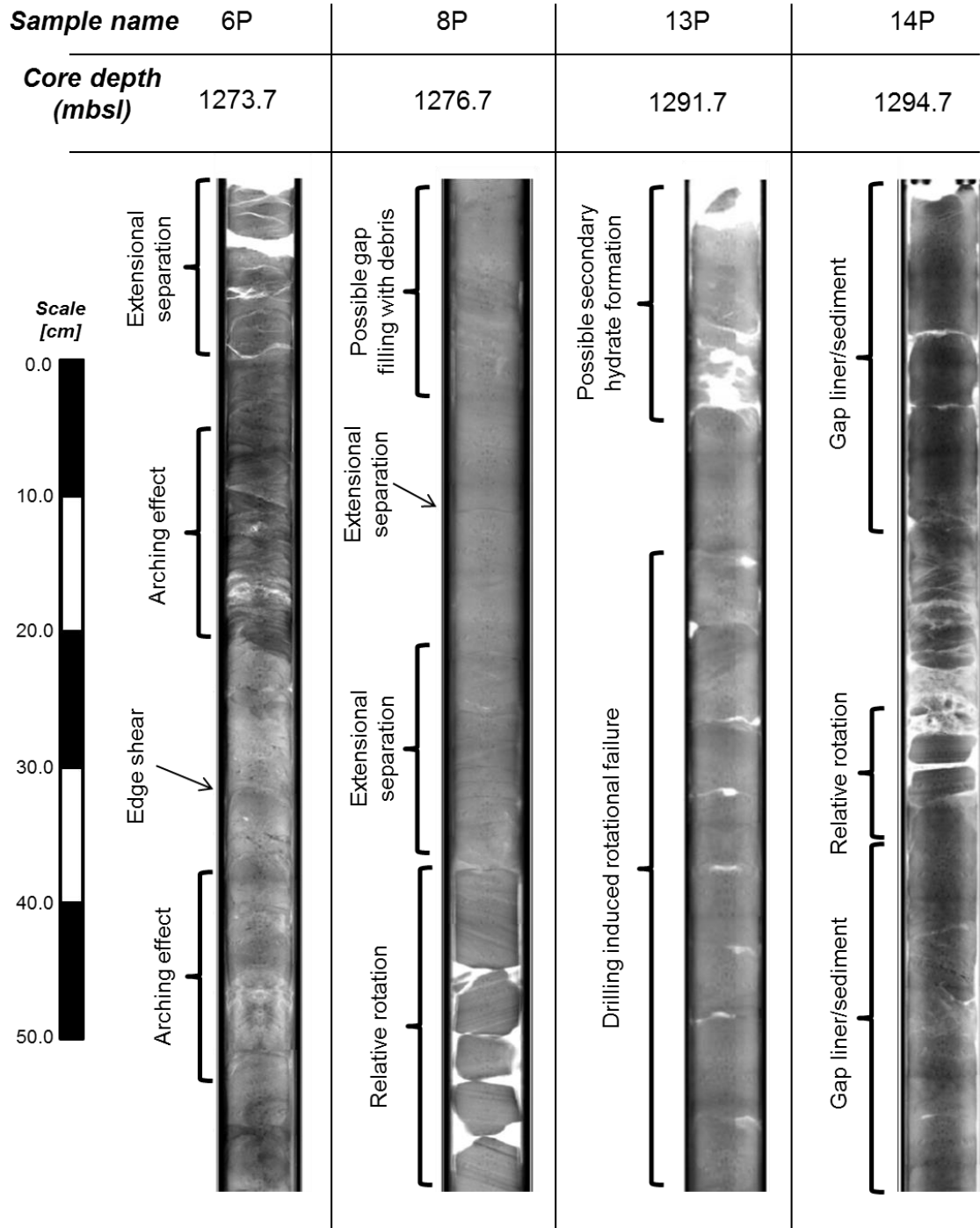


Figure 2.4. Typical X-ray images from the pressure cores recovered at the Nankai Trough, Japan (with permission JOGMEC). Samples were obtained using a 53.6mm (ID) liner and 51.4mm cutting shoe (JOGMEC corer).

2.4 Coring Disturbances

Two extreme conditions are analyzed next. First, a cemented core is allowed to expand freely within the sampler and may experience yield. Second, an un-cemented sediment mobilizes friction as it slides into the sampler and may plug.

2.4.1 Cemented Soils: Radial Expansion

Rotary coring is used to advance the sampler in cemented soils. The cutting shoe diameter is typically smaller than the sampler size with inside clearance $C_i > 0$. As soon as the core enters into the sampler, the effective lateral stress is released and the core expands (Figure 2.5). The optimal gap/clearance between the cutting shoe and the sampler liner C_i has to be large enough to allow the core to enter the sampler easily, but small enough so that minimal core relaxation takes place.

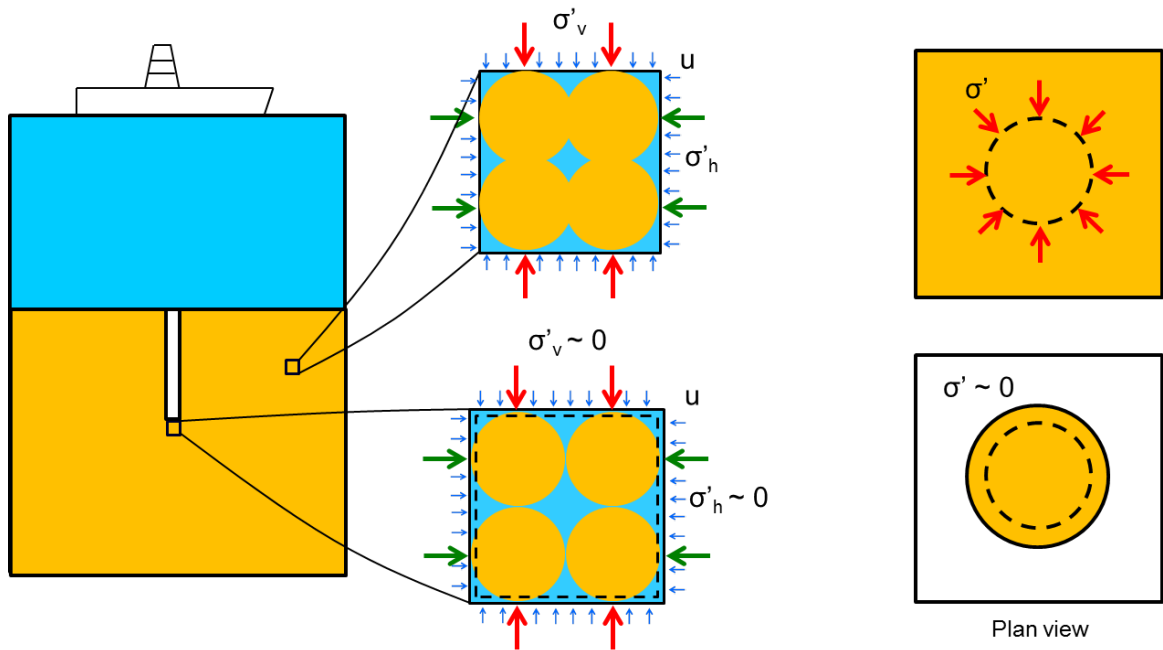


Figure 2.5. Soil expansion due to confinement release.

Let's assume that the core expands in the radial direction only (expansion in the z direction is not relevant for this analysis). The change in core stresses reflects the elastoplastic material response. The general case is solved next. Equilibrium in the radial

direction for an element in cylindrical coordinates r, θ, z is (refer to Figure 2.6-a):

$$(\sigma_{rr} + d\sigma_{rr})(r + dr)d\theta = \sigma_{rr} r d\theta + \sigma_{\theta\theta} d\theta dr \quad (2.1)$$

Ignoring second order terms and re-arranging:

$$\frac{\partial \sigma_{rr}}{\partial r} + \frac{1}{r}(\sigma_{rr} - \sigma_{\theta\theta}) = 0 \quad (2.2)$$

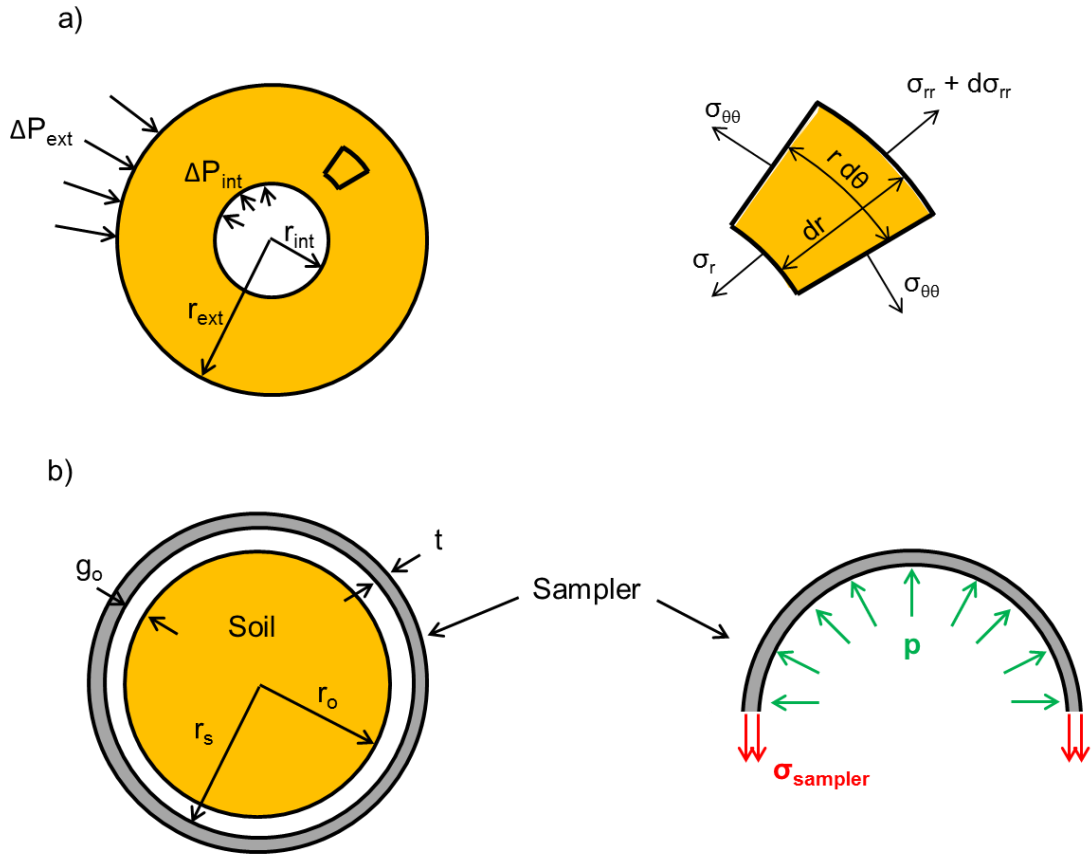


Figure 2.6. General geometry for the analysis of the sampler-soil interaction. (a) General solution. (b) Soil expansion against the sampler.

The radial and tangential strains are

$$\varepsilon_r = \frac{\partial u_r}{\partial r} \quad (2.3)$$

$$\varepsilon_\theta = \frac{u_r}{r} \quad (2.4)$$

From Hooke's law:

$$\sigma_{rr} = \frac{E}{1-\nu^2} (\varepsilon_r + \nu \varepsilon_\theta) = \frac{E}{1-\nu^2} \left(\frac{\partial u_r}{\partial r} + \nu \frac{u_r}{r} \right) \quad (2.5)$$

$$\sigma_{\theta\theta} = \frac{E}{1-\nu^2} (\varepsilon_r + \nu \varepsilon_\theta) = \frac{E}{1-\nu^2} \left(\nu \frac{\partial u_r}{\partial r} + \frac{u_r}{r} \right) \quad (2.6)$$

Substituting in (2.2):

$$\frac{\partial^2 u_r}{\partial r^2} + \frac{1}{r} \frac{\partial u_r}{\partial r} - \frac{u_r}{r^2} = 0 \quad (2.7)$$

The solution of this equation is:

$$u_r = Ar + \frac{B}{r} \quad (2.8)$$

Substituting in (2.5) and (2.6):

$$\sigma_{rr} = \frac{E}{1-\nu^2} \left[A(1+\nu) - B \left(\frac{1-\nu}{r^2} \right) \right] \quad (2.9)$$

$$\sigma_{\theta\theta} = \frac{E}{1-\nu^2} \left[A(1+\nu) + B \left(\frac{1-\nu}{r^2} \right) \right] \quad (2.10)$$

Then the constants are solved at these boundaries: $\sigma_{rr}(r_{int}) = -\Delta P_{int}$ and $\sigma_{rr}(r_{ext}) = -\Delta P_{ext}$, where ΔP_{int} [Pa] is the internal pressure change, and ΔP_{ext} [m] is the external pressure change; to obtain:

$$A = \frac{1-\nu}{E} \left(\frac{r_{int}^2 \Delta P_{int} - r_{ext}^2 \Delta P_{ext}}{r_{ext}^2 - r_{int}^2} \right) \quad (2.11)$$

$$B = \frac{1-\nu}{E} \left[\frac{r_{int}^2 r_{ext}^2 (\Delta P_{int} - \Delta P_{ext})}{r_{ext}^2 - r_{int}^2} \right] \quad (2.12)$$

For the particular case of a cylinder: $r_{int} = 0$ and $-\Delta P_{int} = 0$, yielding:

$$A = \frac{1-\nu}{E} (-\Delta P_{ext}) \quad (2.13)$$

$$B = 0 \quad (2.14)$$

Then, the displacement at the edge of the cylinder is:

$$u_r|_{r_o} = \frac{1-\nu}{E} (-\Delta P_{ext}) r_o = \frac{(-\Delta P_{ext}) r_o}{2 G_{soil}} \quad (2.15)$$

In this case, ΔP_{ext} is the change in external pressure exerted by the cylinder. For the case of the specimen analyzed here, $\Delta P_{\text{ext}} = \sigma'_{\text{lat}} - p$, where σ'_{lat} is the original lateral effective stress and p is the final confinement the sample experiences in the sampler tube. Therefore:

$$u_r|_{r_o} = \frac{(\sigma'_{\text{lat}} - p)r_o}{2 G_{\text{soil}}} \quad (2.16)$$

where G_{soil} [Pa] is the soil shear stiffness and r_o [m] the core radius. When the sampler confinement is $p = 0$ the core relaxes and the radial strain reaches its maximum value.

The sampler will take the relaxation load as soon as the soil engages the sampler wall. The relationship between the radial displacement and the internal pressure in a thin walled tube is given by Figure 2.6-b. If there is a radial gap g_o [m]:

$$u_r = g_o + \frac{r_s^2}{E_{\text{sampler}} t} p \quad (2.17)$$

where E_{sampler} [Pa] is the Young modulus of the material of the sampler, t [m] is the sampler wall thickness and r_s is the sampler radius.

If the core remains elastic, Equations 2.1 and 2.4 predict:

$$u_{r,\text{soil}} = u_{r,\text{sampler}} \quad (2.18)$$

$$\frac{\sigma'_{\text{lat}} - p}{2G_{\text{soil}}} r_o = g_o + \frac{r_s^2}{E_{\text{sampler}} t} p \quad (2.19)$$

The confining pressure the sampler exerts on the core when it is fully engaged ($r_o = r_s$) is:

$$p = \frac{\frac{\sigma'_{\text{lat}} r_s}{2G_{\text{soil}}} - g_o}{\frac{r_s^2}{E_{\text{sampler}} t} + \frac{r_s}{2G_{\text{soil}}}} = \frac{\frac{\sigma'_{\text{lat}}}{2G_{\text{soil}}} - C_i}{\frac{r_s}{E_{\text{sampler}} t} + \frac{1}{2G_{\text{soil}}}} \quad (2.20)$$

2.4.2 Non-cemented Soils: Plugging

Un-cemented sediments will yield and “flow” inside the sampler, fill the gap g_o and develop friction against the sampler wall. Then, the length of the recovered core will

be a function of core-sampler frictional resistance and the bearing capacity at the front of the corer. When these two forces are equal, the soil ahead of the sampler will displace away from the coring tool and will not slide into the sampler.

The vertical equilibrium of a slice of core height dz is (Figure 2.7; see also Randolph et al. 1991):

$$\left[\sigma'_z - \left(\sigma'_z + \frac{\partial \sigma'_z}{\partial z} dz \right) \right] \pi r_s^2 = \pi r_s^2 \gamma dz + f_s (2 \pi r_s dz) \quad (2.21)$$

where $f_s = \sigma'_z \mu k$, μ is the friction coefficient between the soil and the sampler and $k = \sigma'_h / \sigma'_z$ is the stress ratio for the sediment inside the sampler. Then:

$$\frac{\partial \sigma'_z}{\partial z} = \gamma + \frac{2 \mu k}{r_s} \sigma'_z \quad (2.22)$$

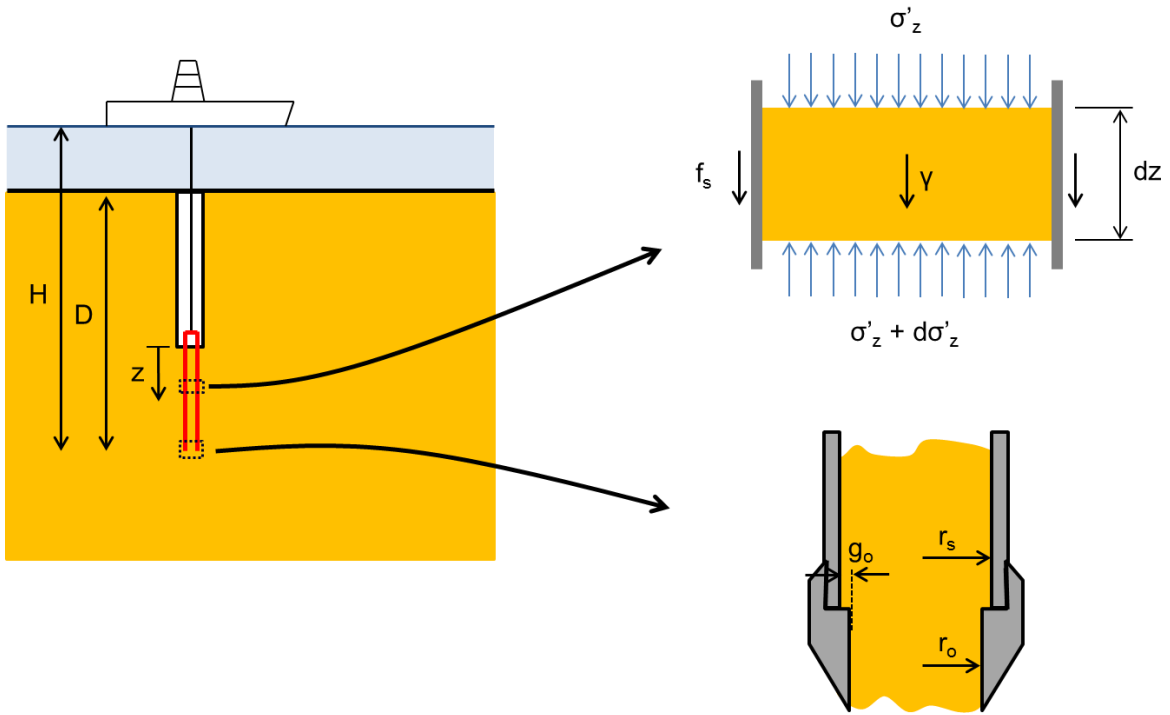


Figure 2.7. Non-cemented soils: Forces involved in plugging.

The closed form solution for equation 2.22 is (Coddington 1961):

$$\sigma'_z = C_1 + C_2 e^{(-C_3 z)} \quad (2.23)$$

Then:

$$\sigma'_z = \frac{\gamma r_s}{2 \mu k} \left[e^{\left(\frac{2 \mu k z}{r_s}\right)} - 1 \right] \quad (2.24)$$

where σ'_z is the vertical effective stress, γ effective soil unit weight, r_s sampler radius.

On the other hand, the bearing capacity for a deep foundation is:

$$q_{ult} = \sigma'_o N_q \quad (2.25)$$

where σ'_o is the vertical effective stress applied at the tip of the sampler and N_q bearing capacity factor which can be approximated from the friction angle ϕ by:

$$N_q = 1.05 e^{0.12 \phi} \quad (2.26)$$

Plugging starts when:

$$\sigma'_z = q_{ult} \quad (2.27)$$

$$\frac{(\gamma_{sat} - \gamma_w) r_s}{2 \mu k} \left[e^{\left(\frac{2 \mu k z}{r_s}\right)} - 1 \right] = D (\gamma_{sat} - \gamma_w) N_q \quad (2.28)$$

where D is the sampling depth (see Figure 2.7). Therefore the maximum length of core that can be recovered before plugging is:

$$z = \frac{r_s}{2 \mu k} \ln \left(\frac{2 \mu k D N_q}{r_s} + 1 \right) \quad (2.29)$$

Lateral stress ratio k ranges from rest (k_o) to active pressure (k_a). The interface interaction $\beta = \mu k$, is plotted in Figure 2.8. This coefficient varies in a short range for typical soil friction angles. A value of $\beta = 0.11$ to 0.17 can be adopted.

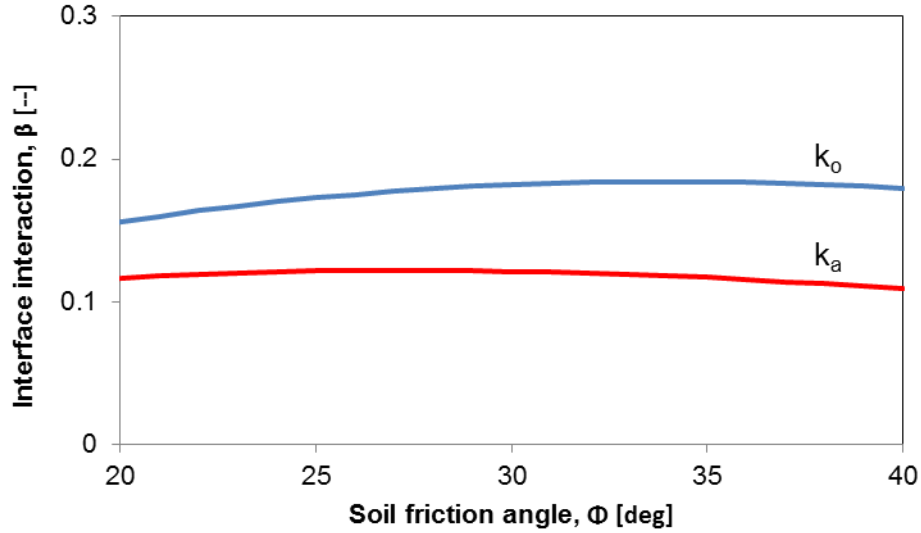


Figure 2.8. Interface interaction coefficient β .

2.5 Guidelines for Coring and Sampling Tool Design

The previous analyses are the foundations for the development of mechanically robust guidelines for the design of coring (gap) and sampler length.

2.5.1 Optimal Gap

The inside clearance coefficient can be defined as $C_i = g_o/r_s$, where g_o is the gap between the cutting shoe and the sampler radius r_s (Figure 2.7). The inside clearance can be computed from Equation (2.19) for the case of full engagement ($r_o = r_s$). The goal is to allow a stress relaxation that does not fall below the yield stress $\sigma_{y,soil}$:

$$C_i = \frac{g_o}{r_s} = \left(\frac{\sigma'_{lat} - \sigma_{y,soil}}{2G_{soil}} - \frac{r_s \sigma_{y,soil}}{E_{sampler} t} \right) \quad (2.30)$$

where $p = \sigma_{y,soil}$ is the soil yield stress.

Values of C_i are plotted in the Figure 2.9 as function of the strain at relaxation $(\sigma'_{lat} - \sigma_{y,soil})/(2 G_{soil})$ and the sampler stretching $(r_s \sigma_{y,soil})/(E_{sampler} t)$. Published guidelines are superimposed on the figure. Results confirm that a gap should be allowed for soft

samples with low $\sigma_{y,soil}$. The optimal gap is small compared to real sampler dimensions and tolerances. This means that cemented cores will expand and yield long before they react against the sampler wall. For example, let's consider cores recovered from the Nankai Trough, Japan, and typical hydrate bearing sediment properties. Results plotted in Figure 2.10 show loss in confinement and relaxation beyond acceptable values. In fact, X-ray images in Figure 2.4 show the sediment completely detached when hydrate cements the sediments; conversely, the sediment fills the gap in hydrate-free layers. The insert in Figure 2.10 shows the plastic liner p- ϵ curve that plots outside the acceptable core deformation range.

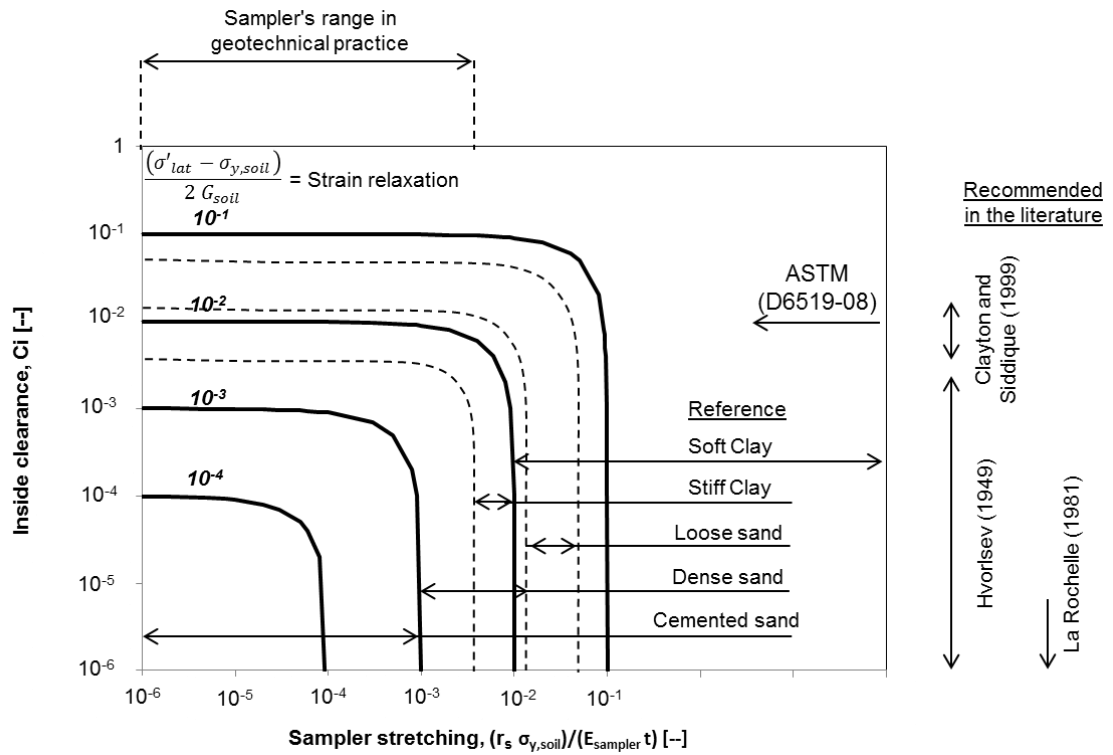
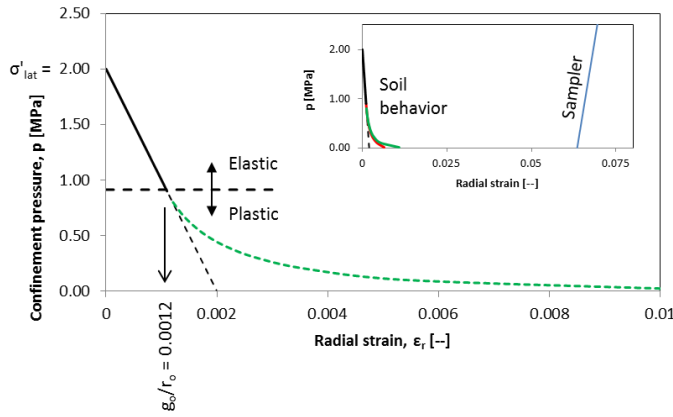


Figure 2.9. Optimal gap: Design chart for a linear elastic soil.



Optimal gap $\rightarrow g_o = 0.0012 \cdot 25.4 \text{ [mm]} = 0.03 \text{ mm}$

$$C_i = \frac{D_1 - D_2}{D_2} = \frac{2 \cdot g_o}{2 r_s} = \frac{0.03 \text{ [mm]}}{26.8 \text{ [mm]}} = 0.11\%$$

Sampler's gap $\rightarrow g_o = 26.8 \text{ mm} - 25.2 \text{ mm} = 1.6 \text{ mm}$

$$C_i = \frac{D_1 - D_2}{D_2} = \frac{2 \cdot g_o}{2 r_s} = \frac{1.6 \text{ [mm]}}{26.8 \text{ [mm]}} = 5.9\%$$

	Parameter	Unit	Value
	σ'_{lat}	[MPa]	2
	$\sigma_{y,soil}$	[MPa]	0.8
Soil	G	[MPa]	500
	ϕ	[deg]	30
	r_o	[mm]	25.2
	r_s	[mm]	26.8
	t	[mm]	3
Sampler	$\sigma_{y,plastic}$	[MPa]	30
	$E_{plastic}$	[GPa]	4

Figure 2.10. Example of a plastic liner sampler computation for a frictional soil for the case of hydrate bearing sediments in Nankai Trough. Insert: large scale to accommodate soil and sampler behavior.

2.5.2 Maximum Recoverable Length (un-cemented sediments)

The maximum expected core length before plugging can be computed from Equation 2.29. The design chart in Figure 2.11 shows this equation as a non-dimensional function of the dimensionless depth D/r_s and sampled length z/r_s for engineering practices. Other parameters μ , k and N_q are function of the friction angle. Results show that the recoverable length increases with depth and friction angle, but for engineering practical purposes $z/r_s \rightarrow \sim 30$ for deep sediments. In general, a recoverable length of $z/r_s = 10-15$ should be expected (similar values obtained from data from Paikowsky and Whitman 1990).

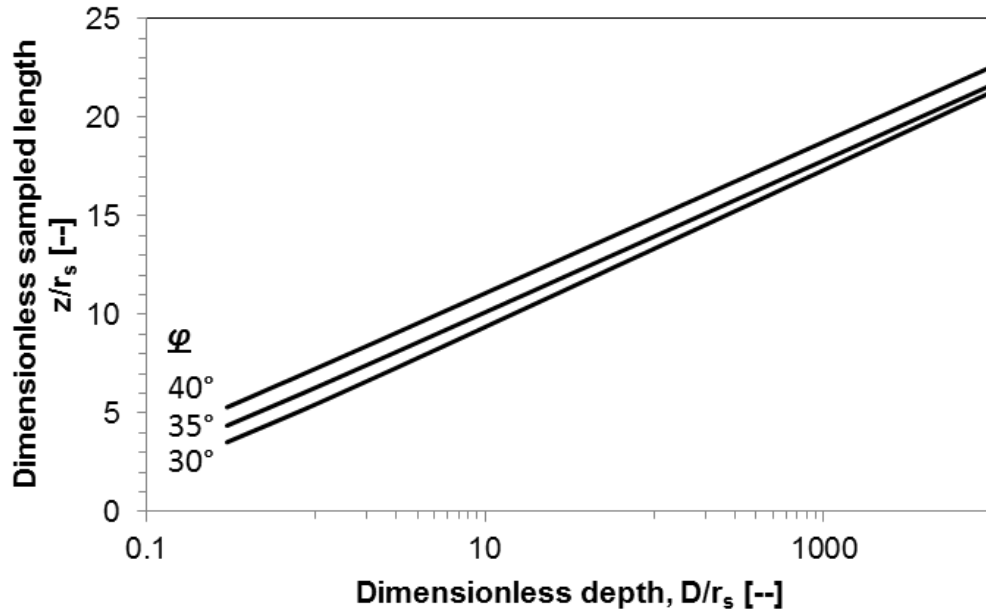


Figure 2.11. Maximum expected recoverable core length: Design chart for frictional soil.

Consider the case of hydrate bearing sediments: a $r_s = 25\text{mm}$ sampler and operating at depths of 300 mbsf can recover a maximum length $L_{\text{max}} = 60\text{ cm}$ of un-cemented sediments. On the other hand, long hydrate bearing sediments cores can be recovered when no un-cemented layers plug the sampler.

2.6 Experimental Study

A near surface sampling test was conducted on Lake Acworth, GA (coarse grained soil) and in a fill at Georgia Tech (fine grained soil) to validate the expected recoverable length in un-cemented soil using a small radius sampler.

Set-up and Procedure: two driving conditions were tested. The first one consists of driving two different samplers into sand with a hammer (dynamic penetration). The second test uses a continuous push. This system implies a reaction frame, with three ground anchors, an Enerpac hydraulic cylinder, and a load cell to record penetration forces (Figure 2.12). The water table is 5 cm below the surface.

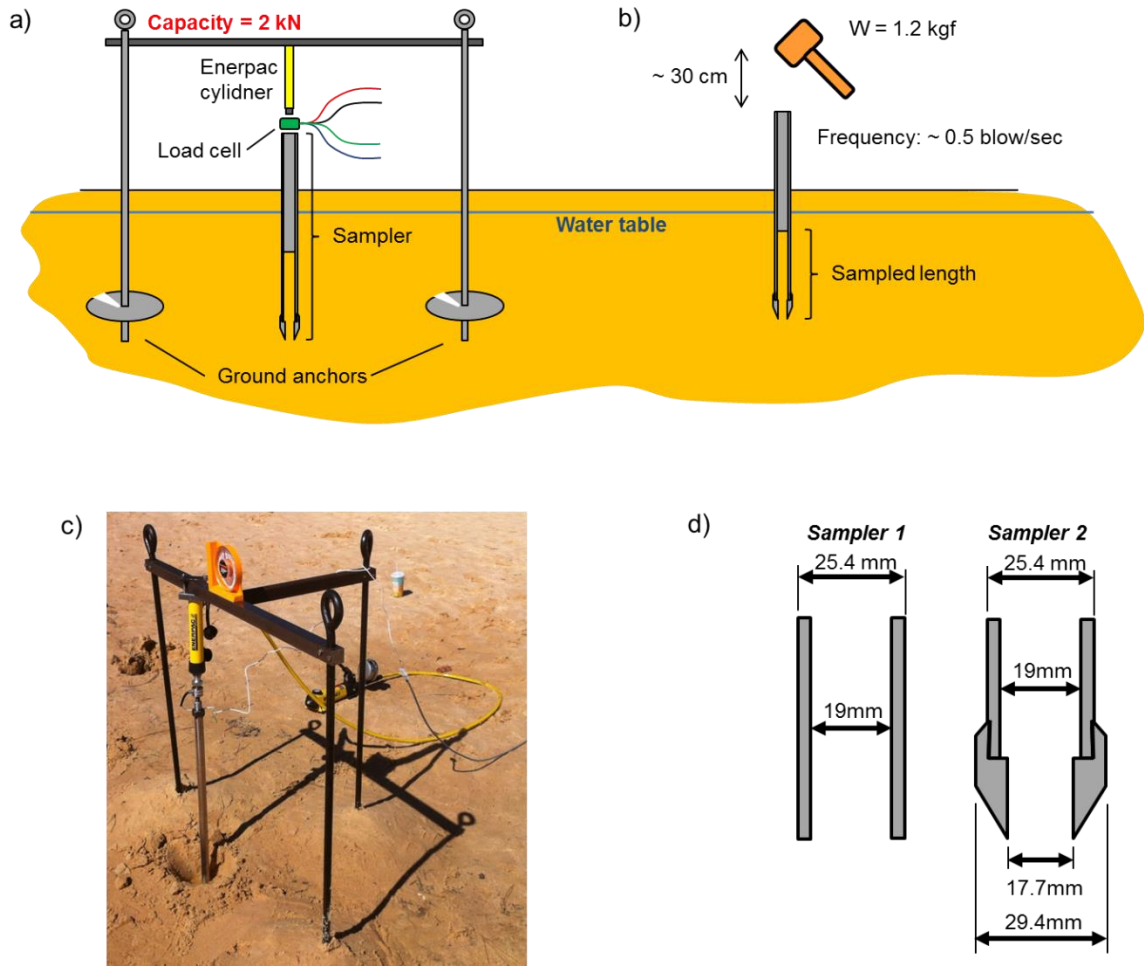


Figure 2.12. Core recovery with small sampler – Field study: (a) Continuous push schematics. (b) Dynamic driving. (c) Picture at the site. (d) Samplers dimensions.

Two samplers were tested using both penetration methods. Sampler 1 is a 25 mm open ended pipe hence its inside clearance $C_i = 0$. Sampler 2 is a specially designed sampler for the recovery of disturbed samples from hydrate bearing sediments; it has a cutting shoe with $\alpha = 10^\circ$ angle and a reduction of the internal diameter so that the inside clearance ratio is $C_i = 3.7\%$. No catcher was used with either sampler.

Results: Figure 2.13-a shows sampled lengths obtained with the two driving methods, both samplers, and soil types. Each test was repeated 5 times. The box represents the median, 25th and 75th percentile of test results, while the segments run from the

maximum and the minimum recorded values.

Results confirm the benefits of dynamic driving over pushing to gather longer samples, as discussed in the review (Section 2.2.1). Sampler 2, with the sharp cutting shoe and internal clearance delays frictional build up and leads to longer samples in both static and dynamic modes. The internal clearance facilitated the extrusion of the sample after testing in the case of fine grained soil.

The expected plug length is also shown here for cases of friction angles of $\phi = 20^\circ$ and $\phi = 35^\circ$ (from Figure 2.11 and Eq. 2.29); they agree well, particularly with data gathered with sampler 1 (i.e. a pipe without a cutting shoe).

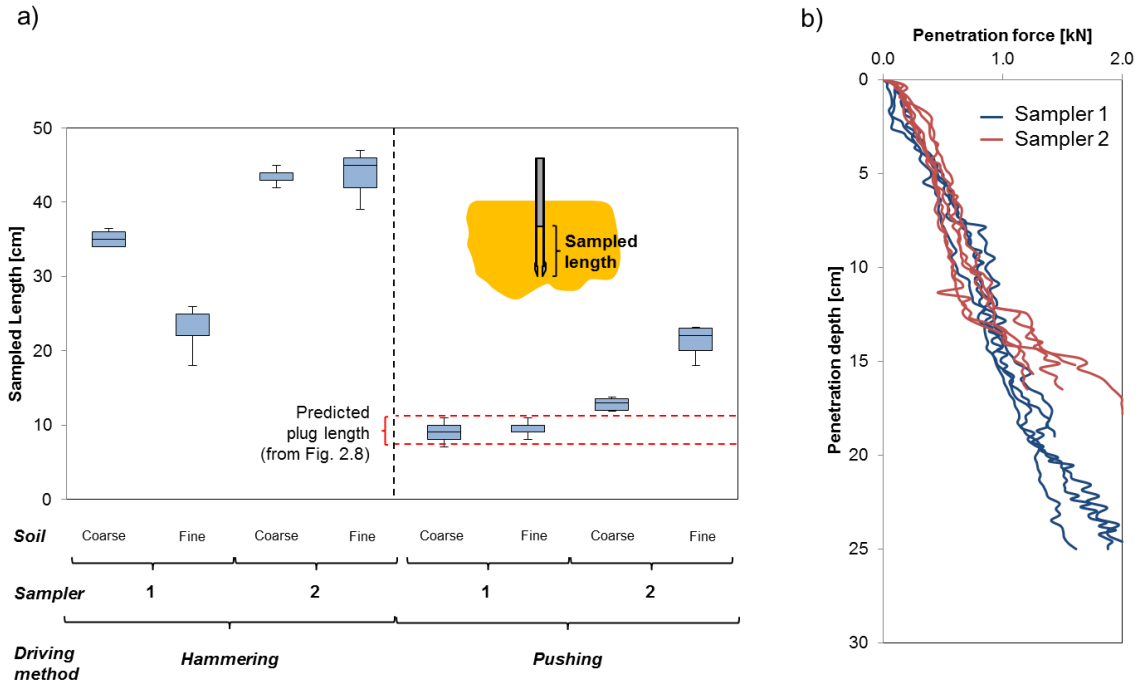


Figure 2.13. Core recovery with small sampler – Results: (a) Sampled length (distance measured before removing the sampler from the ground). (b) Penetration force vs. depth. There is no clear evidence of significant differences between the two samplers.

The penetration force was recorded to the maximum load cell capacity (2 kN; Figure 2.13-b). The penetration forces increase quasi-linearly with depth, as expected for frictional materials, and there is no evident difference between the penetration

resistances exhibited on both samplers with different cutting shoes.

2.7 Conclusions

Sampling and coring disturb sediments and alter sediment properties. Lateral stress relaxation and plugging were studied to develop robust guidelines for the design of coring equipment to be used to sample hydrate bearing sediments. Results show:

- The internal gap determines the balance between lateral relaxation and wall friction.
- Typical samplers used in geotechnical practice have a large gap and are not adequate to recover long cores from hydrate bearing sediments.
- Plugging should be expected with all samplers. Experimental results show plugging in all type of soils. A recoverable length of $z/r_s = 10-15$ should be expected.
- Dynamic driving is preferred to recover long samples, particularly when the insertion velocity exceeds 1 cm/sec.
- Sampled lengths reported in the literature, agree well with values predicted using the plugging limit.
- Soil-sampler interaction parameters affect the predicted plugging length. Values of $\beta = 0.11$ up to 0.17 can be adopted.

CHAPTER 3

PRESSURE CORE CHARACTERIZATION TOOLS FOR HYDRATE-BEARING SEDIMENTS

This chapter was published in abbreviated form in Santamarina et al. (2012), which was co-authored with Dr. S. Dai and Dr. J.B. Jang at Georgia Tech. The pressure core characterization tools were successfully deployed in January of 2013 for the study of methane hydrate bearing sediments in the Nankai Trough region, offshore Japan. The author was solely responsible for the design, manipulation, operation and analysis of the direct shear chamber and the guillotine; in addition, he played a direct role in the design and verification of all other components.

3.1 Introduction

Natural gas hydrates form under high fluid pressure and low temperature, where biogenic or thermogenic gases are available. These requirements delimit the distribution of hydrate bearing sediments to sub-permafrost, deep lakes (theoretical water depth greater than ~390 m) or ocean sediments (theoretical water depth greater than ~320m). Typically, hydrates are found in deeper water columns due to thermal fluctuations, and diffusion near the sediment surface (Xu and Ruppel 1999).

The clathrate or cage-like structure formed by water molecules hinders the repulsion between gas molecules and allows for high gas concentration: there is one molecule of methane for every 5.75 molecules of water in CH₄-hydrate, compared to the solubility of methane in water which is in the order of 1-in-750. With such a high methane concentration, natural gas hydrates can become an energy resource and remains a potential source for a potent green-house gas.

Depressurization and/or heating across the phase boundary causes hydrate dissociation. The hydrate volume expands multiple times just to cross the phase

boundary; for example there is a 1.3-times expansion under Blake Ridge pressure-temperature P-T conditions, and 4-times expansion in the shallower Hydrate Ridge formation. Rapid volume expansion brings the sediment to failure in low permeability formations, triggering wellbore and even large scale seafloor instabilities.

Dissociation, volume expansion and the ensuing sediment deconstruction dramatically affect the ability to characterize hydrate-bearing sediments. Indeed, proper characterization requires coring, recovery, manipulation and testing under P-T conditions within the stability field. Pressure core technology has been advanced to address this need.

3.2 Pressure Core Technology: Overview

Coring and Recovery. The development of pressure coring and recovery tools have involved research teams around the world, including initiatives such as the International Ocean Drilling Program and the European Union's Marine Science and Technology Program (Kvenvolden et al., 1983; Pettigrew 1992; Amann et al., 1997; Dickens et al 2003; Qin et al., 2005; Schultheiss et al., 2009). Push-piston (clay bearing sediments) and rotary coring (sands with high hydrate saturation) methods have been developed to gather several meter long pressure cores. The core slides inside a plastic liner during coring to facilitate its manipulation after recovery. The in situ fluid pressure is maintained by a ball valve that closes the barrel beyond the core-catcher; the ball valve seal is critical to reliable pressure core recovery. While temperature control is also possible (PTCS - Kawasaki et al., 2006), analytical and field results show that the additional complexity of temperature control is unnecessary as long as the barrel is rapidly cooled once it reaches the surface.

Manipulation. Earlier studies using pressure cores required fast depressurization and stabilization in liquid nitrogen before transferring the core into testing chambers. Such drastic changes in pressure and temperature can be prevented if all operations after

recovery are conducted under P-T conditions within the stability field to prevent dissociation. Pressure core manipulation and transfer technology requires a longitudinal positioner/manipulator and ball valves to couple components at equalized pressures (Pressure Core Analysis and Transfer System PCATS - Schultheiss et al., 2006).

Testing and Characterization. Testing and characterization tools were developed in parallel to manipulation capabilities. Non-contact characterization tools are based on gamma density, X-rays and water-coupled P-waves (Pressure Multi-Sensor Core Logger - Schultheiss et al., 2006; see also Abegg et al., 2008). Contact/invasive tools allow for the assessment of stiffness using P-and S- wave velocities, strength, electrical resistivity profiles and internal core temperature (IPTC - Yun et al., 2006); contact measurements require pre-drilling the plastic liner under pressure at the locations where measurements will be conducted. Subsampling capabilities have also been developed for biological studies under in situ P-T conditions (DeepIsoBug - Parkes et al., 2009).

Current Situation. Other characterization needs have gradually surfaced driven by the enhanced understanding of hydrate bearing sediments, the renewed interest in gas production and related engineering tasks, and the increased reliability of pressure core recovery. Pressure core characterization tools developed at the Georgia Institute of Technology are described next.

3.3 Pressure Core Characterization Tools

Our pressure core characterization system includes both core manipulation tools and characterization chambers. Tools have been selected to obtain complementary information relevant to science and engineering needs, with emphasis on the measurement of parameters used in hydro-thermo-mechanical analyses.

All tools are designed following key guidelines and objectives: simple and robust systems, portable components for fast deployment, modular design for maximum flexibility, standard dimensions and parts for economic construction and maintenance,

rust-resistance for seawater environment (all devices are made of stainless steel 316), can hold 35 MPa fluid pressure and operate at 21 MPa, capable to impose effective stress when physical parameters are effective stress dependent, and safe for the monitoring of hydrate dissociation and gas production during controlled depressurization, heating or fluid exchange (such as with liquid CO₂). The modular design implies geometrically compatible chambers and components developed with the same design philosophy; in particular, any two tools/chambers can be readily coupled through an identical flange-clamp system.

3.3.1 Manipulator (MAN).

The manipulator is a longitudinal positioning system that is used to grab and move the core along the interconnected chambers and valves as needed, always under the required P-T conditions. Figure 3.1 shows the typical operation sequence used to retrieve a specimen from the storage chamber into the manipulator followed by displacing core into a generic test chamber. The geometric analysis of the operation shown in Figure 1 reveals that the length of the manipulator L_{man} (with its “temporary storage chamber”) is proportional to the length of the core L_{core} to be manipulated, $L_{man} \approx 3.5 \cdot L_{core}$. If an external positioning system is used, the rod must undertake the force due to the fluid pressure and the force required to displace the core; such a design is typically limited by buckling even when an open ended hollow tube is selected. Our system is designed to handle $L_{core} = 1.2$ m long cores, uses an internal telescopic screw system (stroke = 2.6m) driven by an external stepper motor, and can position the specimen with sub-millimetric resolution. It is coupled to the 1.3 m long temporary storage chamber by means of a dismountable flange-clamp connection. A see-through port is included to confirm the position of the manipulator at any time.

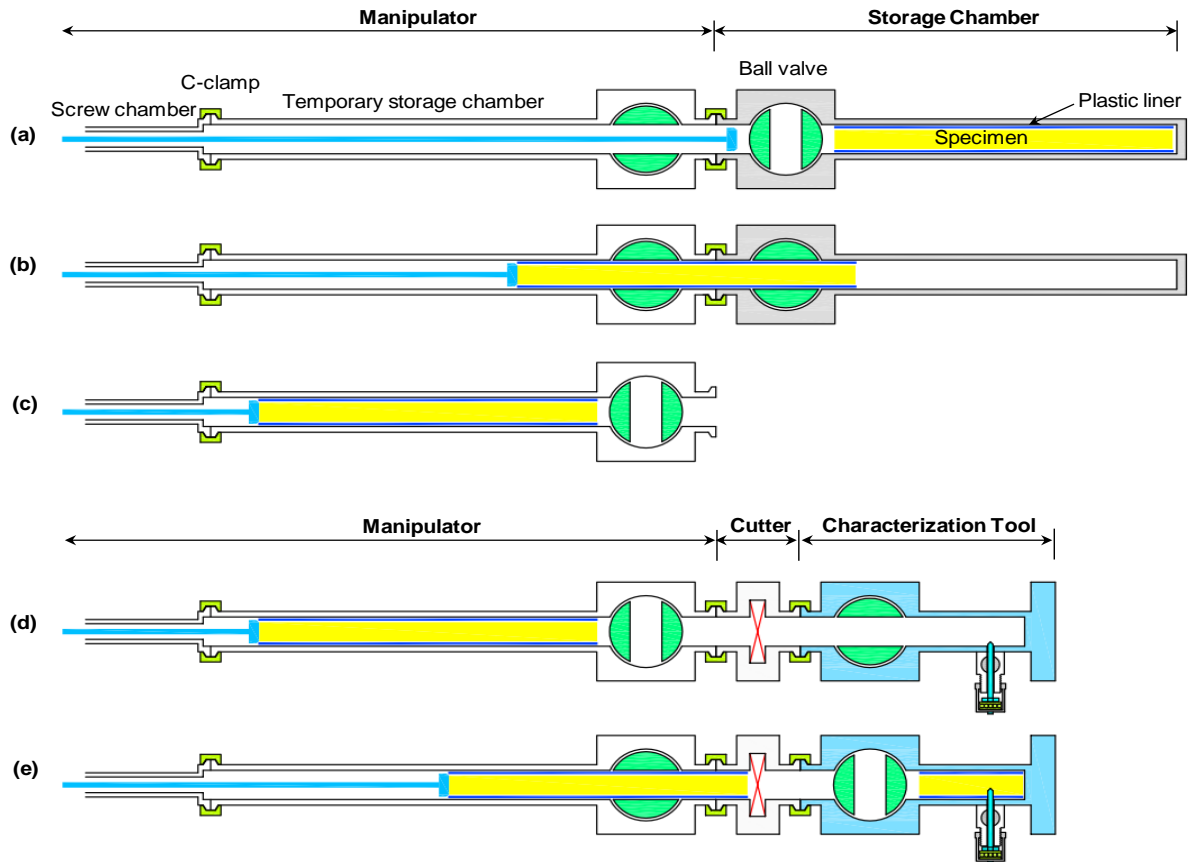


Figure 3.1. Pressure core manipulation. (a) The manipulator MAN couples with the storage chamber and fluid pressures are equalized at the target pressure p_0 before opening the ball valve. (b) The manipulator captures the core and transfers it into the temporary storage chamber. (c) Ball valves are closed and the depressurized storage chamber is separated. (d) The selected characterization tool is coupled to the manipulator and is pressurized to p_0 . (e) Ball valves are opened and the core is pushed into the characterization tool; stand-alone characterization tools may be detached after retrieving the rest of the core and closing valves. Note: the cutter tool CUT is shown in panes d&e; it is attached in series to cut core to any desired length to meet tool requirements (for stand-alone ESC, DSC, CDP, and Bio tools).

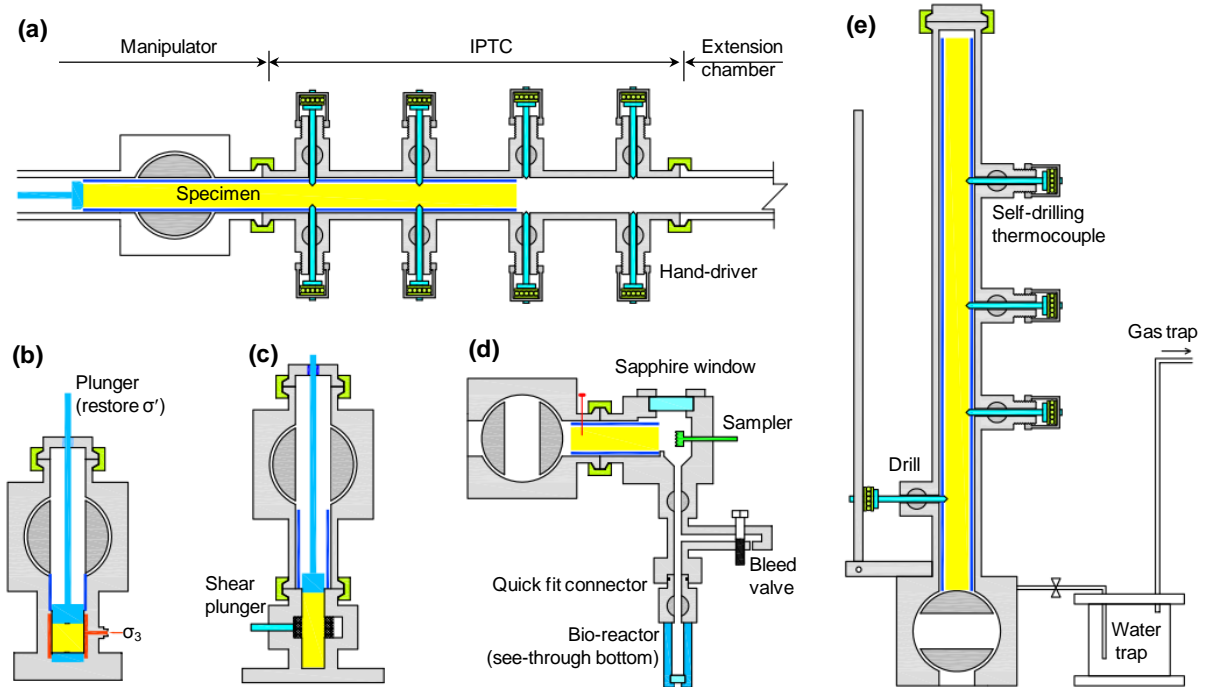


Figure 3.2. Schematic diagrams of characterization chambers. (a) IPTC instrumented pressure testing chamber with P-T control. (b) ESC effective stress chamber with σ' -P-T control. (c) DSC direct shear chamber with σ' - τ -P-T control. (d) CDP controlled depressurization chamber for sediment preservation and gas production. (e) BIO sampler for multiple bio-reactor chambers. Scale: the outside diameter of the large ball valve shown in all devices is OD = 220 mm.

3.3.2 Sub-sampling (CUT)

The 1.2m long core can be cut into short specimens. Our cutting tool CUT houses either a linear or a ring-shaped saw-blade within a clamp-type chamber. The saw-based cutting ensures clean surfaces and minimizes specimen disturbance. The cutting tool CUT is mounted in series between the manipulator and any other test or storage chamber as needed (Figure 3.1e).

3.3.3 Instrumented Pressure Testing Chamber (IPTC).

The chamber was developed to measure P&S wave velocities, undrained strength, electrical conductivity, internal core temperature, and to sample fluids (Figure

3.2a - details in Yun et al 2006). This cylindrically-shaped chamber has two sets of four diametrically opposite port pairs. The first pair drills holes (ID = 8mm) in the plastic liner so that contact probes in successive ports can be pushed into the specimen. In characterization mode, the IPTC is coupled to the manipulator on one side and an extension chamber on the other end, and measurements can be conducted at any position along the core length. The eight access ports make the IPTC a versatile chamber for conducting well-monitored production studies in view of reservoir calibration models.

3.3.4 Effective Stress Chamber (ESC).

Pressure cores are recovered and stored at fluid pressure and temperature P-T conditions needed to preserve hydrate. However, physical properties such as stiffness and shear strength are a function of both hydrate saturation and effective stress (Note: the relative relevance of effective stress increases as hydrate saturation decreases).

The effective stress chamber ESC maintains P-T stability conditions and restores the effective stress σ' that the sediment sustains in situ (Figure 3.2b). It was designed and laboratory-tested at Georgia Tech in 2006 under Joint Oceanographic Institutions JOI sponsorship, and it was first deployed in the field by the Korean Institute of Geoscience & Mineral Resource KIGAM in collaboration with Geotek during the UBGH1 expedition (Lee et al., 2009).

The original design was based on a zero-lateral strain boundary condition. We have updated this chamber to accommodate a stress-controlled boundary condition using a jacket (Figure 3.2b). The resulting triaxial stress configuration consists of σ_3' applied with the jacket and σ_1' applied by a piston that is advanced through the ball valve and acts directly onto the pressure core. The piston and the base pedestal house the sensors needed for the measurements of physical properties, including stiffness (wave velocities), thermal conductivity, and electrical resistivity.

A salient advantage of the flexible wall configuration is the ability to conduct

precise fluid conductivity measurements by preventing the preferential flow along the sediment-steel boundaries in rigid-wall chambers. This chamber is particularly well suited to monitor production studies under in situ effective stress conditions, including the assessment of sediment volume change upon dissociation.

3.3.5 Direct Shear Chamber (DSC).

Note: The DSC is reported in detail in Chapter 4; the brief summary presented herein complements the description of the complete set of pressure core characterization tools PCCTs.

The shear strength of hydrate-bearing sediments under in situ pressure, temperature and effective stress conditions is a necessary parameter for constitutive models.

Two constraints guided the design of the DSC tool. First, the imperfect boundaries that result when cutting heterogeneous cores under pressure cause stress concentration during vertical loading; thus, we selected a “double direct shear” geometry to cut across the specimen away from end effects. Second, overcutting during coring leaves a gap and the core tends to tilt during shear; then, we adopted a double shear plane configuration to avoid bending action. Consequently, the direct shear chamber consists of a thick wall stainless steel ring that is pushed to shear the central third of the specimen (Figure 3.2c). The DSC includes the piston to restore effective stress (self-reacting vertical frame - similar to the ESC), a liner trap to capture the plastic liner before the specimen enters the shear chamber, and a small lateral built-in frame to push the side piston that displaces the ring (Figure 3.2c). The maximum shear displacement is $\delta_{max} = 15\text{mm}$ so that both peak and residual shear strengths can be determined.

The test sequence includes: (1) shear under in situ vertical effective stress and P-T conditions, (2) push the ring back to its original position, (3) monitor hydrate dissociation and gas production at constant vertical effective stress and zero-lateral strain

boundary conditions, and (4) shear the specimen again to determine the hydrate-free residual shear strength. The complete data set provides strength and volume change data under in situ conditions that are necessary for model calibration, production design and stability analyses

3.3.6 Sub-sampling Tool for Bio-Studies (BIO).

The study of bioactivity in deep-water sediments without incurring in depressurization cycles is crucial to the survival of some barophilic microorganisms. The BIO chamber is loaded with a core segment using the manipulator; afterwards, it is detached from the manipulator for all successive procedures (Figure 3.2d). Its operation involves (1) Nitrogen-liquid replacement, (2) core face cleaning and chamber fluid-based sterilization, (3) sub-sampling using a rotary sampling head, and (4) sample release into the bio-reactor that is pre-filled with nurturing solutions (volume = 10 cc). All operations can be observed through a sapphire window. Bio-reactors are readily replaced by closing a system of two ball valves and decoupling the quick connect fitting in between. This device allows the collection of a large number of specimens from a single core segment under in situ hydrostatic pressure.

3.3.7 Controlled Depressurization Chamber (CDC).

Successful pressure coring operations may produce more pressure cores than the available storage. In this case, recovered cores are selectively de-pressurized to conduct further studies under atmospheric pressure. The controlled depressurization chamber is designed to help preserve the core lithology and to gain valuable information during depressurization, with minimal demand on personnel resources. This stand-alone device has a built-in drilling station to perforate the liner at selected locations in order to reduce the specimen longitudinal expansion. A pressure transducer and a thermocouple monitor the gas P&T conditions inside the chamber. In addition, three self-drilling thermocouples

are built-in along the CDC; these are driven into the core to monitor the internal sediment temperature during depressurization. Finally, a 2 L water trap and a 55 L gas trap are attached in series to the needle valve that controls the rate of depressurization; these traps sit on scales to monitor produced water and gas (Figure 3.2e).

3.4 Measurement of Physical Properties

Multiple sensing systems have been developed to characterize the sediment and to determine hydro, thermo, chemo, bio, and mechanical parameters within the chambers, under controlled pressure, temperature, and effective stress conditions as described above. Not all sensors or gadgets are available for all chambers, yet, their deployment in various devices support the comprehensive characterization of natural hydrate-bearing sediments under in situ pressure, temperature, and/or stress conditions, and permit detailed monitoring of gas production tests.

3.4.1 Tool Position Control.

All contact instruments, sensors and drills are mounted on polished rods (diameter $d=7.9\text{mm}$) which are advanced into the specimen using externally controlled screw-based positioning systems to overcome the 1.7 kN force at the maximum working fluid pressure of 35 MPa (Figure 3.3). The hand-operated driver advances along the threaded guide while pushing the tool rod. The ball valve between the threaded guide and the chamber permits replacing tools under pressure (Figure 3.3).

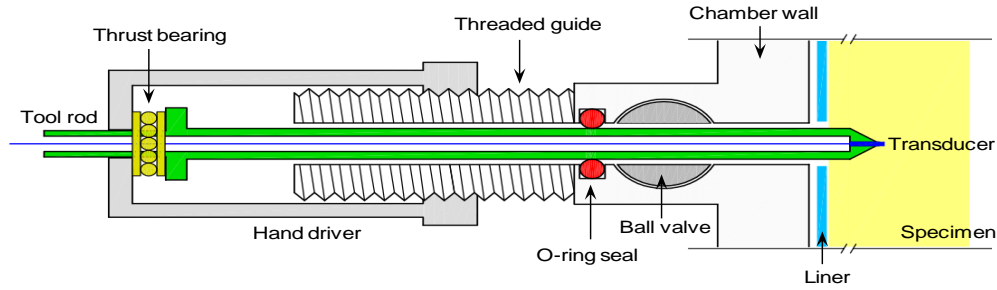


Figure 3.3. Tool Control. The displacement of sensors, subsampling tools and drills are controlled under pressure using a screw-based positioning system where the driver advances along the threaded guide while pushing the tool rod (shown in green). Transducers at the tip of the rod are wired through the central hole in the tool rod.

3.4.2 Sensors.

Transducers are mounted at the tip of tool rods and wired through the central bore. Available instruments are shown in Figure 3.4. Small-strain wave velocity measurements employ bender elements for S-waves and pinducers for P-waves (Figures 3.4a&b –peripheral electronics and test procedures as described in Lee and Santamarina, 2005 a&b).

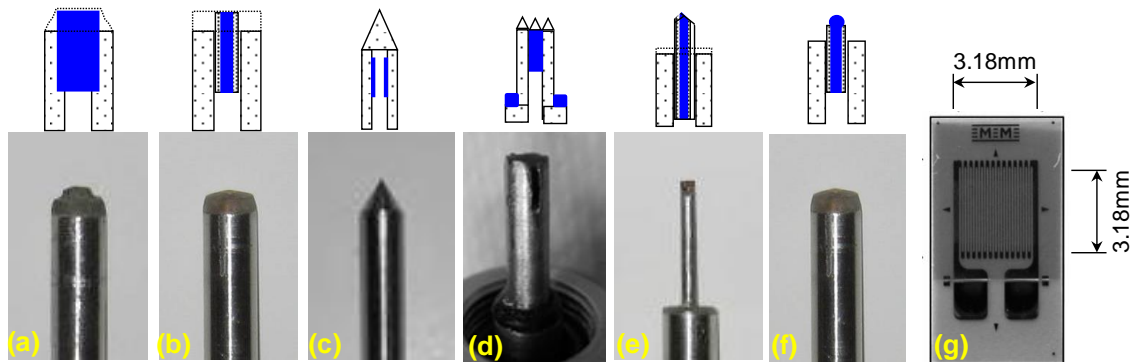


Figure 3.4. Measurement tools and sensors. (a) Bender elements for S-wave generation and detection. (b) Piezocrystals for P-waves. (c) Penetrometer for strength measurement. (d) Pore fluid sampler. (e) Electrical needle probe for resistivity profiling. (f) Thermocouple instrumented tip. (g) Strain gauge for thermal conductivity determination (TPS – NETL; Rosenbaum et al. (2007)).

While large-strain strength data can be gathered using the direct shear chamber (DSC – Figure 3.2c), we have developed a strength-penetration probe as well (Figure 3.4c). This

device determines the sediment strength using a cone-shaped stud equipped with a full-bridge strain gauge inside. The measured tip resistance during probe penetration reflects the sediment undrained shear strength (details in Yun et al., 2006).

Fluid conductivity can be determined using the flexible wall system built within the effective stress chamber ESC (Figure 3.2b), and inferred using the fluid sampling tool (Figure 3.4d). This is a self-drilling drainage port with a pressure or volume control flow condition to drive the interstitial fluids out of hydrate-bearing sediment. The pressure difference can be selected to preserve hydrates within stability conditions.

Electrical resistivity is measured using an electrical needle probe that is gradually inserted into the specimen to determine a radial resistivity profile with millimeter-scale spatial resolution (Figure 3.4e – details and measurement procedure in Cho et al., 2004). We have also developed a multiple electrode system at the base of the effective stress cell that allows us to conduct a surface-based electrical resistivity tomography within a specimen.

The thermal probe consists of a thermocouple deployed at the tip of a tool rod. When pushed into the sediment, the thermal probe monitors the temperature inside the core (Figure 3.4f). The self-drilling version of this probe, deployed in the controlled depressurization chamber CDC, places the thermocouple inside a hollow drill tip at the end of a tool rod. Internal temperature measurements can be used to monitor phase transitions during controlled gas production studies and to determine thermal conductivity (by inversion for given imposed boundary conditions). In addition, the TPS sensor for thermal conductivity measurements developed at NETL (Figure 3.4g, Rosenbaum et al 2007) can be installed at the tip of tools or on the pedestal of the effective stress and direct shear chambers.

3.5 Monitoring Dissociation – Gas Production

All PCCTs chambers allow core-scale gas production tests by either de-

pressurization, heating, or chemical injection (e.g., inhibitors or carbon dioxide). Monitoring data include pressure, temperature, produced gas and water, stiffness (seismic wave velocities), fluid conductivity, and electrical resistivity. Figure 3.5 shows examples of data gathered during the depressurization of natural hydrate-bearing sediments.

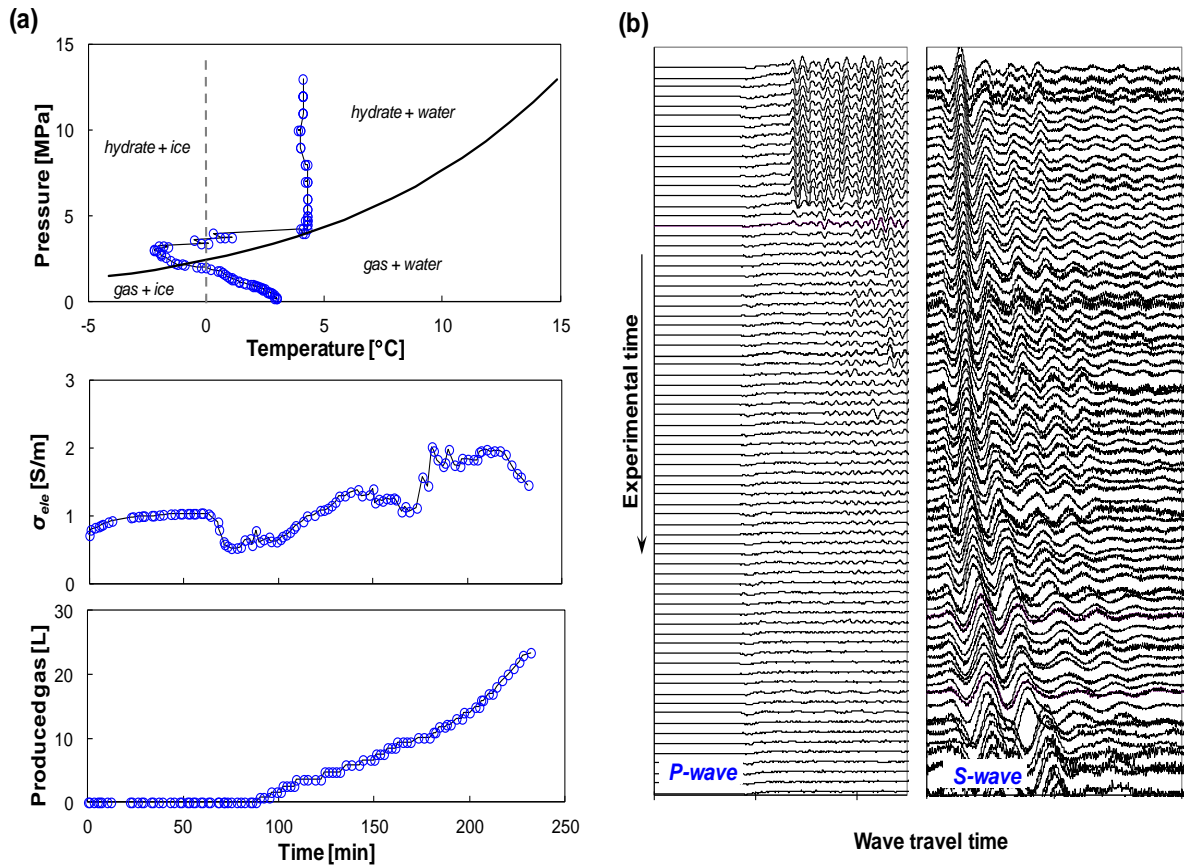


Figure 3.5. Monitored gas production tests using IPTC: (a) Evolutions of pressure, temperature, electrical resistivity, and produced gas (Krishna-Godavari Basin, (Yun et al., 2010)); (b) Typical wave signatures during gas production: P-wave signatures eventually fade out after gas production; S-waves detect the evolution of the skeleton shear stiffness during hydrate dissociation and gas production (Ulleung Basin, Yun et al. 2011).

3.6 Discussion: Comprehensive Characterization Approach

Pressure coring, recovery, and testing prevent hydrate dissociation and its catastrophic consequences on sediment structure. However, inherent sampling effects

caused by unavoidable changes in effective stress remain. These changes are quite prominent and include: stress relaxation from lithostatic confinement to virtually no effective stress, the potential for internal fluid pressure drop and local dissociation even when chamber P-T conditions are within the stability field (i.e., a form of poro-elastic Mandel-Cryer effect coupled with phase transition), side friction along the liner, skeleton expansion and the potential for stain-induced decementation.

Clearly, in-situ testing can play an important role in the characterization of hydrate bearing sediments. However, in situ tests face their own technical challenges and interpretation difficulties, including the effect of tool insertion on measured properties.

Based on these observations and field experiences (Gulf of Mexico, Krishna-Godavari Basin, Ulleung Basin, and Mount Elbert), the comprehensive characterization of hydrate-bearing sediments should include: (1) detailed analysis of available logging data, (2) pressure core characterization and monitored de-pressurization, (3) index properties (with emphasis on grain size distribution and fines content, specific surface, SEM microphotographs, mineralogy and plasticity, pH and pore fluid ionic concentration), and (4) laboratory tests on reconstituted specimens with synthetic hydrate saturation to determine the behavior of sediments as a function of effective stress and hydrate saturation (including: stiffness, strength, and hydraulic conductivity).

Index properties -analyzed within the framework of accumulated field and laboratory data- provide exceptional information related to hydrate pore habit and morphology, potential sediment properties and production-related information including the possibility of fines migration (Refer to Waite et al., 2009 for a comprehensive review of hydrate-free sediment properties).

The reconstitution of hydrate bearing sediments is hindered by inherent difficulties in forming methane hydrate from dissolved phase methane. Tetrahydrofuran THF presents important advantages as a proxy hydrate former (Lee et al., 2007). First, its complete miscibility in water enables accurate hydrate saturation control and fast hydrate

formation from dissolved phase (i.e., no preferential formation at interparticle contacts). Second, THF hydrate forms at atmospheric pressure and standard geotechnical devices can be used to characterize hydrate bearing sediments.

3.7 Conclusions

- Pressure core technology is needed for the proper evaluation of natural hydrate bearing sediments.
- The set of pressure core characterization tools PCCTs described in this review allow the manipulation, sub-sampling, and extensive assessment of natural gas hydrate bearing sediments under in situ pressure, temperature, and effective stress conditions.
- In addition to pressure core testing, comprehensive characterization programs should include sediment index properties analyzed within the framework of available data for natural hydrate bearing sediments, and tests with remolded specimens with synthetic hydrate.
- Pressure core technology can also be deployed to study other gas rich hydrocarbon formations such as deep sea sediments, coal bed methane and gas shales.

CHAPTER 4

PHYSICAL PROPERTIES OF METHANE HYDRATE BEARING SEDIMENTS: NANKAI TROUGH DEPLOYMENT

4.1 Introduction

There is increased interest in the potential recovery of methane from hydrate bearing sediments. Extraction methods could involve: depressurization, heating, inhibitor injection (including CO₂ replacement) or combined methods (Moridis et al. 2009). The reservoir characteristics and properties are needed for the proper design of extraction methods. Geophysical and wire-logging methods provide valuable information averaging values over large distances and properties are often inferred through correlations.

Methane hydrates are stable under high pressure and relatively low temperature, thus they are found in marine sediments and permafrost regions. Coring, sampling, and sample characterization are challenged by conditions required for stability. Pressure core technology has been developed to overcome these limitations: the main goal is to maintain the specimen within the stability field at in-situ pressures and temperature conditions at all times.

This chapter describes a new Direct Shear Chamber DSC designed to measure the physical properties of hydrate bearing specimens recovered using pressure core technology. The device is used to measure the shear strength at large displacements, P-wave, compressibility before and after dissociation, and volume contraction upon dissociation. In addition, this device can be used to gain information during dissociation. Specimens recovered from the Nankai Trough, Japan, were tested using this device.

4.2 Direct Shear Chamber: Design

4.2.1 Design

The direct shear chamber DSC is designed to measure the shear strength of hydrate bearing sediments under in-situ vertical stress ($\sigma'_{\max} = 12$ MPa for $u = 0$ MPa and $\sigma'_{\max} = 5$ MPa for $u = 30$ MPa) and water pressure ($u_{\max} = 35$ MPa). The device couples with the transfer system through a sealed connector to take a specimen within the plastic liner.

The DSC consists of four parts from top to bottom (figure 4.1-a): the vertical plunger used to restore the in-situ vertical stress, the transfer coupler, the liner trap and the shear box. The vertical plunger is a 25 mm diameter hollow shaft (Figure 4.1-b). The instrumented loading cap houses the piezo-crystals for the P-wave measurements and a thermocouple (Figure 4.1-c). Force is applied on the vertical plunger using a hydraulic piston and an external frame (not shown in the figure); force and displacement are measured using a load cell and a LVDT. The transfer coupler involves a ball valve to isolate the chamber as needed during operation. The vertical plunger extrudes the specimen from the plastic liner into the direct shear box, and the liner remains behind in a specially designed funnel trap.

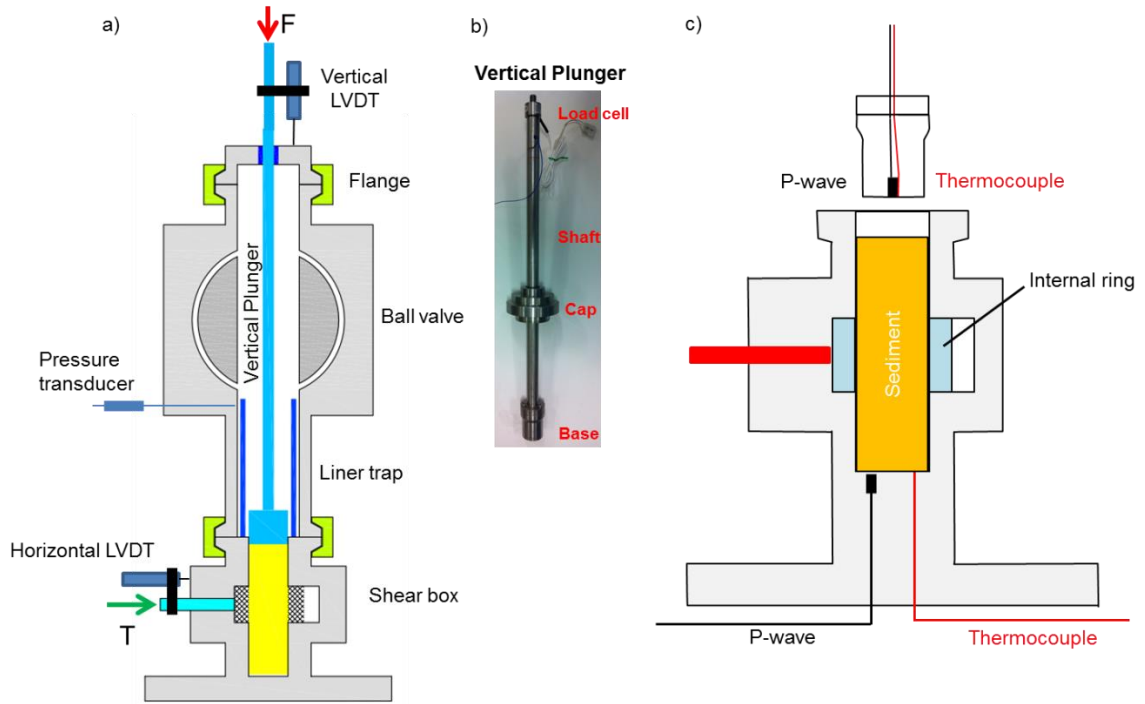


Figure 4.1. Direct Shear Chamber DSC. (a) Cross section. (b) Picture of the vertical plunger and the cap. (c) Transducers, internal ring and specimen.

A two-plane shear box design is selected to avoid boundary effects due to uneven surfaces left by the current sub-sampling tools, and to prevent bending action in one-plane shear systems. The internal thick ring is displaced horizontally to shear the specimen into two planes. The horizontal plunger pushes the internal ring (maximum shear displacement of 15 mm) while the shear force and ring displacement are measured. The horizontal reaction frame is anchored on the stainless steel shear box.

Water pressure, temperature, vertical and horizontal forces, vertical and horizontal displacements, and P-waves are recorded at all times. Figure 4.2 summarizes the instrumentation available in the DSC.

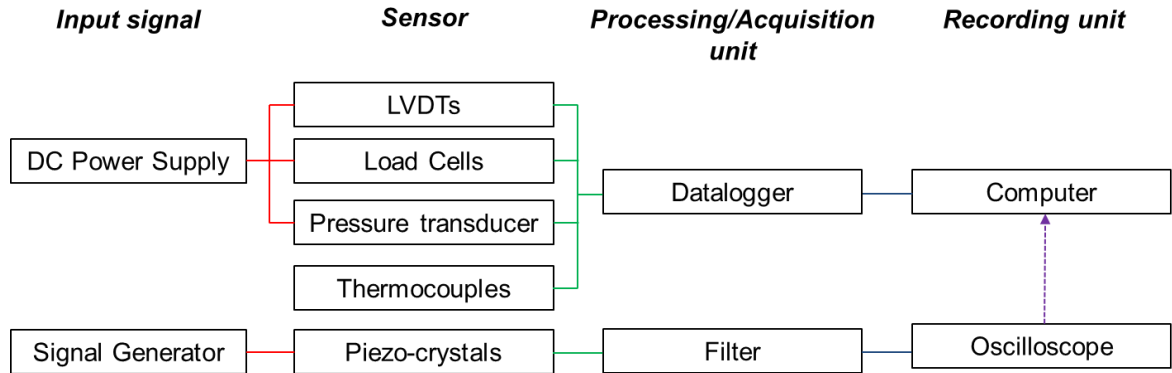


Figure 4.2. Instrumentation in the DSC. The same power supply is used for the LVDTs, load cells and pressure transducer (shared the ground). The datalogger reads output values which are stored in the computer.

4.2.2 Calibration

All transducers used in the DSC were calibrated to the design capacity and tested with saturated sand and frozen sand. A total of 10 samples were tested at different water pressures (up to $u = 20$ MPa) and effective stresses (up to $\sigma' = 5$ MPa for pressurized and $\sigma' = 9$ MPa for dry specimens). In all cases, fluid pressure and effective stress combinations must remain within the chamber capacity (Figure 4.3-c). Figure 4.3-a shows a typical result for a dry specimen used to test and validate this device.

The chamber must be subjected to a leak test every time before a hydrate bearing specimen is loaded for testing (Figure 4.3-d).

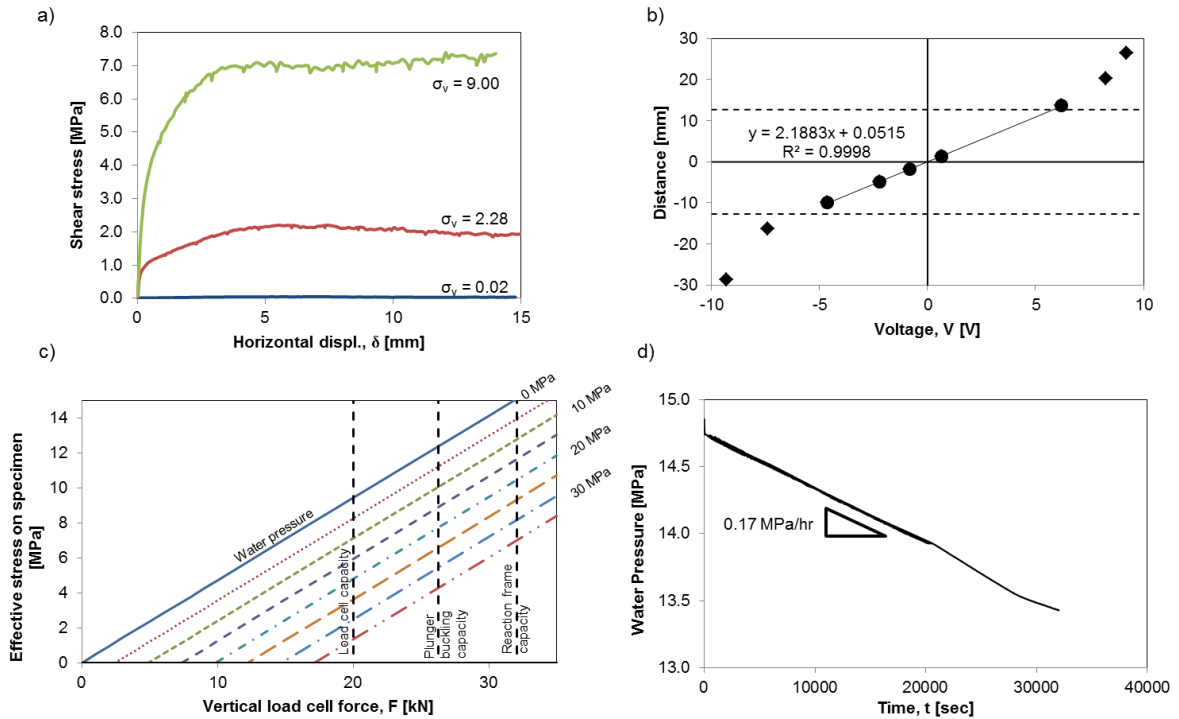


Figure 4.3. Calibration of the direct shear chamber DSC. (a) Typical shear test conducted on dry sand. (b) Typical LVDT calibration showing linear relationship and range of application. (c) Effective stress applied to the sample for each reading of the vertical load cell, with respect to water pressure. Chamber capacity is also shown. (d) Leak test: minor leakage is common as reflected in this response vs. time for a water saturated DSC (Note: this depressurization rate may also reflect early dissolution of trapped gas bubbles).

4.3 Experimental Study: Nankai Trough

4.3.1 Procedure

The transfer and sub-sampling systems described in Chapter 3 are used to load specimens in the DSC under pressure. First, the core is transferred into the temporary chamber in the manipulator MAN. The sub-sampling tool CUT and the direct shear chamber DSC are coupled in series. The MAN displaces the specimen until it reaches the cutting position. A 12 cm to 17 cm long specimen is cut and then displaced into the DSC funnel trap. The ball valve is closed and the DSC is separated from the manipulator

(after the bridge is depressurized).

The DSC is placed vertically and the external vertical frame is attached to the self-reacting chamber. The bridge between the top plunger and the ball valve is pressurized. As soon as pressures are equalized, the ball valve is opened and the vertical plunger is lowered, to extrude the sample from the liner into the shear box. An ISCO pump is connected to the chamber to maintain water pressure constant at all times ($u = 10$ MPa).

4.3.2 Specimens

The Nankai Trough is located 80 km from Atsumi Peninsula, SW of Japan. The Bottom Simulating Reflector BSR is found at a depth of ~ 300 m beneath the seafloor and ~ 1300 m below the sea level (Figure 4.4). The target formation consists of a several meter thick sandy deposit within a turbidic system (Tsuji et al. 2009; Noguchi et al. 2011; and Fujii et al. 2013). The estimated amount of gas in place is 5×10^{11} m³ (Fujii et al. 2008).

Pressure coring was performed from June 29th to July 4th, 2012 (Yamamoto et al. 2012). Pressure cores were kept in a dedicated cold room at $T = 4^\circ\text{C}$ and at a water pressure $u = 20$ MPa. All tests were performed at $u = 10$ MPa to facilitate operations yet well inside stability conditions.

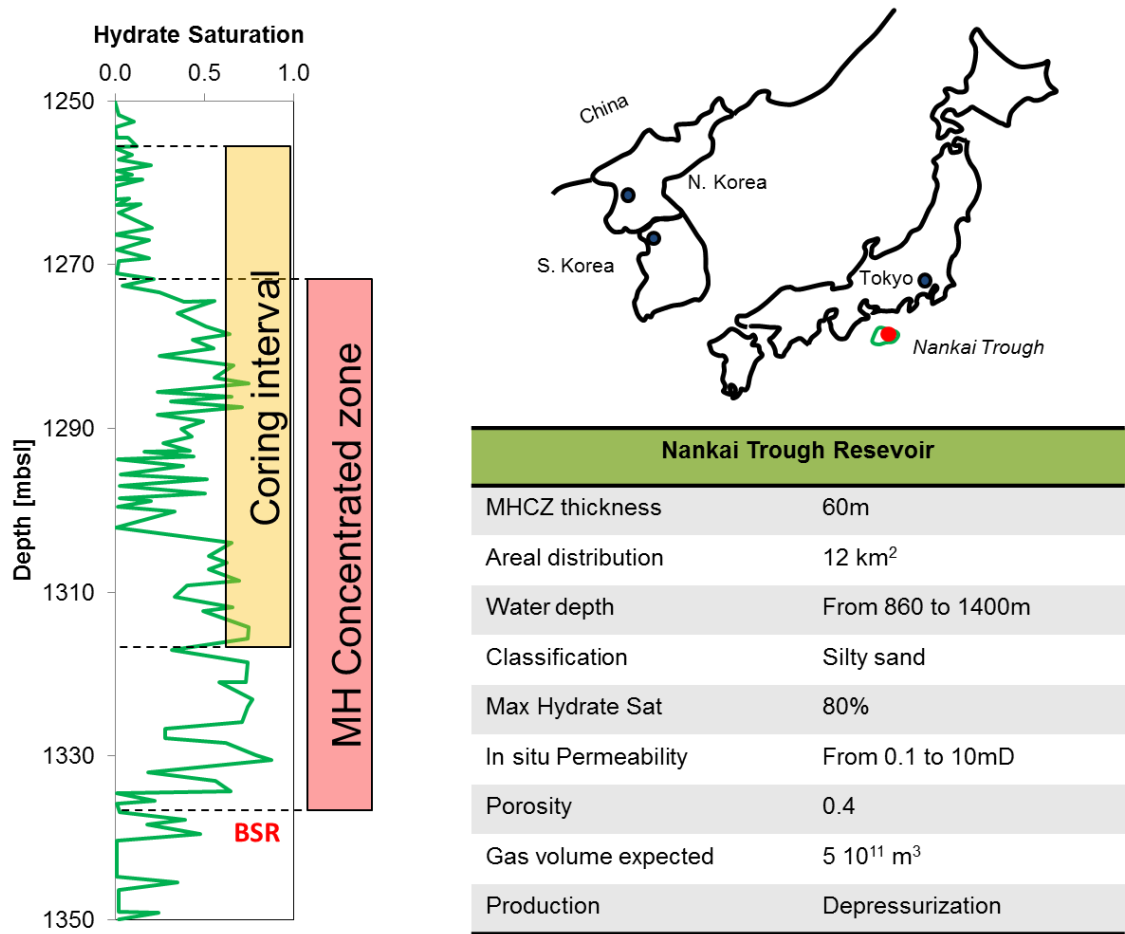


Figure 4.4. Nankai Trough: location, hydrate saturation, coring interval and reservoir characteristics (after Fujii et al. 2013). Note: mbsl = meters below sea level.

The direct shear chamber was used to test 3 samples taken from the top, the middle and the lower layer within the hydrate stability zone (8P, 10P and 20P). Figure 4.5 summarizes sample properties (gathered after dissociation and using conventional laboratory analyses), and X-ray images.

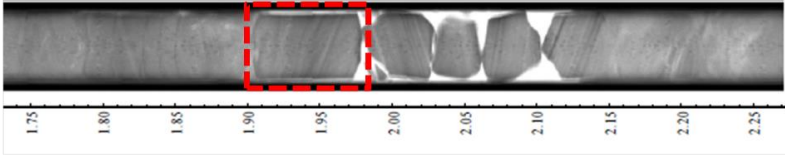
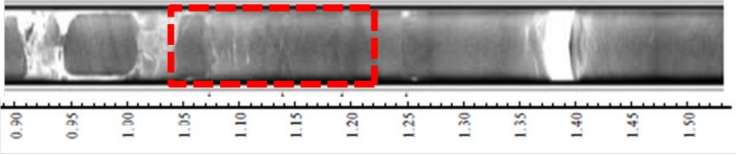
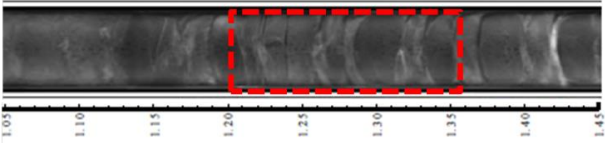
Sample	Core top depth [m]	Overburden [m]	Description
8P	1276.7	278	Silty sand to sandy silt
X-ray image			
			
10P	1282.7	284	Silty sand to sandy silt
X-ray image			
			
20P	1312.7	314	Silty sand to sandy silt
X-ray image			
			

Figure 4.5. X-ray images of tested specimens and properties.

4.3.3 Test Sequence

The test sequence can be synthesized as follows:

- The plunger is used to apply to $\sigma'_z = 3$ MPa vertical stress onto the specimen with simultaneous P-wave measurements.
- A relaxation test is conducted, starting at $\sigma'_z = 3$ MPa of vertical stress. It consists of several load applications (Figure 4.10-a).
- The shear test is conducted at $\sigma'_z = 3$ MPa using a staged-load approach to detect creep in shear. Then, the ring is repositioned to its original zero-displacement position (the vertical stress is temporarily lowered for this step).
- Depressurization driven dissociation. Water pressure, temperature and vertical settlement, P-waves are recorded during depressurization.
- New shear test conducted at $\sigma' = 3$ MPa vertical stress on the sediment without

hydrate.

- Unload and re-position of the internal ring to the zero-displacement condition.
- Reload to 7.5 MPa and conduct a new shear test.

Figure 4.6 shows the test sequence for core 20P during the complete loading history.

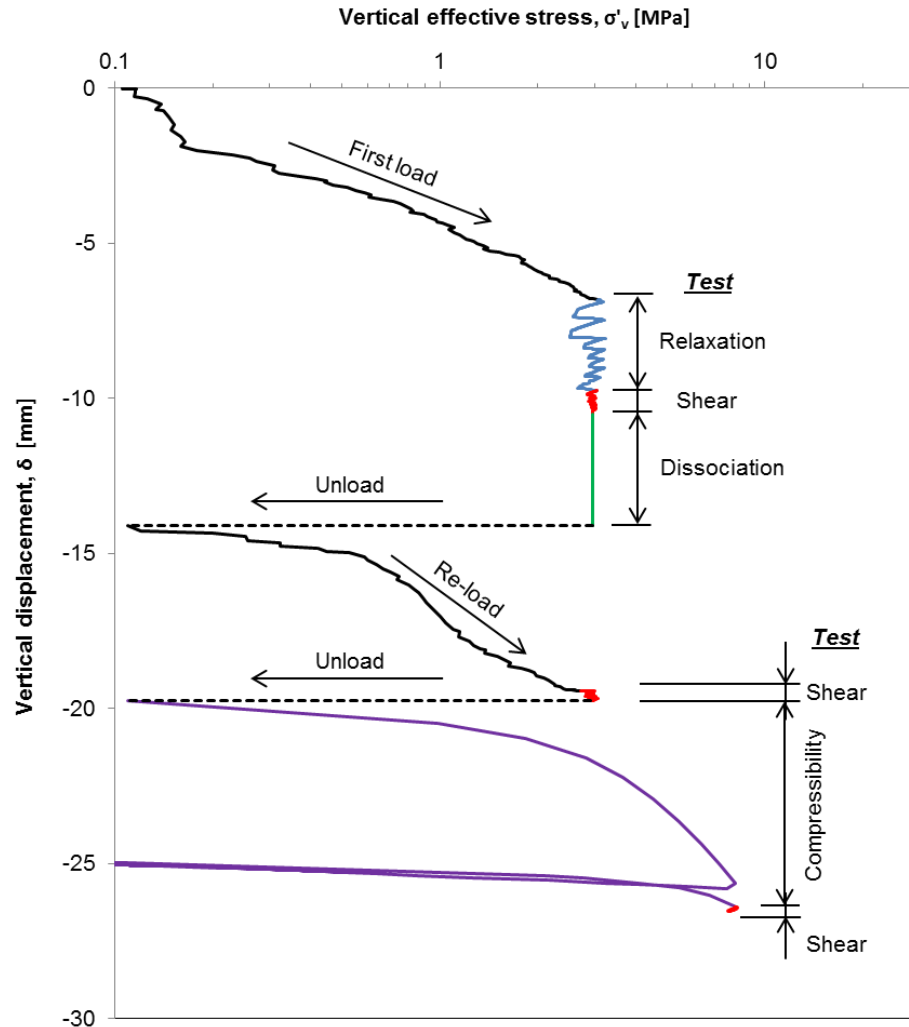


Figure 4.6. Evolution of specimen vertical displacement during the complete loading history for core 20P. Sample initial length = 160 mm.

4.4 Results

Results reported herein are organized in three groups: (1) properties of hydrate bearing sediments, (2) sediment evolution during dissociation, (3) post dissociation

sediment properties.

4.4.1 Hydrates Bearing Sediments

4.4.1.1 Shear Strength

Figure 4.7 shows the applied shear stress vs. testing time for the hydrate bearing specimen 20P obtained during the shear test. Shear stress τ [Pa] is computed as a function of the applied shear force T [N], the cross sectional area A [m²], and the water pressure u [Pa]. No correction factor is applied for the change of the area during shear (Note: sheared sediment rides over the ring)

$$\tau = \frac{T}{2A} - u \quad (4.1)$$

The shear force is applied by imposing one millimeter steps and is permitted to relax between steps. A seating effect can also be noticed during the early stages of the shear loading. Creep takes place in all steps. Figure 4.8 shows the shear stress and the mobilized friction angle.

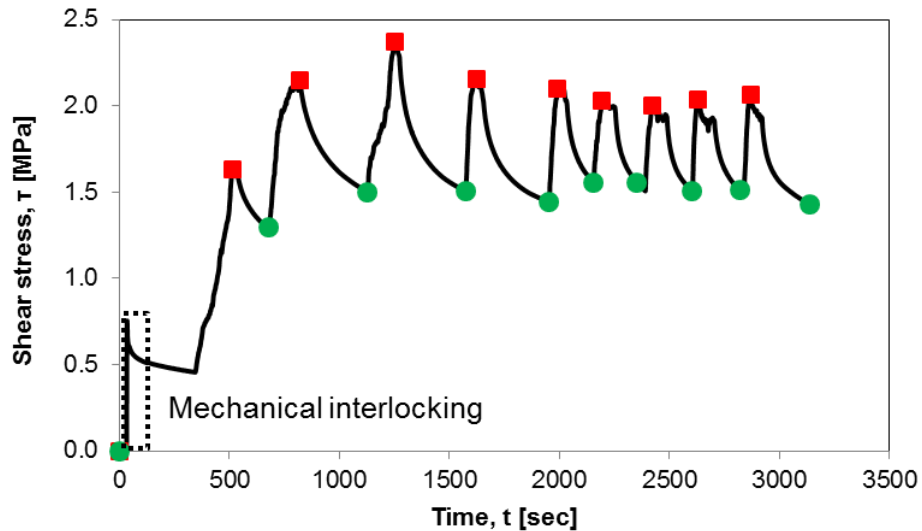


Figure 4.7. Hydrate bearing sediment shear test for the core 20P. The system is left to relax for each millimeter of imposed displacement. Shear strengths values, before and after relaxation are readily seen.

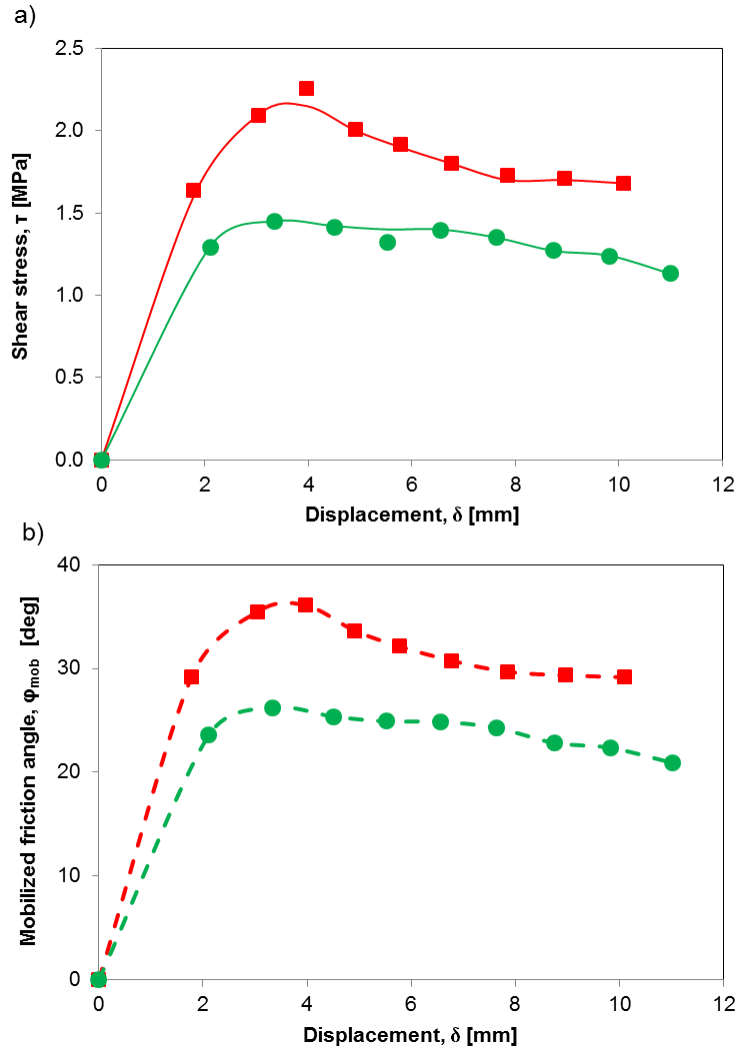


Figure 4.8. Shear test results for core 20P. (a) Shear stress vs. displacement. (b) Mobilized friction angle vs. displacement (assuming cohesion = 0).

4.4.1.2 P-waves

Figure 4.9-a shows the cascade of P-wave signatures for different values of vertical stress. The x-axis shows the travel time divided by specimen length to take into consideration sample shortening that results from the application of the load (i.e., the inverse of the velocity). Figure 4.9-b shows the P-wave velocities for the first load to 3 MPa, and a second reload to assess “healing effects”. The measured velocities range

from 1.68 to 1.82 km/s during first loading. Assuming a density $\rho = 2000 \text{ kg/m}^3$, the small strain constrained stiffness M_0 can be computed as (values in Table 1):

$$M_0 = V_p^2 \rho \quad (4.2)$$

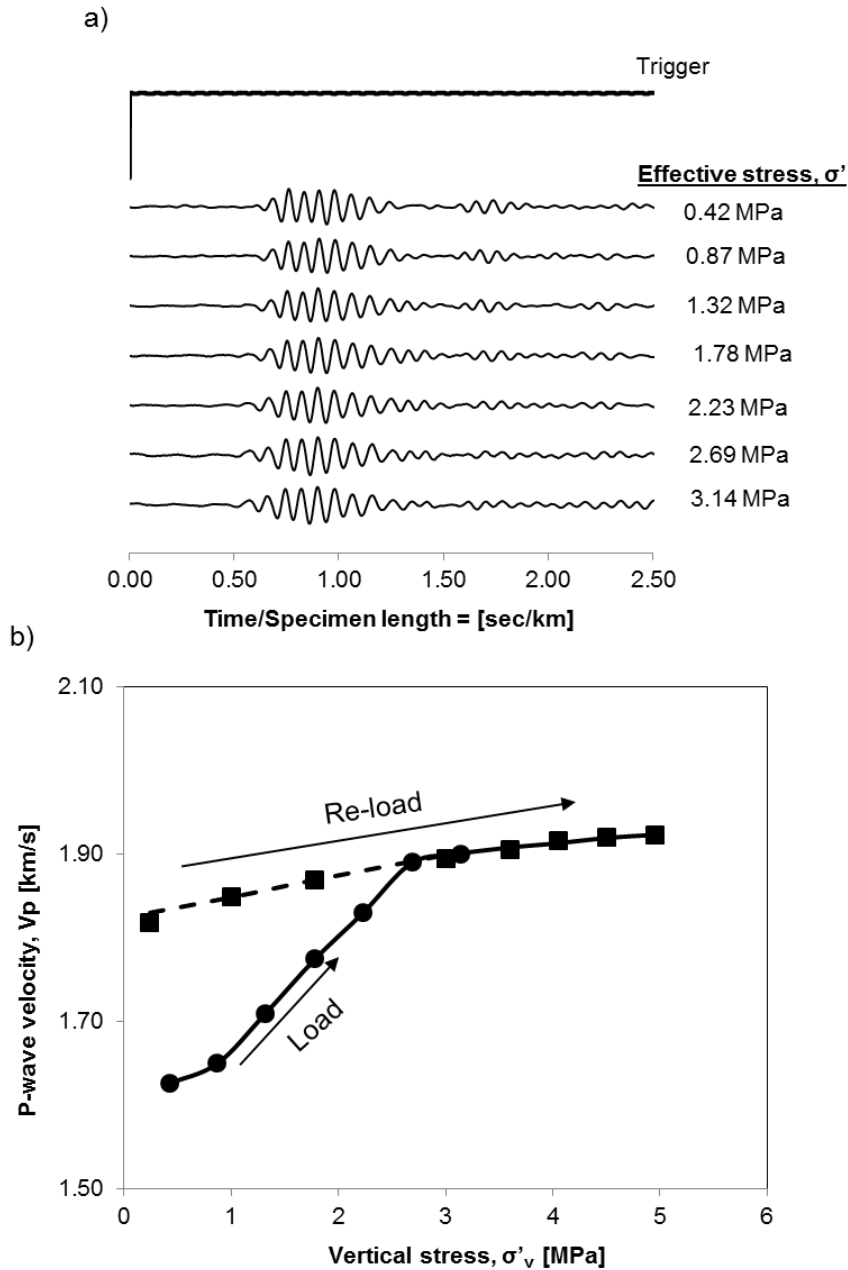


Figure 4.9. P-wave monitoring results for hydrate bearing sediments under different applied vertical effective stress σ'_z for the hydrate bearing sample 10P. (a) P-wave signature cascade and trigger signal during loading. (b) P-wave velocities.

4.4.1.3 Relaxation Test

Figure 4.10-a shows the relaxation behavior after the first load and the multiple re-load interventions. Vertical stress and displacement are measured during the relaxation test. The 1D consolidation equation ($C_v \nabla^2 u = \partial u / \partial t$) is solved together with the settlement equation ($\delta = \int C_\varepsilon \log(\sigma'_i + \Delta u) / \sigma'_i dz$), using a forward scheme in finite differences to simultaneously match the measured displacement. Figure 4.10-b shows results for the specimen 20P. Blue dots represent measured values and the black line is the result of the best fit. The insert shows the first loading in semi-log scale; the slope is the coefficient of volume compressibility m_v :

$$m_v = \frac{\Delta e}{1 + e_0} \frac{1}{\Delta \sigma'} = \frac{\varepsilon_{vol}}{\Delta \sigma'} \quad (4.3)$$

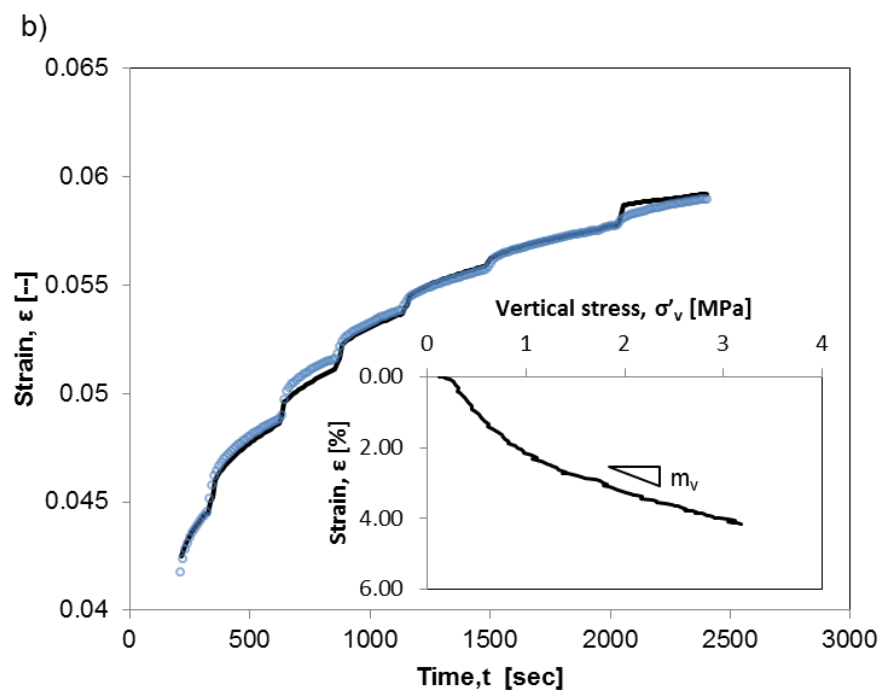
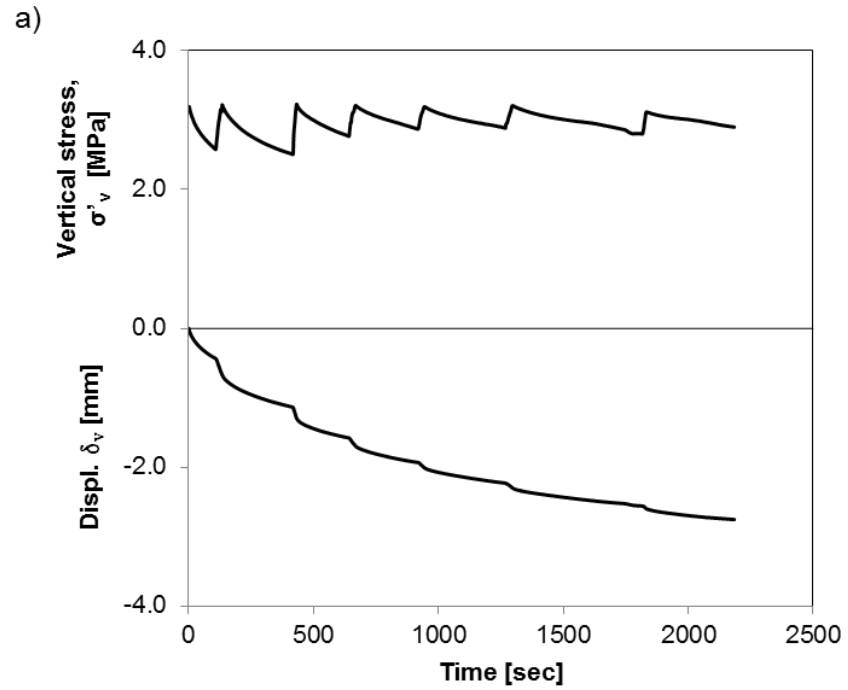


Figure 4.10. Relaxation test for the hydrate bearing sample 20P. (a) Measured stress and displacement. (b) Best match. The insert shows the first load response.

4.4.2 Methane Gas Dissociation

Cores 8P and 10P were dissociated under fluid pressure-control by opening a needle valve until the internal pressure equalizes with the room pressure. Core 20P was dissociated following a sequence of pressure- and flow-control conditions. Figure 4.11-a and Figure 4.11-b show the transition from pressure-control to flow-control.

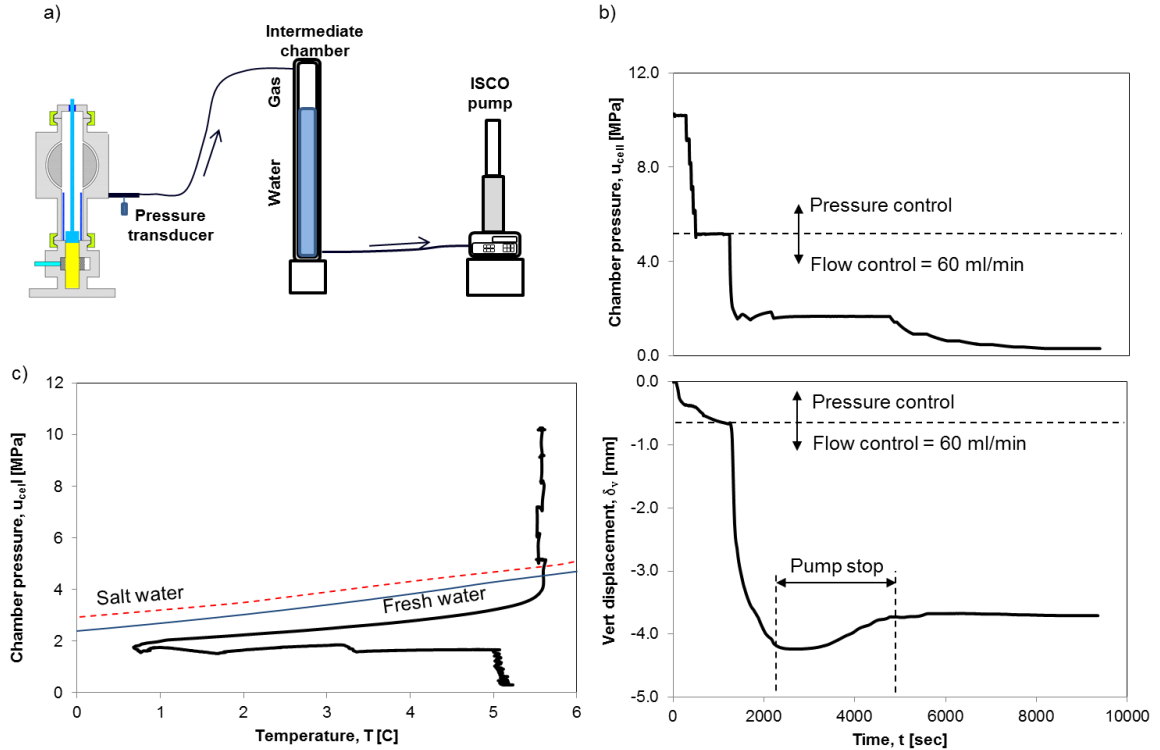


Figure 4.11. Dissociation test for core 20P under effective stress $\sigma'_v = 3$ MPa. (a) Flow control procedure. The ISCO pump extracts water at a constant rate of 60 ml/min, and the chamber pressure. Pressure and temperature are monitored at all times. (b) Pressure drop and volume contraction vs. time for the two systems: pressure control and flow control. (c) Dissociation test in PT space: hydrate stability boundaries in salt water and fresh water are shown for reference.

The dissociation of core 20P is plotted in Figure 4.11-c in a pressure-temperature PT space, where the phase boundaries for hydrate fresh and salt water are superimposed. Dissociation follows the theoretical curves closely. Minor deviations are potentially due to the lack of co-location between the dissociation front and the position of the

thermocouple (see Figure 4.1).

Hydrate saturation is computed from the amount of gas extracted as:

$$S_h = \frac{\frac{V_g}{n V_c} - \chi_{CH_4}}{c_o \beta} \quad (4.4)$$

where V_g is the volume of gas at atmospheric pressure, V_c the volume of the specimen, n the porosity, χ_{CH_4} is the methane solubility in water, c_o is the cage occupancy and $\beta = 172$ is the gas volume expansion factor.

The sediment volume contraction is also measured in all cores during this step. Figure 4.11-b shows the vertical displacement for core 20P during dissociation, reaching a vertical contraction of $\epsilon_v = 2.3 \times 10^{-2}$. After 36 min (2200 sec.) of testing, the pump needed to empty its container, pausing the test.

4.4.3 Post Dissociation Sediments Response

4.4.3.1 Shear Strength

Figures 4.12-a and 4.12-b show the shear strength and mobilized friction angle for core 20P after dissociation and under vertical effective stress $\sigma'_v = 3$ MPa. Once again, the specimen relaxes after each horizontal displacement (1mm – as in Figure 4.7), but the relaxation is less pronounced than in the case in the sediment with hydrates. The post dissociation shear response does not show a clear peak strength. Since this test was performed after dissociation and gas was present in the sample, the applied vertical stress is expected to be close to the effective stress.

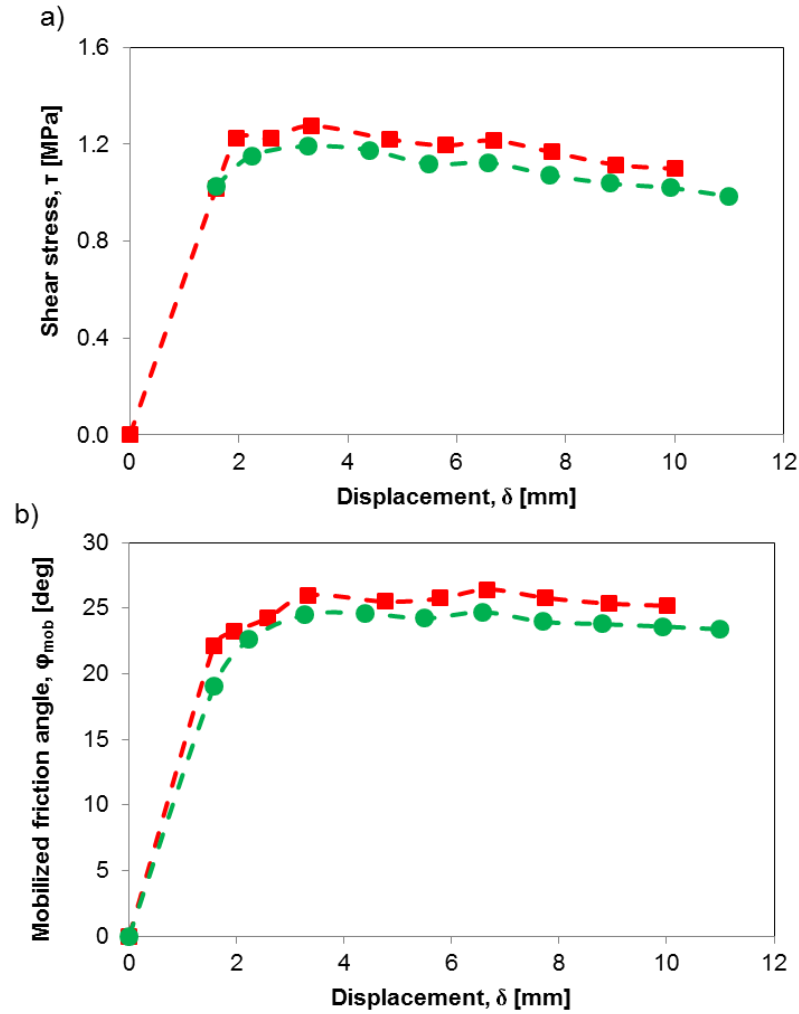


Figure 4.12. Shear test after dissociation for core 20P. (a) Shear test vs. displacement. (b) Mobilized friction angle vs. displacement (assuming cohesion = 0).

4.4.3.2 Compressibility

Compression test data gathered after dissociation are plotted in Figure 4.13 for core 20P. Since this specimen was loaded during dissociation, it shows a pre-consolidation value of 3 MPa. The virgin curve is reached during reloading.

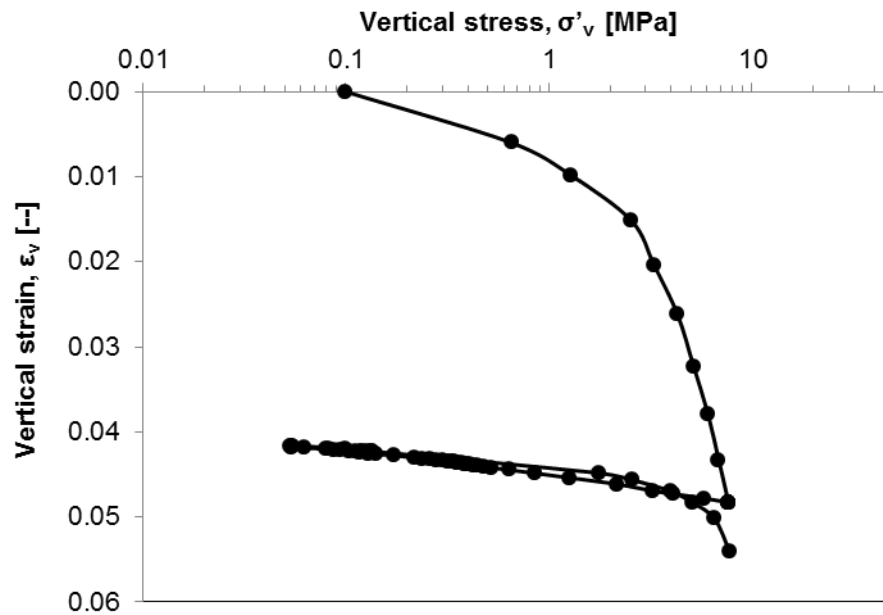


Figure 4.13. Compressibility test after dissociation for core 20P. Data show a pre-consolidation stress of 3 MPa since during dissociation it was loaded to that effective stress.

4.4.4 Summary

All values gathered by the DSC are summarized in Table 4.1. Figure 4.14 combines all shear tests for the core 20P, with and without hydrates.

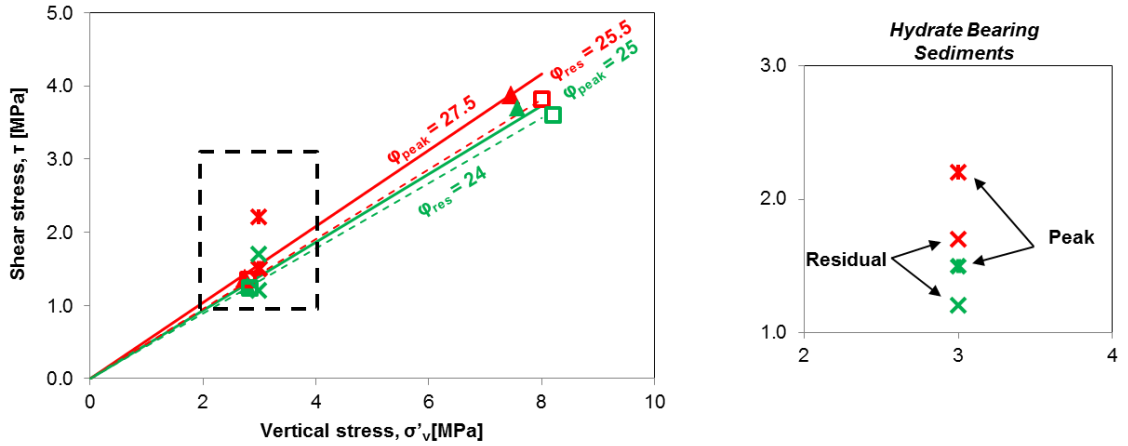


Figure 4.14. Compilation of shear tests with and without hydrates on marine sediments of Nankai Trough for the sample 20P. Triangles represent peak values while squares are residual values. Red dots corresponds to the pre-relaxation behavior and green dots are for post-relaxation. Insert: hydrate bearing sediments shear strength.

Table 4.1: Summary of results gathered using the direct shear chamber DSC

Properties		8P-6	10P-2	20P-4
Pre-dissociation	Coef. of volume compressibility, m_v [m ² /MN]	0.108	0.083	0.038
	Coef. of consolidation, c_v [m ² /s]	8.8×10^{-7}	4.4×10^{-6}	9.0×10^{-7}
	Peak shear strength, τ [MPa] @ $\sigma' = 3$ MPa			2.20
	Peak friction angle, ϕ_{peak} [°] (*)			36
	Residual friction angle, ϕ_{res} [°] (*)			27
	Wave velocity (@ $\sigma' = 3$ MPa), V_p [m/s]		1890	
	Initial height, H_0 [mm]	60.0	117	160
	M_{max} (@ $\sigma' = 3$ MPa), [GPa]		7.0	
Dissociation	Volume of extracted gas, V_g [cc]	2620	4330	5030
	Hydrate saturation, S_h [-]	0.21	0.15	0.27
	Settlement, δ [mm]	2.5	4.58	3.68
	Axial strain during dissociation, ε_v [-]	4.8×10^{-2}	4.5×10^{-2}	2.3×10^{-2}
Post-dissociation	Compression index, C_c [-]	0.39	0.13	0.14
	Recompression index, C_r [-]	0.018	0.001	0.011
	Peak shear strength, τ [MPa] @ $\sigma' = 3$ MPa			1.36
	Peak shear strength, τ [MPa] @ $\sigma' = 7.5$ MPa			3.69
	Peak friction angle, ϕ_{peak} [°] (*)			27
	Residual friction angle, ϕ_{res} [°] (*)			25

(*) Assuming cohesion = 0

4.5 Discussion: Comparison with Published Data

P-wave velocities and shear strength are compared in Figure 4.15-a. The P-wave velocity from logging while drilling data LWD are ~ 16% higher than V_p measured on pressure cores in the DSC. Sampling effects may account for this difference (refer to Stokoe and Santamarina 2000). Conversely, in-situ V_p measurements are affected by drilling operations, change in effective stress (cake formation imposes the mud weight as lateral effective stress), and longer wavelength averaging.

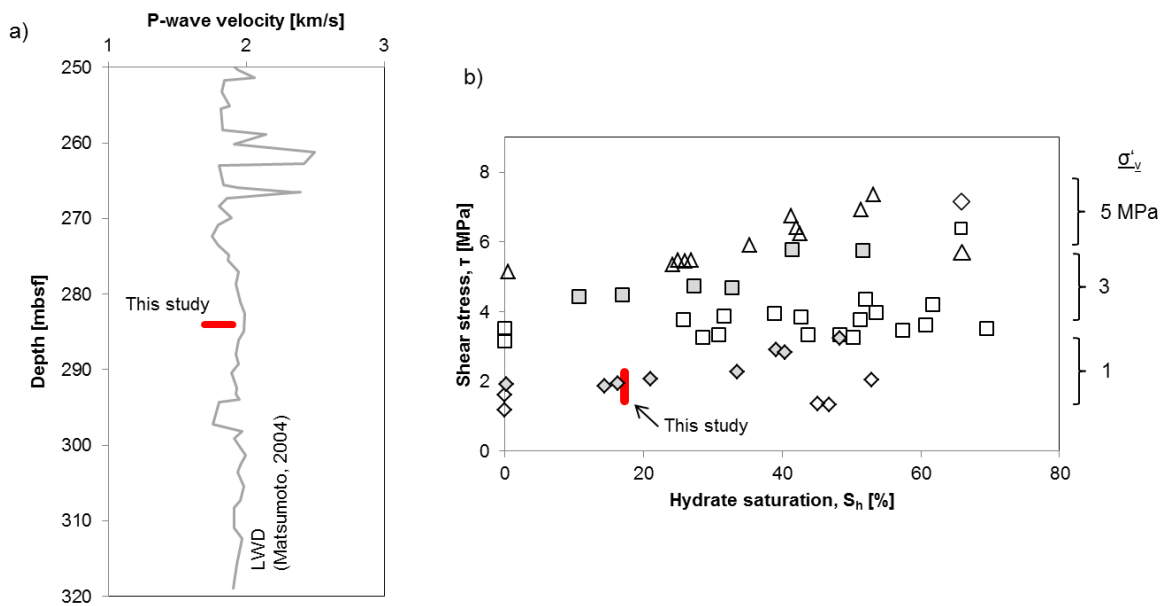


Figure 4.15. Comparison with published data. (a) P-wave velocity gathered from DSC is shown in a thick black line while the logging while drilling data is grey from Matsumoto et al. (2004). (b) Shear strength values from this study are shown in a thick black line. Diamonds represents 1 MPa in confining stress, while squares and triangles are the markers for 3 and 5 MPa. Empty markers are for the case of Nankai Trough bearing sand and methane hydrate; filled markers for Toyoura sand and methane hydrate. Shear strength from the literature was computed as half of the maximum deviatoric stress. Data compiled from (Hyodo et al. 2011; Miyazaki et al. 2011; Waite et al. 2009).

Figure 4.15-b compares the shear strength data gathered using pressure cores in the DSC and laboratory test published in the literature. In particular, triaxial tests were performed on remolded sandy specimens from Nankai Trough with methane hydrates at 1, 3 and 5 MPa of confining stress (Hyodo et al. 2011) and Toyoura sand with

reconstituted methane hydrates (Miyazaki et al. 2011). Published values tend to be higher than the ones gathered using pressure cores in this study. A significant contributor to this discrepancy is attributed to the biased hydrate formation in laboratory specimens.

4.6 Conclusions

This chapter described the design, construction and operation of a new shear device with concurrent wave measurements to characterize the small and large strain response of natural hydrate bearing sediments recovered using pressure core technology.

- The chamber was designed for a water pressure of 35 MPa and effective stress of 9 MPa (refer to Figure 4.3-c).
- This tool was first deployed to test pressure cores from the Nankai Trough. These hydrate bearing sediments, recovered during the July 2012 expedition were tested to determine P-wave velocity, shear strength, compressibility, relaxation, gas saturation and volume contraction upon dissociation.
- The peak friction angle of the hydrate-bearing clayey-sand specimen with $S_h = 0.27$ is 30% higher than the hydrate free sediment, yet, the residual friction angles are the same. The low residual friction angle $\varphi_{res} = 25^\circ$ confirms the effect of clay content.
- Shear strength results from laboratory experiments and P-wave measurements from Logging While Drilling data tend to be higher values than the one obtained with Direct Shear Chamber. The discrepancy may be due to the core disturbances during sampling and biased sample preparation practices used to reform hydrate.
- Sediments contract during depressurization-driven dissociation. Volume contraction is aggravated by fines migration and removal, i.e., fines production. Deliberate steps must be taken to prevent fines migration/removal in laboratory tests as well as field production studies. Filters with an opening size less than ~ 5 times the characteristic size of migratory particles should prevent loss of fines.

- The study of Nankai trough specimens reported in this Chapter documents the evolving methodology for the comprehensive characterizing of hydrate-bearing sediments. Data gathered with pressure core characterization tools play a central role. Additional information is gained from borehole logging measurements (in-situ tests – Chapter 5) and through post decompression sediment analyses, including index properties (refer to the discussion in Chapter 1). Finally, all data are considered within the framework of physical models and correlations that reflect worldwide sediment data. This methodology provides adequate estimates of parameters necessary for reservoir analyses and simulators.

CHAPTER 5

BOREHOLE TOOL FOR THE COMPREHENSIVE CHARACTERIZATION OF HYDRATE BEARING SEDIMENTS

5.1 Introduction

In-situ characterization plays a critical role in the determination of stratigraphy, soil characteristics and parameters in geotechnical engineering. Devices and tests procedures have evolved to overcome boundary effects, measurement errors and misleading interpretations. Still, data post processing remains a mixture of mechanical analyses and correlations.

Penetration testing gained broad acceptance in the 1940's when Karl Terzaghi standardized its procedure (Standard Penetration Test SPT) and included the split spoon sampler (Rogers 2006). Besides SPT, today's most common in-situ geotechnical tests include: Cone Penetration Test CPT, Flat Plate Dilatometer DMT, Pressuremeter PMT and Vane Shear VST. These devices have been extensively instrumented with diverse transducers such as temperature, geophones (seismic wave velocity), camera, radioisotope (gamma/neutron), electrical resistivity, dielectric, pH, oxygen exchange, and laser/ultraviolet induced fluorescence probe (Lunne, 2010; Robertson and Cabal, 2010).

This chapter reviews seafloor in-situ characterization devices and documents the development of a new tool for the in-situ characterization of off-shore formations in the context of hydrate bearing sediments.

5.2 Offshore Exploration – Current Technology

Offshore sediment characterization includes shallow seafloor assessment (~300 mbsf – meters below the seafloor) and deep formation explorations.

Shallow seafloor exploration and characterization have been driven by geohazard studies and the energy industry (gas and oil). Recent developments in deep water near-surface seafloor exploration reflect offshore foundation needs as well, from piled jacket structures to gravity-based platforms and anchored seabed structures (Lunne 2010). Figure 5.1 shows the evolution of deep-water exploration in the last 50 years.

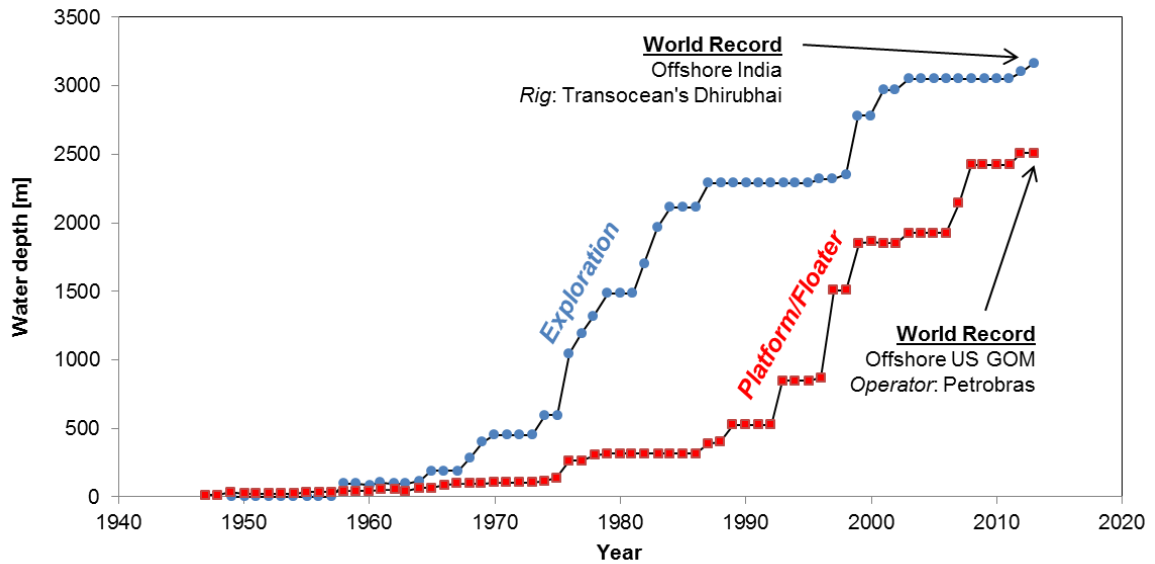


Figure 5.1. Worldwide progression of water depth capability for offshore exploration and production. Each point represents the depth of exploration and platform or floater (offshore-mag.com; Lunne, 2010).

Devices for seafloor characterization can be divided into 4 categories: Remotely Operated Vehicles ROVs, Dragged Devices, Wireline Logging and Penetrometers. These tools vary in maximum operational water depth and sediment penetration depth. Most devices require direct connection to a surface vessel for power supply and data acquisition. Salient examples follow.

5.2.1 Remotely Operated Vehicles ROVs

Remotely Operated Vehicles ROVs are unmanned underwater self-propelled vehicles. A crew operating from a floating vessel receives and sends data/commands through an umbilical cable, including video, power and data. ROVs were first deployed

as military vehicles in the 1950's. Table 5.1 lists commercially available ROVs often used for scientific purposes.

Table 5.1: Selected ROVs (Note: additional information in: www.marum.de)

Name	Size (length x wide x height) [m]	Main features	Max water depth [mbsl]
Cherokee	0.9 x 1.3 x 0.9	- 3 cameras - 3 pushcores (30cm) - 3 fluid samplers	1000
Quest	3.3 x 2.3 x 1.9	- Turbidity sensor - Up to 16 pushcores - KIPS fluid sampler - 2 sonars - HD video - Scoops, nets	4000
B-seal	0.74 (diam) x 5.5	- Detailing bathymetry data - Sonars - Purpose: detection of hydrothermal vent activities; pre-site surveys at cold seep system	5000
Move	2 x 2 x 3	- Sensors: salinity, temperature, turbidity, current measurements, bio-geo-chemical via incubation chambers - Operates in difficult conditions thanks to its tire traction system	6000
ParCa		- Captures pictures of a known volume of water for statistical analysis of suspended particles - Camera: NIKON Coolpix 995	6000
Nereus (*)	4.25 x 2.3 wide	- Hybrid (could be operated with or without umbilical cord) - Coring for sediments and rock - Biological sampling - Water sampling - HD Acoustic Bathymetry - HD video - Basic chemistry	10000

(*) Taken from Woods Hole Oceanographic Institution – Nereus was lost at sea on May 2014 – it was considered the second-deepest-diving device in operation

5.2.2 Draggled Devices

Dragged devices are attached with a cable to the main vessel, and are towed typically at a constant velocity while they collect data in the water column and the near-surface seafloor. For example the Neridis III (German Center for Marine Environmental Sciences – Marum) captures magnetic susceptibility (a proxy for fine-grained soils), conductivity, temperature, depth, turbidity, video, and photography (www.marum.de; Figure 5.2-a).

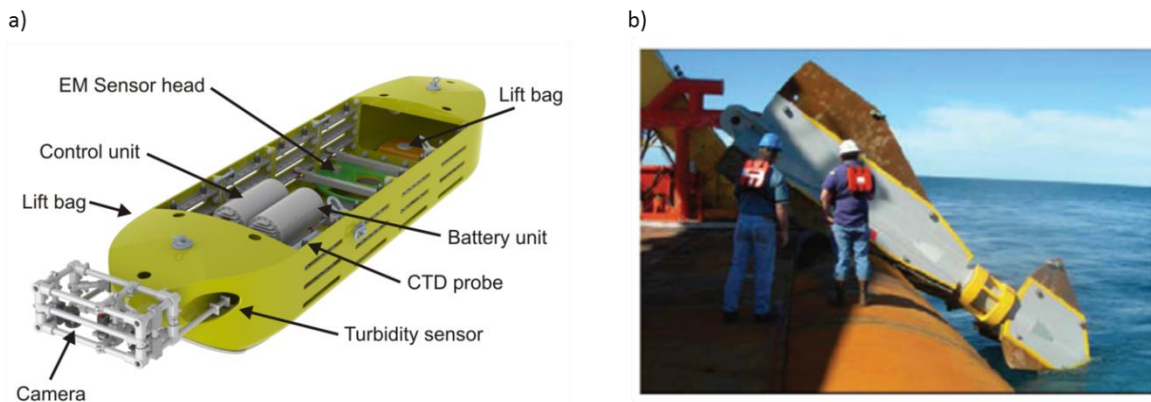


Figure 5.2. Draggled devices. (a) NERIDIS III (Marum). (b) OmniMax anchor (Shelton 2007; delmarus.com).

Dragged systems may also include anchors. The OmniMax anchor is a 10 to 17 m long torpedo-like anchor, has 2 or 4 flukes, and weighs 80 to 100 tonnes (Figure 5.2-b; Zimmerman et al, 2009; Shelton 2007). The anchor is left to free fall in the water column, and penetrates the sediment to a depth of 1.5 to 3 times the length of the anchor (Randolph, 2012; Randolph et al 2011). The recorded penetration force-time signature is back-analyzed to obtain the variation of seafloor strength with depth.

5.2.3 Wireline Logging and Borehole Operations

Wireline logging tools are lowered into a borehole while data is stored inside the tool or sent live to the vessel. Logging while drilling LWD and measurement while drilling MWD characterize the formation without the need to remove the drill string and

avoid relaxation effects. Available measurements are summarized in Table 5.2. Correlations and physics-inspired models are invoked to infer porosity, hydrate saturation, and formation stiffness from logging data (Collett and Lee 2011).

Table 5.2: Information collected during scientific cruises (iodp.ldeo.columbia.edu)

Principal Application		Resistivity	Acoustic Velocity	Density	Porosity	Gamma Ray	Geochemistry	Vertical Seismic Profile	Temperature/Pressure	Borehole/Drilling Parameters
<i>Technical</i>	Core-log Integration	√	√	√	√	√	√	√	√	√
	Log-seismic Integration		√	√				√		
	Drilling Operations								√	√
	High Temperature Environments			√		√			√	√
	Hole Stability Problems				√					√
<i>Scientific</i>	Hydrogeology	√			√				√	
	Paleoclimate, High Resolution	√	√	√	√	√				
	Stratigraphy/Sedimentology	√	√	√	√	√	√	√		√
	Structural Geology			√		√		√		
	<i>Gas Hydrates</i>	√	√	√	√		√	√	√	

Available sidewall tools are designed to recover specimens from cemented sediments using rotary motion or percussion, or to conduct fluid sampling (Figure 5.3). Schlumberger’s Modular Formation Dynamics Tester MDT is a modular design tool able to measure pressure, temperature, permeabilities (horizontal and vertical), obtain fluid samples (and a live fluid analyzer module) and run a pump-out test (slb.com). This device was used to test hydrate dissociation in Mallik (Canada; Anderson et al. 2008). Side wall samplers and testing systems operate within the annulus affected by drilling, and results are inherently biased.

Side-wall coring tool

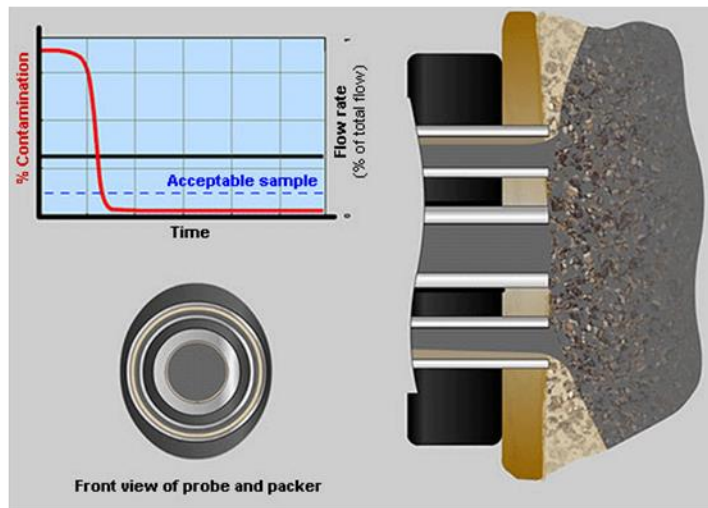


www.halliburton.com



www.slb.com

Side-wall fluid sampling



www.slb.com

Figure 5.3. Side wall samplers: coring and fluid sampling.

5.2.4 Penetrometers

There are full flow and standard cone penetrometers. Full flow penetrometers are preferred in soft sediments and include: ball, T-bar, and vane (Figure 5.4 – Table 5.3). The geometry of full flow penetrometers simplifies data and analysis interpretation. Cyclic penetration can be imposed to assess the fully remolded soil strength (Randolph, 2012; Randolph et al 2011; and Lunne et al, 2011).

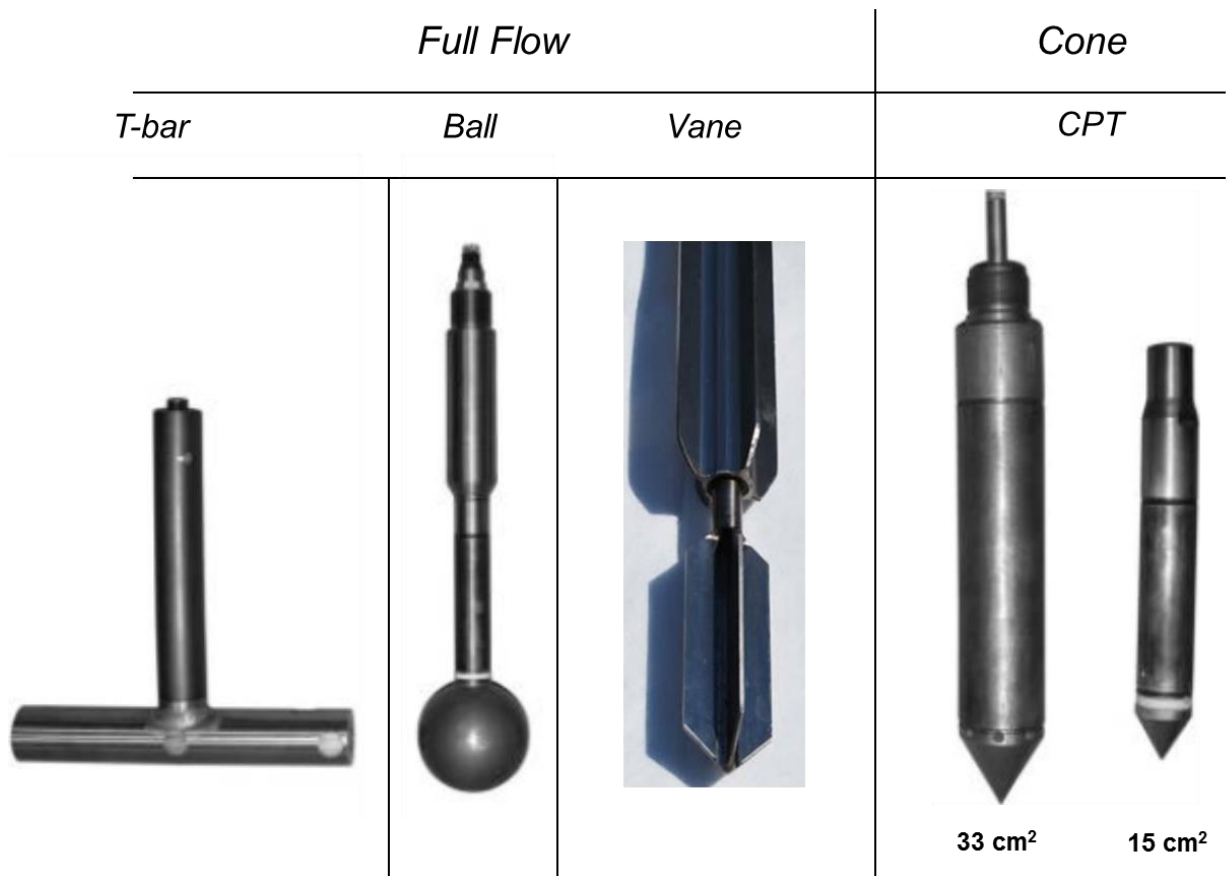


Figure 5.4. Penetrometers for soft marine sediment characterization (Kolk and Wegerif, 2005; fugro.com).

Table 5.3: Full flow penetrometers (Randolph 2012; Lunne et al. 2011)

Full flow penetrometer	Size (diameter x length) [mm]	Recommended guidelines	Standard
T-bar	40 x 250	-20mm/s penetration rate - 10 cycles of penetration and extraction with 15cm stroke	NORSOK G-001 (Norway 2004)
Ball	60 x 200 or 78 x 250	-20mm/s penetration rate - 10 cycles of penetration and extraction with 20cm stroke	(ISO expected to be published)
Vane	40 to 60mm diameter	- Rotation rate: 0.1 to 0.2 deg/sec - After peak: 10 rotations at 4rpm for remolded strength	NORSOK G-001 (Norway 2004) and ASTM D2573-08

On-shore and off-shore cone penetrometers have been instrumented to measure (Burns and Mayne 1998; Jefferies and Been 1987; Raschke and Hryciw 1997; Hryciw et al 1998): penetration resistance, sleeve friction, water pressure, temperature, inclinometers, electrical resistivity, nuclear density, S-wave detection, time domain reflectometry, lateral stress, redox potential, pH and visual grain size analysis. Table 5.4 summarizes available cone penetration tests for seafloor and borehole characterization.

Free-fall cones penetrate the upper few meters of the sediment column and measure penetration resistance, heat generation and dissipation, water pressure diffusion, and have accelerometers and inclinometers (e.g., FFCPT or FF-CPTU, www.marum.de; Steiner et al. 2012; Figure 5.5-a); data interpretation requires proper integration of depth-dependent insertion conditions. Penetrometers for deep marine characterization are deployed ahead of the borehole (bottom hole type). The penetration depth is limited by either mechanical/geometrical factors or by the reaction force that can be mobilized.

Table 5.4: Evolution in Cone Penetration Test CPT developed for marine sediment characterization (modified and updated from Boggess and Robertson, 2011; Lunne, 2010 and Peuchen, 2013)

Date	Equip. name	Company	Main features	Used for	Main reference
1970	WISON	Fugro	1.5m stroke Hydraulic cylinder	Bottom hole	Zuidberg (1972)
1972	--	NGI/McClelland	4 m penetration Discontinuous push	Near surface	Eide (1974)
1972	Seacalf	Fugro	25 m penetration (@ 130 m water depth) Discontinuous push	Near surface	Zuidberg (1975)
1973/ 1974	WISON APvanden Berg	APvandenBerg	Hydraulic cylinder	Bottom hole	Berg (1984)
1974	Stingray	McClelland	Push on drill pipe (Discontinuous push)	Near surface	McClelland (1975)
1974	Stingray	McClelland	Push on drill pipe	Bottom hole	McClelland (1975)
1976	Diving Bell	Delft Soil Mechanics Lab	60 m penetration (Discontinuous push) 600 kN reaction force	Near surface	Vermeiden (1977)
1982	Swordfish	McClelland	4.5m stroke	Bottom hole	Meyer et al. (1982)
1983	Mini Wison	Fugro	1 m stroke 5 cm ² cone Mounted on ROV	Near surface	Geise and Kolk (1983)
1983	ROSON	APvandenBerg D'Appolonia	Roller wheels (Continuous push)	Near surface	Berg (1984)
1984	Modified BORROS rig	McClelland	Continuous push	Near surface	Amundsen et al (1985)
1984	Wheeldrive Seacalf	Fugro	Continuous push	Near surface	Zuidberg et al. (1986)
1984	Dolphin	McClelland	Stroke 3m Capacity = 110kN Data stored on tool Pushed from mud pressure	Bottom hole	Peterson and Johnson (1985)
1991	SCOPE	Geo (Denmark)	Discontinuous push	Near surface	Denver and Riis (1992)
1992	Seascout	Fugro	Coiled rod 1 cm ² cone Pushed from mini-rigs	Near surface	Power and Geise (1994)

Date	Equip. name	Company	Main features	Used for	Main reference
1994	TSP	Rapp/Fugro/McClelland	70 m of 38 mm rod (coiled CPT) 3500 m max water depth	Near surface	Power and Geise (1994)
1994	WISON - XP	Fugro	Stroke 1.5 m to 3 m 10cm ² CPT Max depth = 3000 m 76mm sampler Data stored on tool Pushed from mud pressure	Bottom hole	Power and Geise (1994)
1997	Searobin	Fugro	Sampling of 1 m long CPT to 2 m (10cm ²)	Near surface	Hawkins and Narcus (1998)
2000	Penfeld	IFREMER	30 m penetration – 36 mm diameter rods Coiled rods 6000 m max water depth	Near surface	Meunier et al. (2000)
2001	PROD	Benthic (Australia)	Seabed founded CPT: 36 mm diam. rods Sampling: 44 mm diameter and 2.75 m long 2000 m max water depth	Near surface	Pennington and Kelleher (2007)
2001	CPTWD	SPG and ENVI	Stroke >3m Data stored on tool Advanced by drilling	Bottom hole	Sachetto et al. (2004)
2005	T2P	UT Austin	Mini cone – 6.4 mm diameter; 1.3 m long	Bottom hole	Chartier 2005; Flemings et al. 2006; Darnell et al. 2012
2007	MeBo	Marum	Sampling: 74-84 mm diameter and 3m long (pushing or rotary coring) Up to 50 m of soil sampling	Near surface	Freudenthal and Wefer (2007)
2007	WISON - EP	Fugro	Data stored on tool and real time Pushed from mud pressure	Bottom hole	Peuchen and Raap (2007)
2009	geoROV	GeoMarine	5cm ² cone ROV mounted	Near surface	GeoMarine (2010)
2010	DeepCPT (Figure 4-b)	Gregg	200kN thrust capacity (Continuous push) 3000 m max water depth and 200kN capacity 10 and 15cm ² cones	Near surface	Boggess and Robertson (2010)

Penetrometers can also be used to recover fluids: BAT (max operation depth 800 mbsl; Torstensson, 1984), DGP (max operation depth 2000 mbsl; NGI; Kolk and Wegerif, 2005) and PWS (Fugro’s pore water sampler; fugro.com) which can easily be installed in Fugro’s Dolphin or WISON XP. Other samplers include: Hydropunch (Robertson et al. 1996), Envirocone (O’Neill et al. 1996) and Cone Sipper (Lightner and Purdy 1995). Hydraulic conductivity has been correlated to the measured tip resistance, sleeve friction and pore water pressure (Elsworth and Lee 2005).

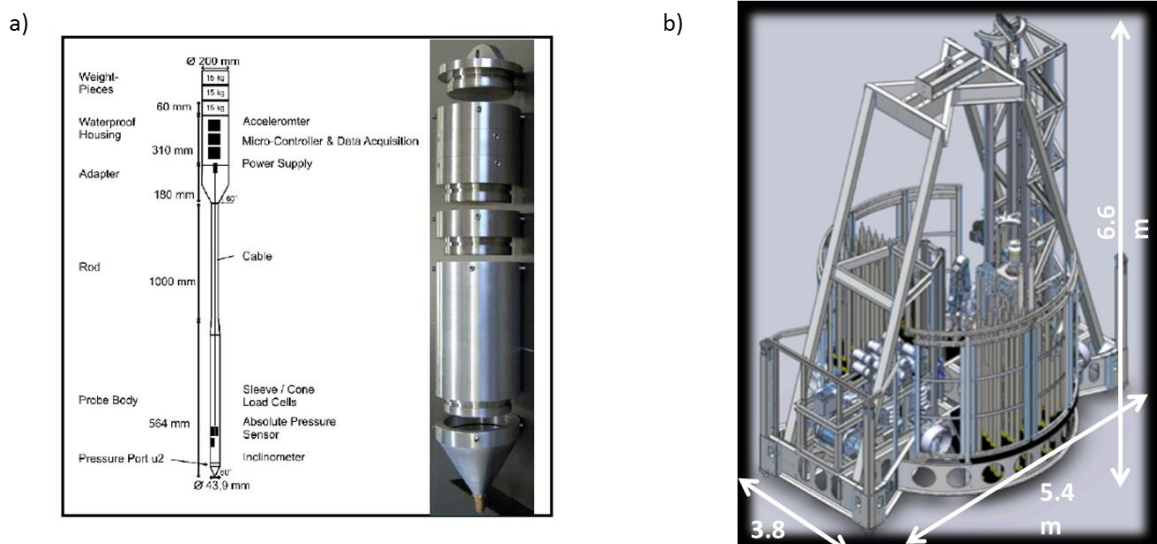


Figure 5.5. Cone penetrometers for shallow seabed characterization. (a) Free fall cone (marum.de). (b) Minirig (greggseafloordrill.com).

Penetrometers cause high shear strains at high strain rates (Mayne 2001; Chung et al 2006); the computed strength of full flow tests is significantly higher than values measured at small strain rates (Lunne et al 2011): typically, the measured undrained shear strength increases by 3% to 10% per log cycle of strain rate (Diaz-Rodriguez et al. 2009).

5.3 Design of an In-situ Tool for Hydrate Bearing Sediment Characterization

Critical parameters needed for the analysis of reservoirs and the design of gas production strategies from hydrate bearing sediments are identified in Table 5.5. The in-

situ tool described herein was designed to address some of these needs.

Table 5.5: Critical parameters needed for analyses and engineering in relation to hydrate bearing sediments.

	Property	Sensor/method
Index Properties and Reservoir Characteristics	In-situ temperature - pressure	Direct measurement
	Porosity – Hydrate saturation	NM
	Hydrate morphology	Video
	Grain size distribution – Fines content	From soil sampling / video
	Stratigraphy	
	Formation history	
	Salinity	From pore water sampling
Pore water geo-chemistry		
Thermal Properties	Thermal conductivity	Direct measurement and post-process.
	Specific heat - Latent heat	NM
Hydraulic Properties	Capillarity – Saturation curve	NM
	Relative permeabilities	NM
	Hydraulic conductivity	Direct measurement and post-process.
	Potential migration pathways	NM
Mechanical Properties	Lateral stress coefficient	NM
	Soil Stiffness: shear and bulk stiffness	Direct measurement and post-process.
	Strength	Direct measurement
	Stress-dependent dilatancy	From soil sampling and lab testing
	Compressibility upon dissociation	

NM = Not measured by this device

The disturbed/plastified zone around a cavity or inserted rod extend to a distance $R_{\text{dist}} = 4.5 R_{\text{rod}}$, where R_{rod} is the rod diameter (Baligh 1985; Kirsch 1898; also Kirsch solution and St. Venant principle). The zone affected ahead of a penetrating rod extends to $L_{\text{dist}}/R_{\text{rod}} = 3$ (Baligh 1985). Therefore the new tool is designed to obtain physical parameters away from the zone affected by coring, in particular, beyond 3 times the radius of the borehole.

General Characteristics: The tool is designed as a stackable-type modular penetration system with a simple but versatile architecture. Measurements are made ahead of the

borehole during and after penetration. The tool is made of stainless steel 316 for high stress- and chemical-resistance. All modules are 36.5 mm in diameter (area ~ 10 cm²). The device consists of: the body, the modular probe system, and electronics (Figure 5.6).

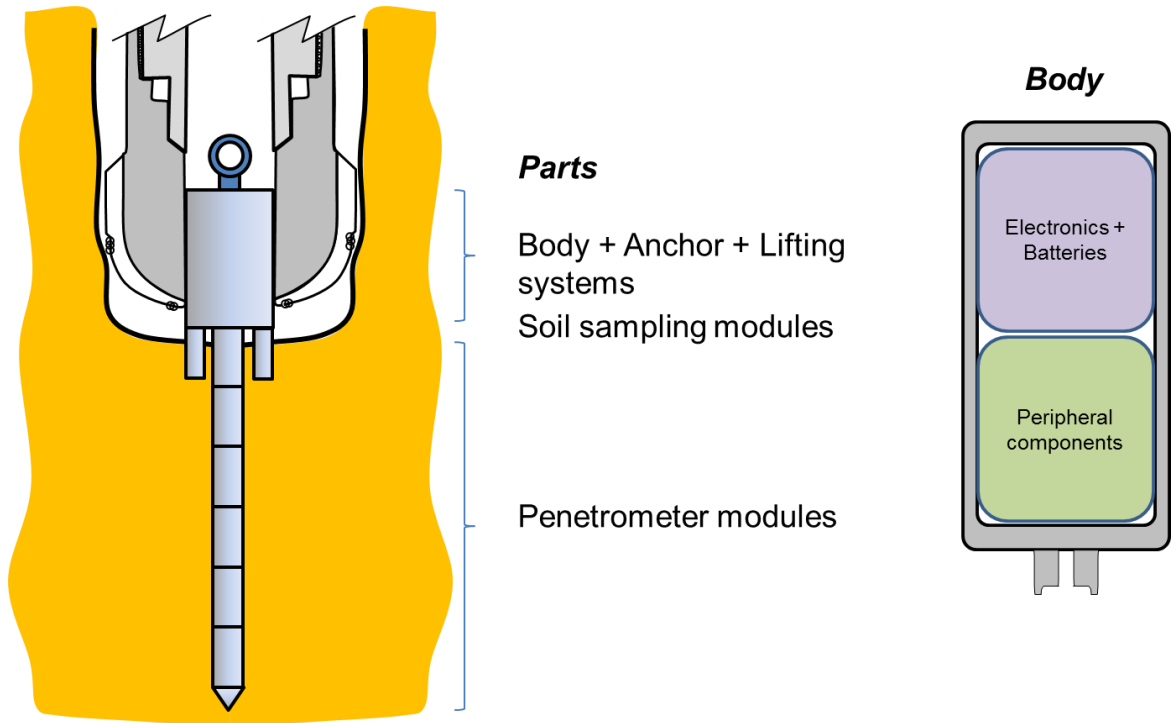
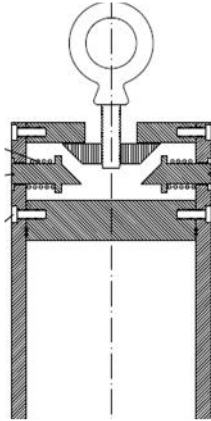


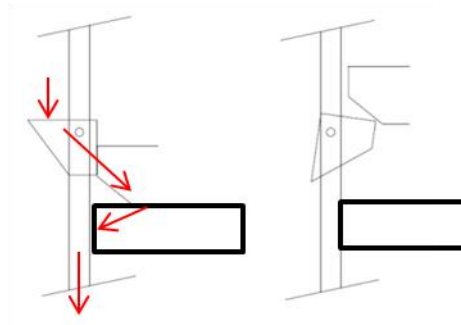
Figure 5.6. In-situ characterization tool: General view.

Body: The body is a cylindrical cavity (OD = 100 mm; SS316) with two rigid end caps. The body supports the modular penetrometer and sampling tubes, houses the electronics, includes the fishing/lifting system, and the anchor to the drill bit Bottom Hole Assembly BHA (Figure 5.7). The anchor system couples the tool to the drilling string to use the weight of the drill bit to advance the penetration device. The geometry of the body depends on the drill string available at the site.

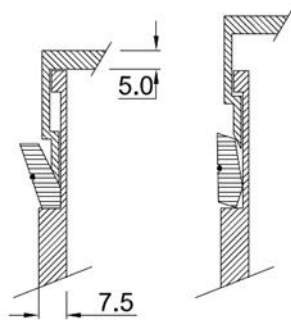
Lateral pins



Lateral pivoting wedge



Lateral latches



Standard API connector

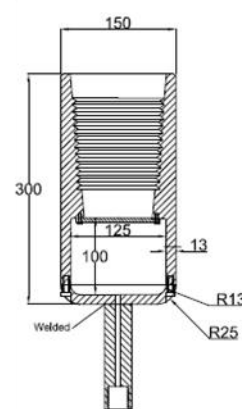


Figure 5.7. Coupling system used to lock the tool to the drill bit.

Modular Probe: The maximum penetration force is computed for a hydrate bearing sediment with an undrained shear strength $S_u = 10$ MPa (hydrate saturation $S_{hyd} = 100\%$; Waite et al., 2009). The maximum force needed to penetrate a 10 cm^2 probe into this formation is ~ 90 kN. The maximum tool length to avoid buckling is computed from Euler's equation. Results show that the maximum length is $L_{max} = 1.20$ m for the case of both ends hinged (Figure 5.8).

The load cell at the tip of the modular probe has a capacity of 200 MPa and measures a combination of water pressure and penetration resistance (Figure 5.8). The

tool can be internally pressurized prior to deployment to pre-stress the load cell to extend the depth range of the probe.

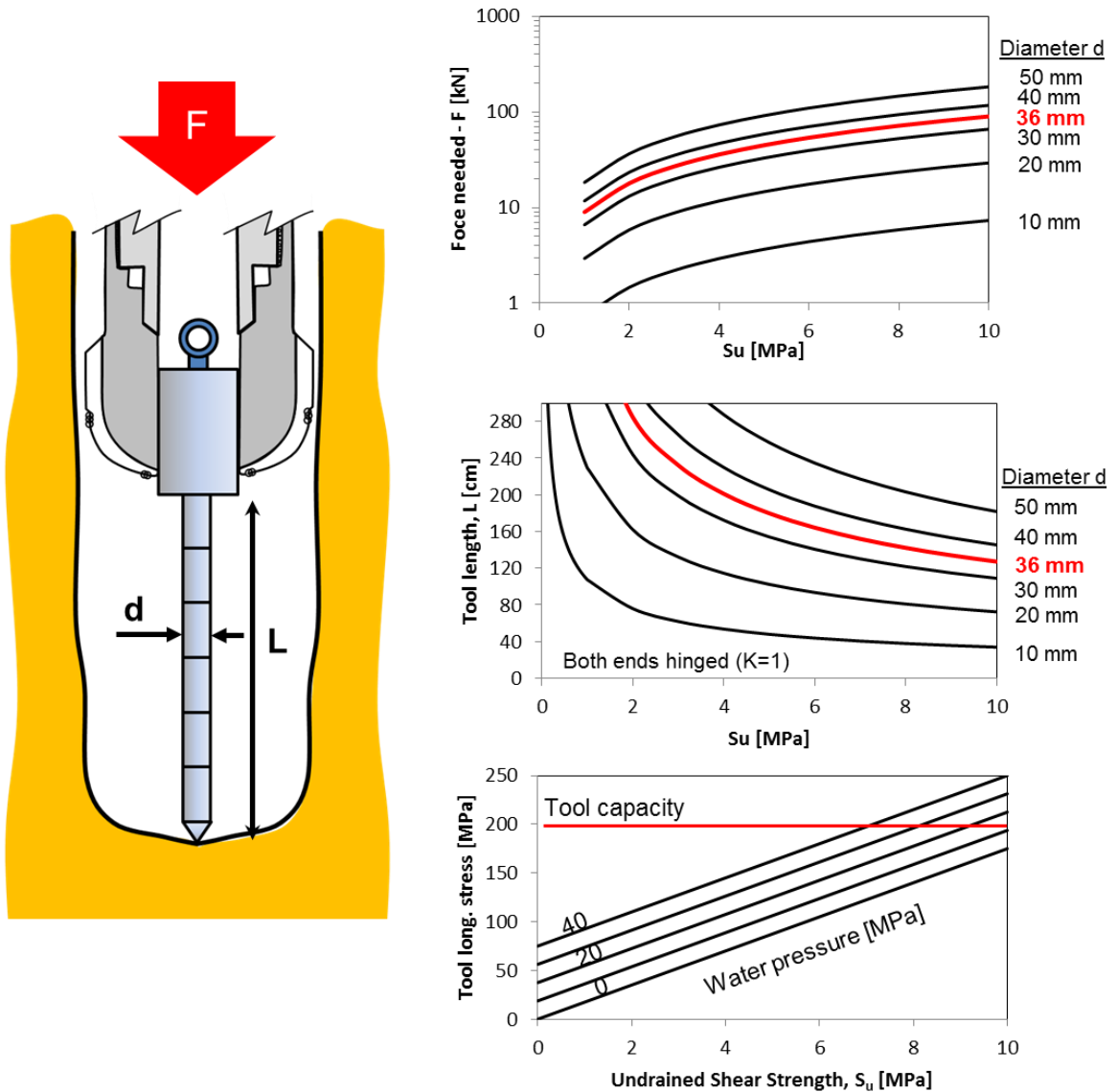
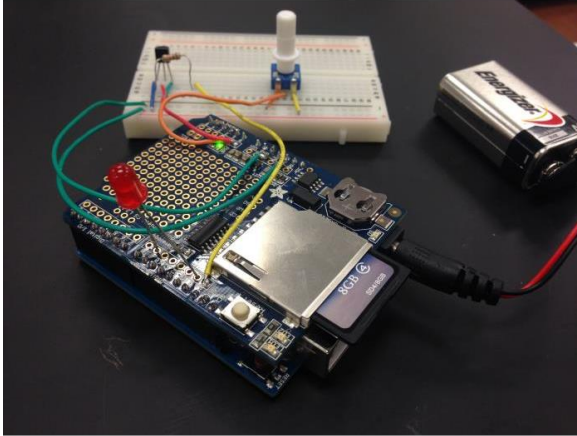


Figure 5.8. Overall mechanical design. (a) Maximum needed force. (b) Maximum tool length to satisfy buckling restrictions. (c) Tool longitudinal stress dependence between water pressure and undrained shear strength.

Electronics: Data is either transmitted to the surface vessel in real time, or stored in the tool. Transmission requires a communication cartridge and a communication modem (weatherford.com). Data storage within the tool is possible using off-the-shelf

microprocessors powered by standard batteries. This is the approach selected for this prototype. The chosen microprocessor is an Arduino UNO (www.arduino.cc) due to its intuitive architecture for sensor development, low power consumption, small dimensions and large online library of projects and peripherals. Figure 5.9 shows the device ready to store data in a SD card, and its technical specifications.



<i>CPU</i>	16 MHz ATmega328
<i>Pins In/Out</i>	14 I/O
<i>Sampling frequency</i>	1 ms
<i>Memory flash</i>	32 K
<i>Size</i>	2.7in x 2.1in
<i>Software</i>	Arduino IDE (Java based)
<i>Power</i>	Batteries / USB / AC-to-DC adapter
<i>Pc connection</i>	USB port
<i>Voltage (limits)</i>	6-20 V
<i>Voltage (recomm.)</i>	7-12 V
<i>Operation voltage</i>	5V
<i>Resolution</i>	10 bits
<i>Memory storage</i>	Peripheral / SD card
<i>Price</i>	~\$30

Figure 5.9. Data storage unit: Arduino UNO (arduino.cc).

The analog-to-digital converter ADC available on the microprocessor's on board is a 10 bits unit (expandable to 16 bits). This allows a resolution of 0.01° C for thermocouples and 0.01 mV for load cells and strain gauges (Figure 5.10-a, -b and -c). Measured power consumption is plotted in Figure 5.10-d for the Arduino, Secure Digital SD card writer, thermocouples, load cells, strain gauges and impedance analyzer (electrical resistivity measurements). Most of the power is consumed by the microprocessor and the data storage components. The maximum amount of time a single 9V battery can last varies from 1 to 3 hrs.

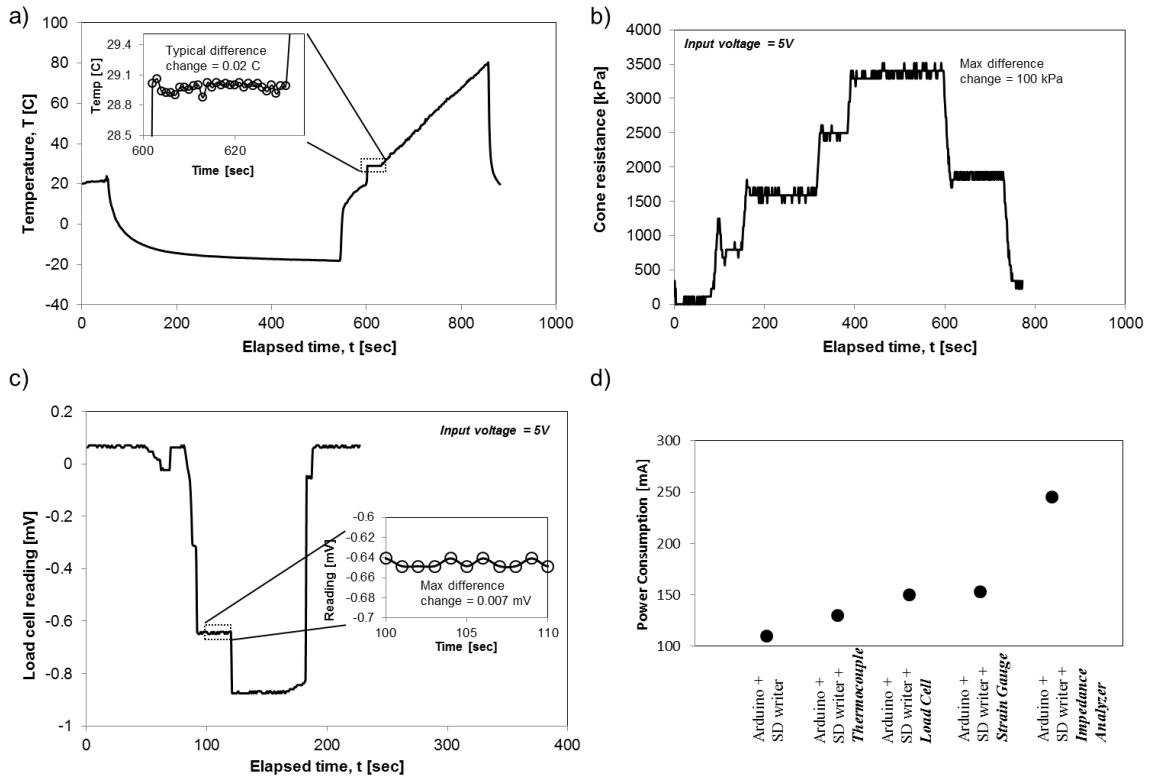


Figure 5.10. Data storage unit: Resolution (a) Thermocouples. (b) Strain gauge. (c) Standard load cell. (d) Power consumption.

5.3.1 Tip Module: Insertion Forces and Temperature

5.3.1.1 Design:

The tip module consists of the tip itself, the sleeve and the porous filter (Figure 5.11). The sleeve houses and protects the instrumentation. The nucleus is instrumented with a full bridge strain gage (to cancel bending and temperature effects) and 2 thermocouples. The porous filter ring is made of stainless steel 316.

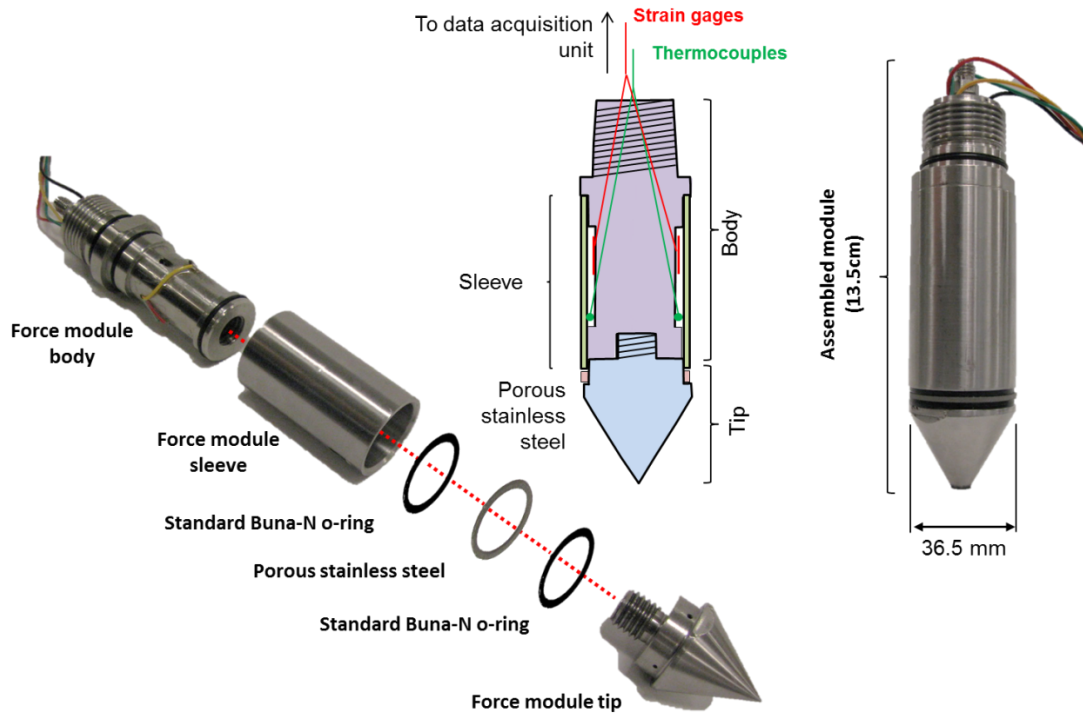


Figure 5.11. Tip module: parts, elements and wiring.

5.3.1.2 Mechanical Verification:

The tip module is designed to sustain the expected penetration forces and water pressure. Analytical solutions and a FEM numerical model are used to assess internal stress concentrations, the collapsibility of the sleeve and buckling of the tool. Figure 5.12 shows the stress field for the tip module facing 90 kN penetration force and 10 MPa water pressure. Results show adequate mechanical performance under these extreme conditions.

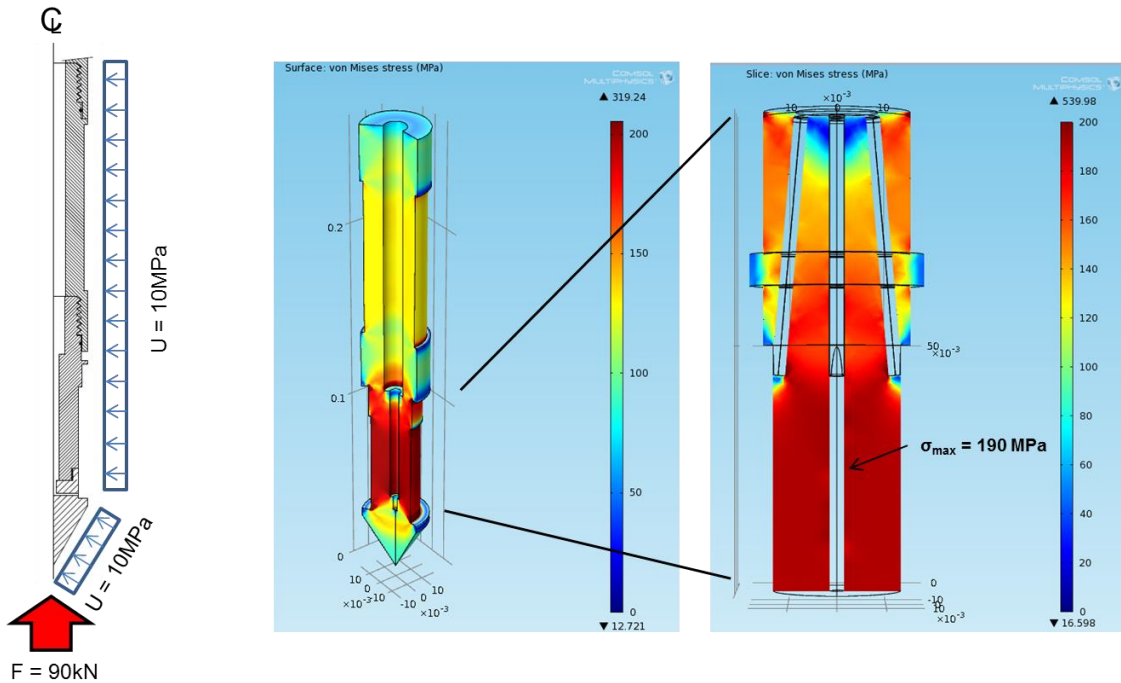
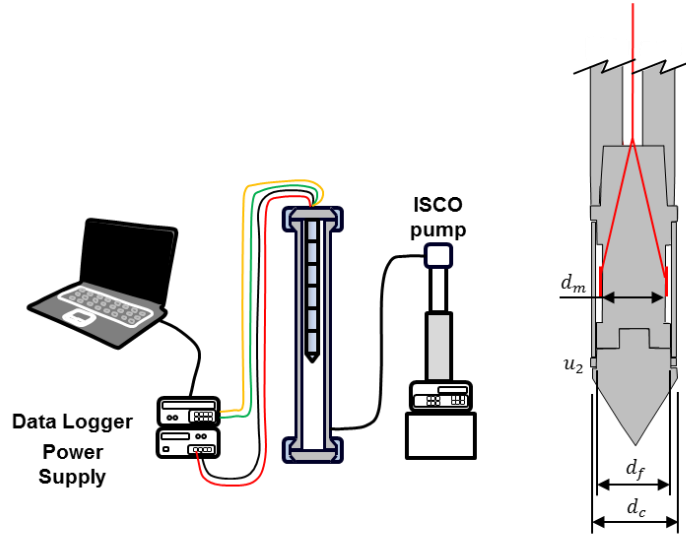


Figure 5.12. Tip module mechanical verification: Yield stress for SS316 is 200MPa.

5.3.1.3 Calibration:

A chamber and coupler are designed to calibrate the tool. It consists of a 1.20 m long SS316 tube with a cap able to couple with the tool to the pressure chamber (Figure 5.13). All cables exit from the top; the tool response is logged using a standard computer-based data logger. The tip was successfully tested to 25 MPa of water pressure. The tool pore pressure response (generally called U_2) and insertion forces q_t correlate well with the applied fluid pressure in the chamber (2% error). The tip resistance determined with the strain gages fixed to the core is corrected for tip-to-core area ratio (coefficient a_s), and the pore pressure effect on the shoulder $(1-a_n) u_2$. Figure 5.13 shows the equations used and calibrations.



$$V_r = \left(\frac{V_{out}}{V_{in}} \right)_{(strained)} - \left(\frac{V_{out}}{V_{in}} \right)_{(unstrained)}$$

$$\varepsilon = \frac{-2V_r}{GF [(v + 1) - V_r(v - 1)]} \quad \text{Strain gage factor (GF) = 2.15} \quad \text{(CEA-06-062UT-350)}$$

$$q_c = \varepsilon E a_s \quad E = 200 \text{ GPa (Stainless Steel)}$$

$$q_t = q_c + (1 - a_n) u_2 \quad a_s = \frac{d_m^2}{d_c^2} \quad a_n = \frac{d_f^2}{d_c^2}$$

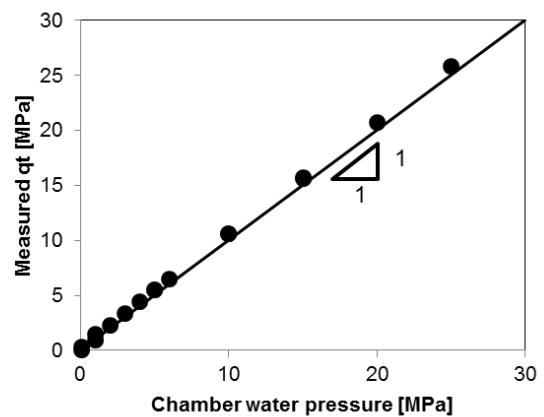
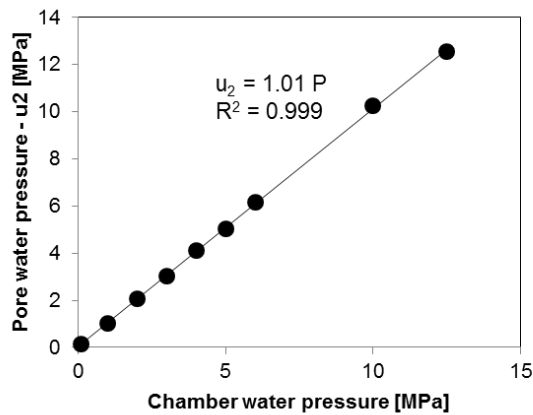


Figure 5.13. Tip module calibration. Measured pressure using strain gauges vs. chamber water pressure.

The thermocouples in the force module are located inside the protecting sleeve. The tool thermal response was measured by subjecting it to cooling and heating cycles in an environmental chamber. The response delay is 10 sec during cooling, and 8 sec

during heating (Figure 5.14-a).

Thermal effects are partially compensated: they cancel in the full bridge but strains in the core remain. A 30 degrees Celsius change in temperature produces a 0.12mV bridge response for a 10V bridge excitation (Figure 5.14-b).

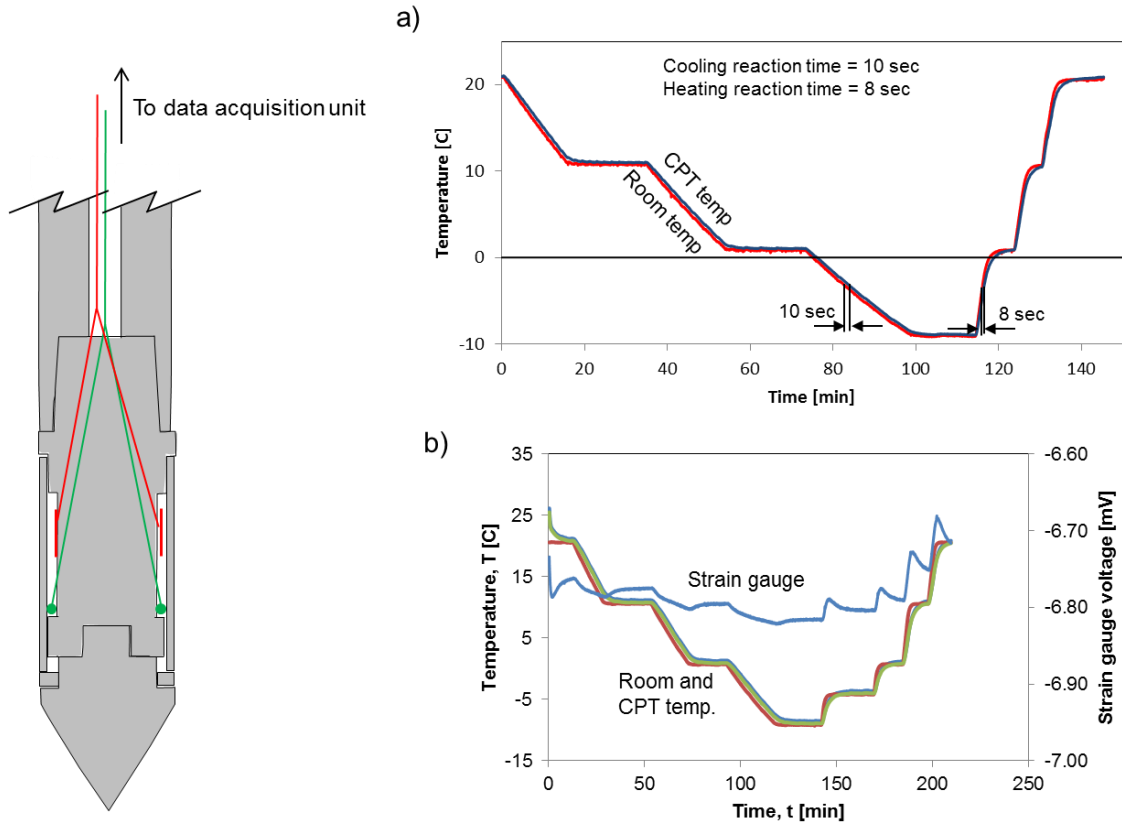


Figure 5.14. Tip module: temperature effect. (a) Thermocouples response time. (b) Strain gage response to temperature change.

5.3.2 Hydraulic Conductivity, Fluid Sampler and Mini Production Test

5.3.2.1 Design:

Hydraulic conductivity is measured using a system of valves and pressure transducers to determine flow rate and pressure gradient (Figure 5.15-a). The water extraction inlet at the tip of the force module is connected to the storage tank through a solenoid valve and a check valve (to prevent reversed flow after sampling). The pressure

transducer in the tank measures the pressure evolution in the gas in order to compute flow rate using Boyle's law.

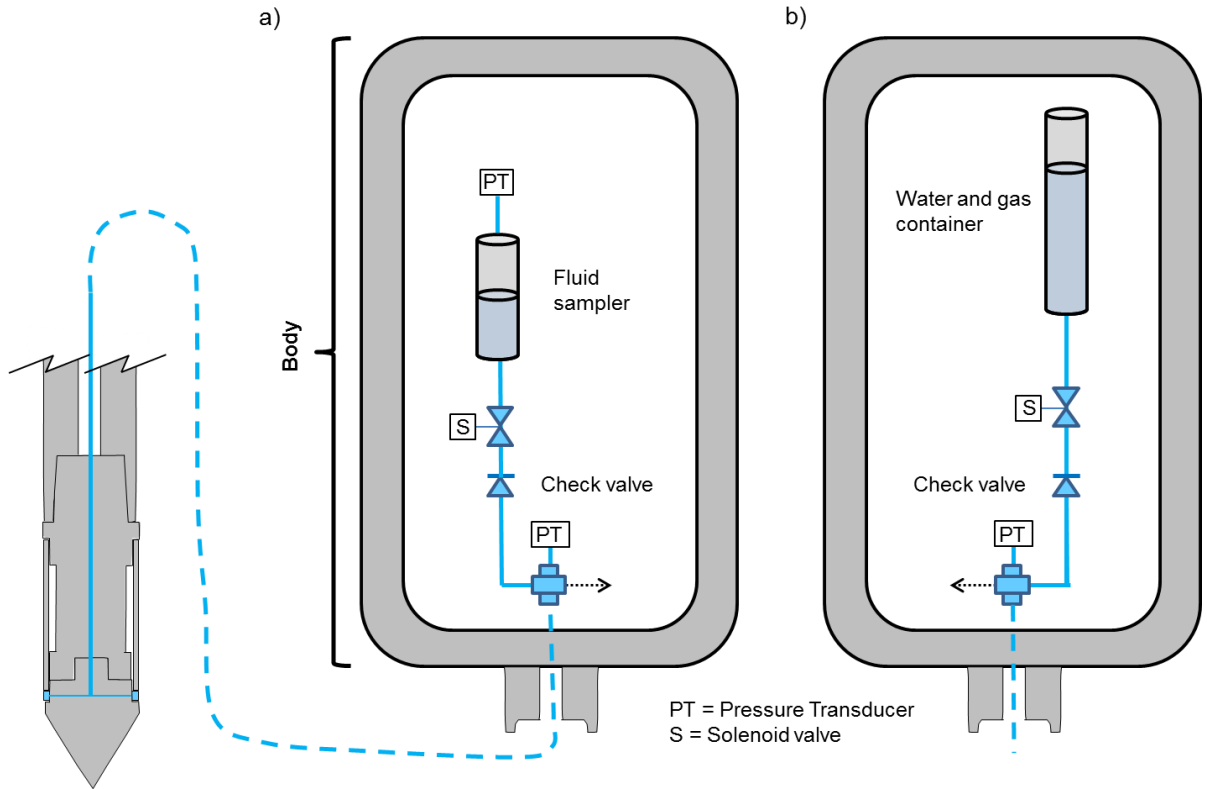


Figure 5.15. Hydraulic dual-system components: (a) Hydraulic conductivity measurement system. (b) Mini-production test

The governing equation:

$$q = F k (u_o - p_o) \quad (5.1)$$

shows the flow rate q as a function of the hydraulic conductivity k , the initial reservoir pressure u_o , the initial pressure in the container p_o and a shape factor F which accounts for boundary conditions. Pore water can be sampled without dissociation by pre-pressurizing the container to an initial pressure u_o higher than the dissociation pressure. Water permeability k can be estimated as (Figure 5.16-a; Tortenson 1984):

$$k = \frac{p_o v_o}{F t} \left\{ \frac{1}{p_o u_o} - \frac{1}{p_t u_o} + \frac{1}{u_o^2} \left[\ln \left(\frac{p_o - u_o}{p_o} \frac{p_t}{p_t - u_o} \right) \right] \right\} \quad (5.2)$$

where v_o the initial volume of gas in the container, and p_t is the pressure in the container

at time t .

The test duration is highly dependent on the permeability. A passive test can be implemented with this probe as well by measuring the dissipation of the excess of pore pressure generated during penetration (see Burns and Mayne 1998; Burns and Mayne 2002; Chartier 2005).

Finally, a parallel hydraulic system allows for a mini-production test. A solenoid valve opens a tank kept at a pressure p_0 below the dissociation pressure, thus water and gas can be extracted and sampled (Figure 5.15-b).

5.3.2.2 Verification:

The shape factor F for this probe is determined using numerical simulations; the computed value is $F = 2D$ (Figure 5.16-b), and corresponds well with published analyses (Hvorlsev 1951; Chirlin 1989; Mathias and Butler, 2006). Note that given the location of the water inlet, flow conditions resembles spherical flow. The numerical and analytical solutions for a spherical flow are compared in Figure 5.17. The chart shown in Figure 5.17-c facilitates the estimation of the hydraulic conductivity using this probe from the measured flow rates and differential pressure changes.

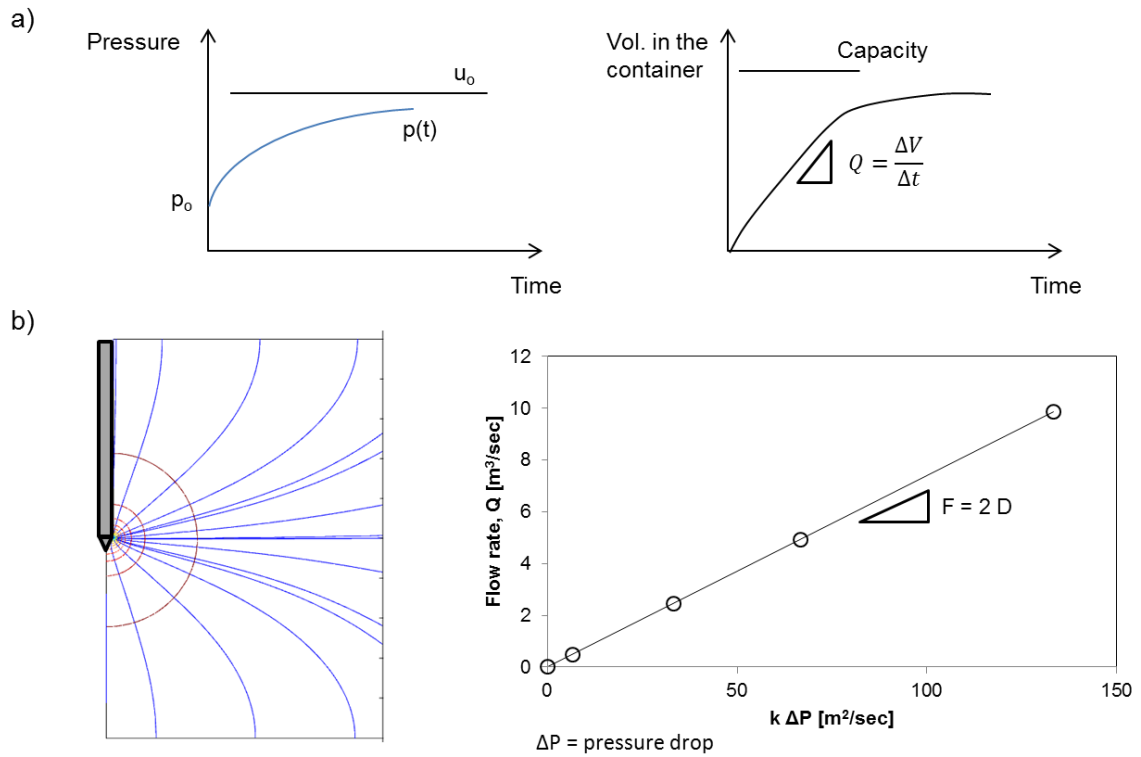


Figure 5.16. Hydraulic conductivity measurement system. (a) Pressure and volume vs. time. (b) Shape factor from numerical simulations. Note: u_o is the reservoir water pressure and p_o the initial water pressure in the container.

Reynold's number ($Re = Vd/v$) should be $Re < 10$ everywhere in the soil mass to satisfy laminar flow, i.e. Darcy's condition (Miyazaki 2005; discussion in Muskat 1965). The associated maximum pressure drop can be obtained from Figure 5.17-c.

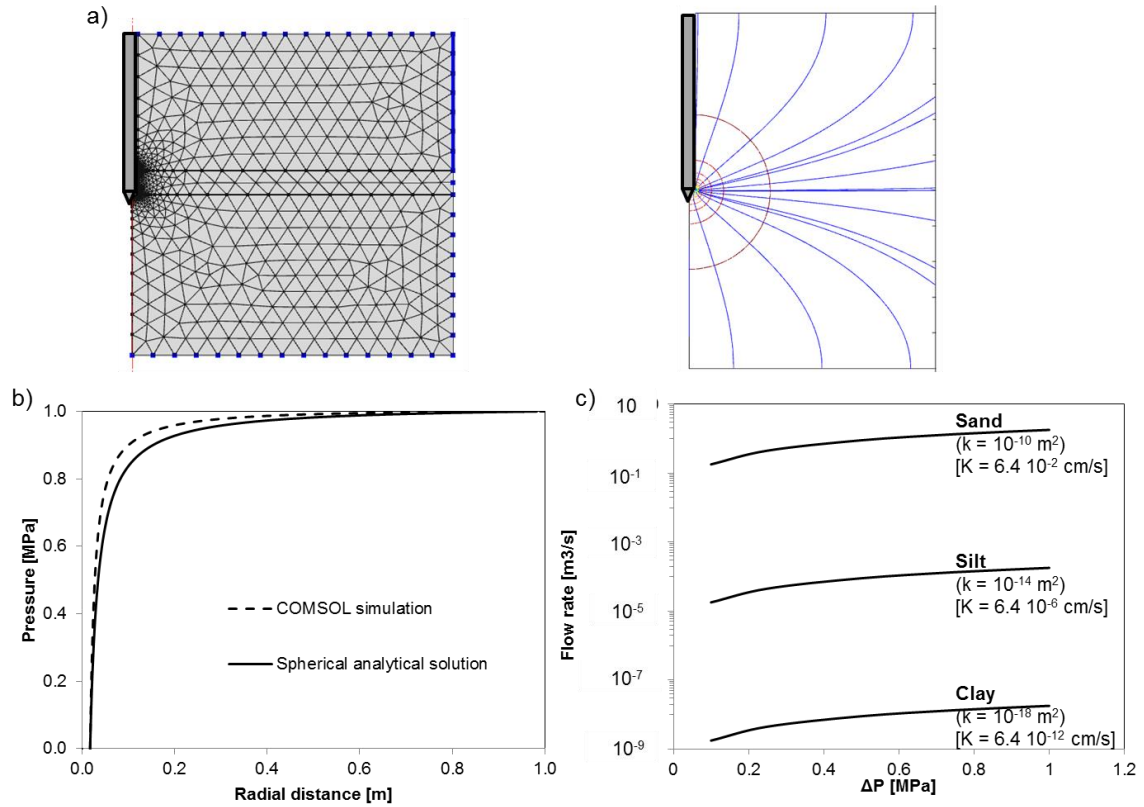


Figure 5.17. Hydraulic conductivity system verification. (a) Numerical model in COMSOL. (b) Comparison of the numerical model and the ideal spherical case. (c) Solution chart for a measured flow rate and water pressure change.

5.3.2.3 Calibration:

Four porous filters are calibrated under: flow-control (low flow rate) and pressure-control (high flow rate; set-up in Figure 5.18). The filters include a standard CPT plastic filter and 3 filters made of stainless steel 316 with different pore sizes. Results are compared with numerical simulations to match the pressure drop ΔP ; all filters exhibit high conductivity ($> 10^{-3}$ cm/s).

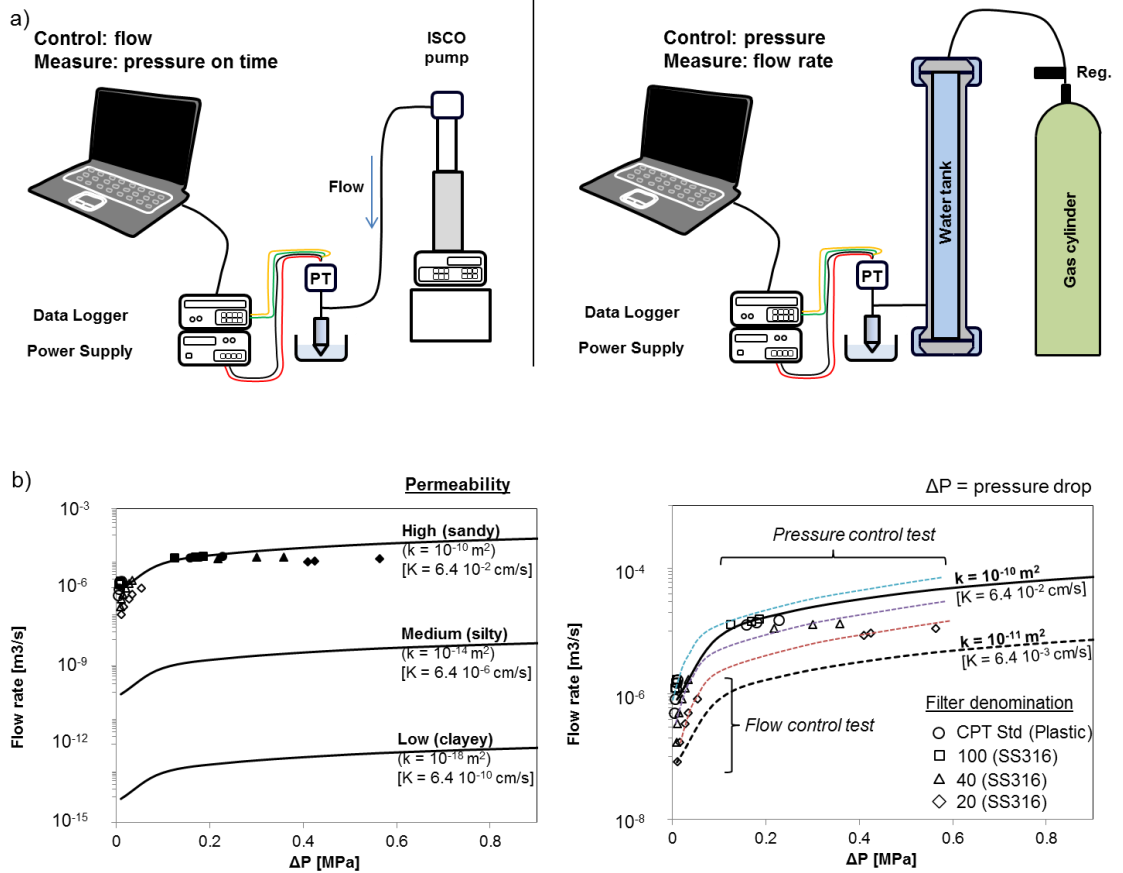


Figure 5.18. Porous filter calibration: (a) Setup of the two types of control tests: flow control and pressure control-based test. (b) Results for different porous filter. Lines represent results from numerical simulations and discrete points show measured values.

Fluid sampling tests are shown in Figure 5.19 and results for $\Delta p = u_o - p_o = 0.33$ MPa, for different filter types. Measurement must fall on the right hand side of plots to disregard measurement errors.

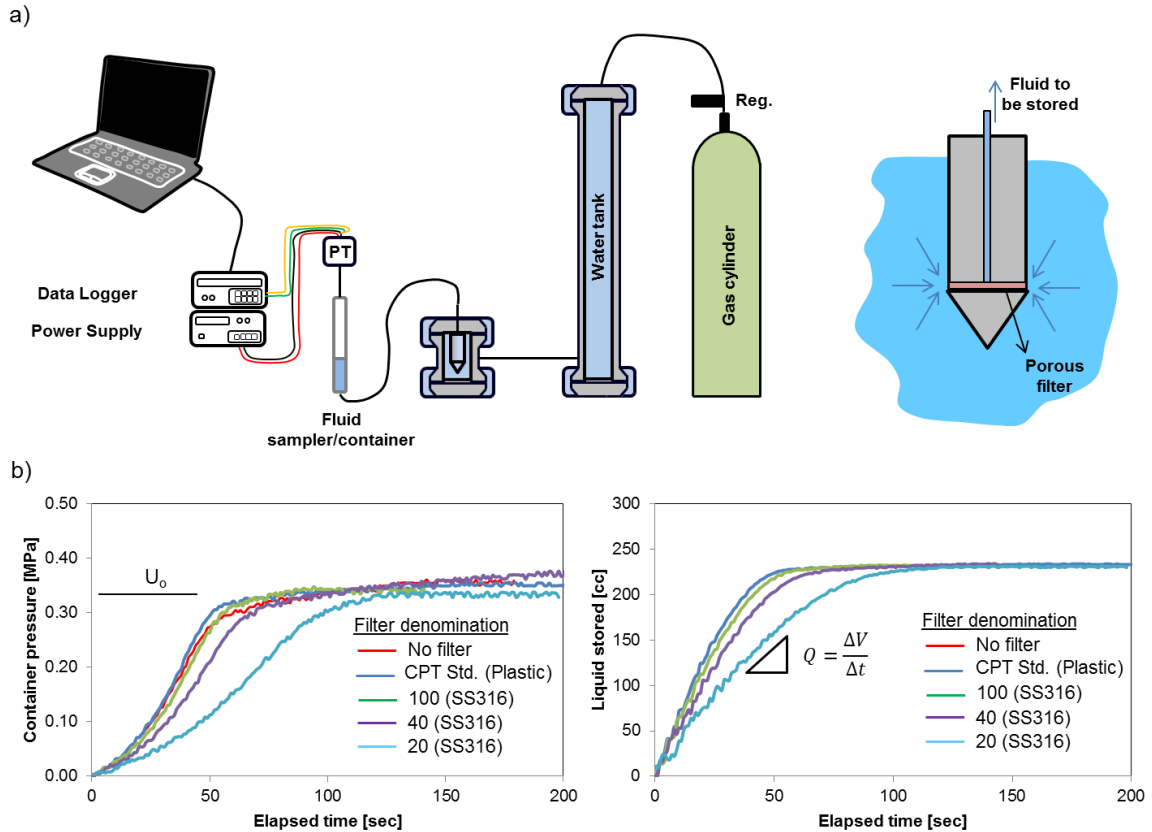


Figure 5.19. Complete hydraulic/fluid sampling test: (a) Setup. (b) Results for different porous filters.

5.3.3 Electrical Resistivity

5.3.3.1 Design:

The local electrical resistivity is measured using a button-type electrode pair. A small PEEK plastic screw (OD = 9.4 mm) is used for electrical insulation. The steel module works as the ground and the central electrode in the button is the active electrode. The button-type electrode pair can be deployed in any module of the penetrometer (Figure 5.20). The peripheral electronics involves an AC source (frequency $f = 100$ kHz) and two voltmeters (details in Cho et al., 2004).

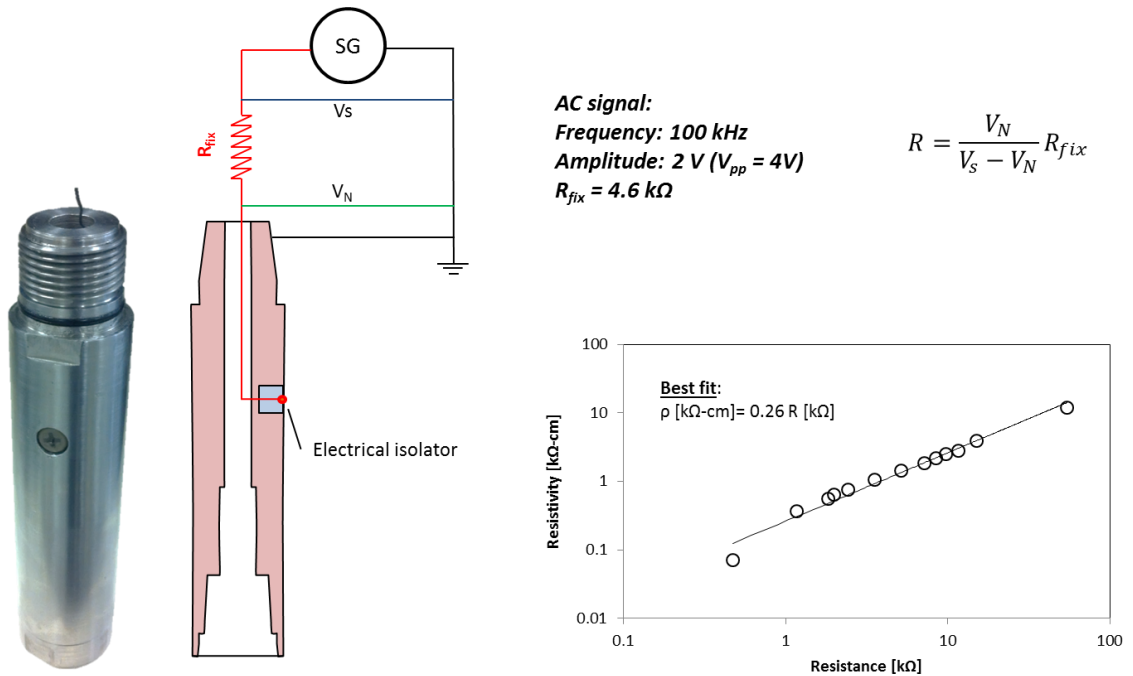


Figure 5.20. Electrical resistivity module and calibration.

5.3.3.2 Calibration:

The button-type electrode pair is calibrated for different values of electrical resistivity. Figure 5.20 shows the setup and calibration results. These results allow for the direct comparison of voltage drop ratio onto electrical resistivity, that is the inherently account for the shape factor associated to the 3D electric field.

5.3.4 Sediment Sampling

5.3.4.1 Design:

Small tube samplers are attached to the tool body to recover disturbed samples (Figure 5.21). These samplers do not satisfy the rules and guidelines proposed in Chapter 2 because they are limited to disturbed specimens only. The samplers consist of a cutting shoe, sampler tube and catcher. The cutting shoe is designed with a taper angle of 10 degrees and an internal step to lock the catcher against the sampler. The sampler tube

houses the recovered sediment kept in place by the catcher. The tube is threaded at the top to mount the sampler to the body of the tool. An extrusion device is designed to push sediments out of the tube sampler (Figure 5.21-e).

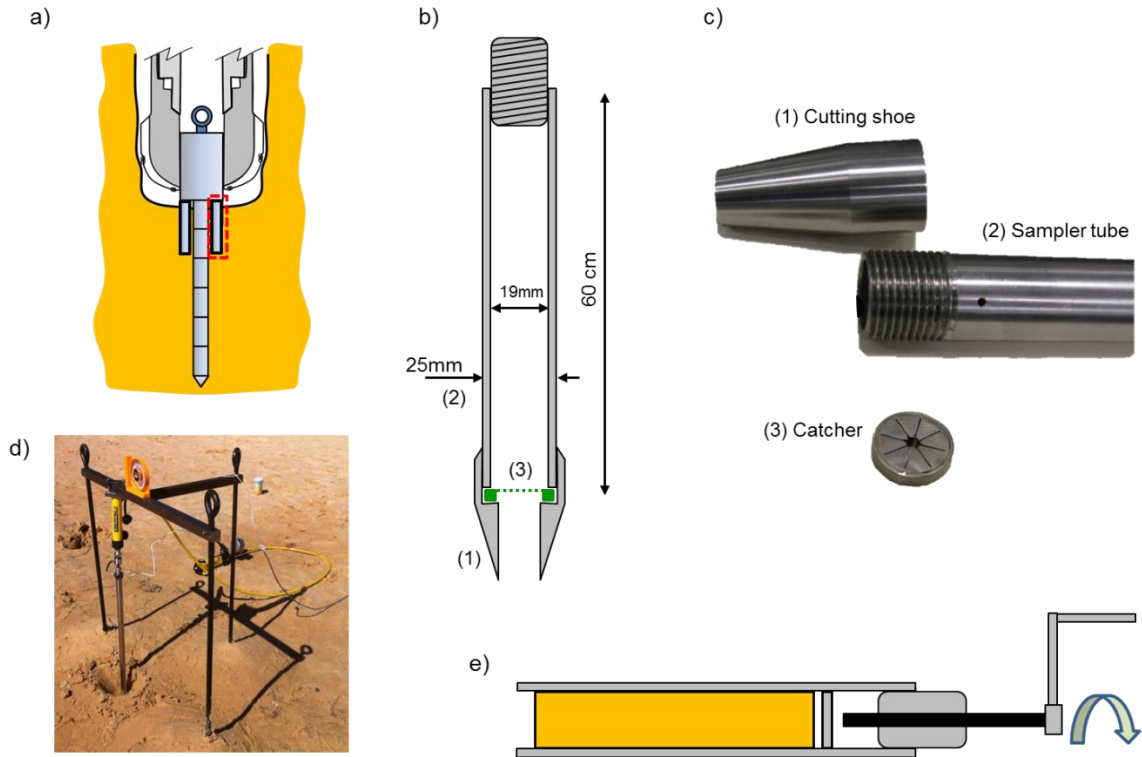


Figure 5.21. Sediment piston sampler. (a) Position in tool. (b) Drawings. (c) Photographs. (d) Field test. (e) Extrusion device.

5.3.4.2 Field Verification:

The first test documented in Chapter 2 (Section 2.6) confirmed the good performance of the sampler for coarse and fine grained soils.

5.4 Future Modules

5.4.1 Thermal Conductivity, Stiffness , Video and Frictional Sleeve

Thermal conductivity/diffusivity can be determined in active mode with a known heat source (either during heating or after shut off) and a thermocouple that is used to

record the temperature change in time (Farouki 1981; ASTM D5334-08; Webb 1956; Rosenbaum et al. 2007; Cortes et al 2009). A passive method can be implemented as well using the heat generated during probe penetration into the sediment (the typical increase in temperature is low $\Delta T < 1^\circ \text{C}$). The passive method has been successfully used to characterize marine sediments (Blackwell, 1954; Herzen and Maxwell, 1959; Hyndman et al., 1979; Pfender and Villinger, 2002; Ruppel 2003).

The middle-strain stiffness module conceived for this system is analogous to a pressuremeter. A precise volume controlled syringe pump located in the tool body can inject small volumes while pressure is monitored (Clarke 1995).

A module with video capability has been prototyped and tested in the lab. The approach resembles video-cone developments by Hryciw and co-workers (Raschke and Hryciw 1997; Hryciw et al. 1998; Hryciw et al. 2003). It is based on a standard Arduino friendly camera installed behind a sapphire window. Images of grains obtained in preliminary tests using this technology are shown in Figure 5.22.

A module with interchangeable sleeves of different roughness can be readily mounted on the system to facilitate the characterization of shear resistance (Frost and DeJong 2005; DeJong and Frost 2002).

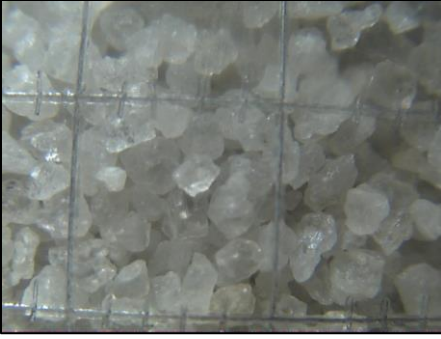
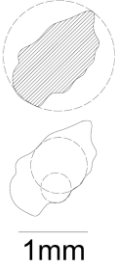
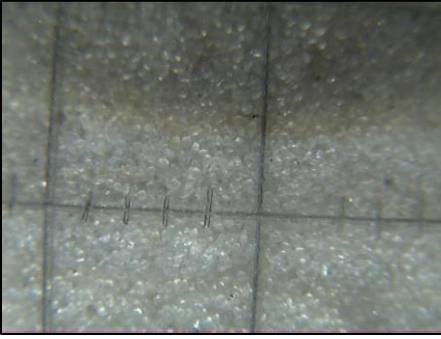

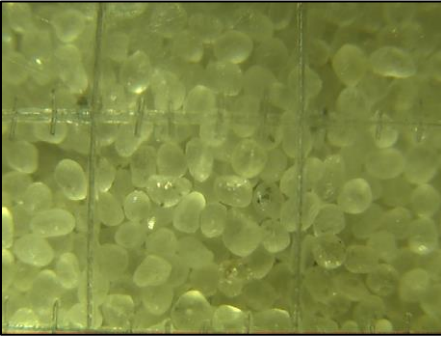
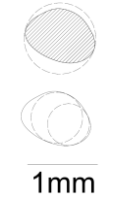
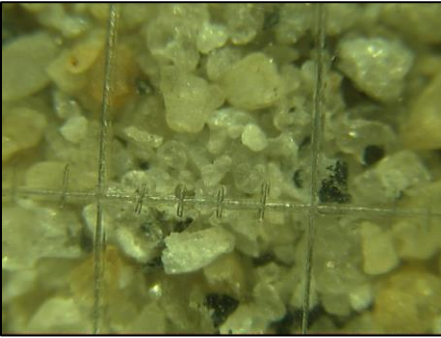
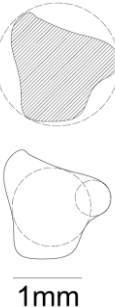
Images	Typical grain	Properties						
		<p style="text-align: center;"><u>Blasting sand</u></p> <table border="1" data-bbox="971 380 1422 491"> <thead> <tr> <th></th> <th>From image</th> <th>From sieve</th> </tr> </thead> <tbody> <tr> <td>D₅₀</td> <td>1.1mm</td> <td>0.90mm</td> </tr> </tbody> </table> <p>Sphericity = 0.51 Roundness = 0.55</p>		From image	From sieve	D ₅₀	1.1mm	0.90mm
	From image	From sieve						
D ₅₀	1.1mm	0.90mm						
		<p style="text-align: center;"><u>Silica Sand</u></p> <table border="1" data-bbox="971 730 1422 842"> <thead> <tr> <th></th> <th>From image</th> <th>From sieve</th> </tr> </thead> <tbody> <tr> <td>D₅₀</td> <td>0.35mm</td> <td>0.30mm</td> </tr> </tbody> </table> <p>Sphericity = 0.56 Roundness = 0.38</p>		From image	From sieve	D ₅₀	0.35mm	0.30mm
	From image	From sieve						
D ₅₀	0.35mm	0.30mm						
		<p style="text-align: center;"><u>Ottawa sand 20-30</u></p> <table border="1" data-bbox="971 1110 1422 1222"> <thead> <tr> <th></th> <th>From image</th> <th>From sieve</th> </tr> </thead> <tbody> <tr> <td>D₅₀</td> <td>0.80mm</td> <td>0.74mm</td> </tr> </tbody> </table> <p>Sphericity = 0.70 Roundness = 0.81</p>		From image	From sieve	D ₅₀	0.80mm	0.74mm
	From image	From sieve						
D ₅₀	0.80mm	0.74mm						
		<p style="text-align: center;"><u>Mixed grains</u></p> <table border="1" data-bbox="971 1463 1422 1575"> <thead> <tr> <th></th> <th>From image</th> <th>From sieve</th> </tr> </thead> <tbody> <tr> <td>D₅₀</td> <td>0.90mm</td> <td>0.70mm</td> </tr> </tbody> </table> <p>Sphericity = 0.65 Roundness = 0.45</p>		From image	From sieve	D ₅₀	0.90mm	0.70mm
	From image	From sieve						
D ₅₀	0.90mm	0.70mm						

Figure 5.22. Video capability prototype test. Image analysis of typical grain compares well with sieving analysis in coarse grains. Sphericity = area of particle projection / area of the circle with diameter equal to the longest length of the projection. Roundness = average radius of curvature of surface features / radius of maximum sphere that can be inscribed.

5.5 Conclusions

Coring and sampling introduces unavoidable sample disturbance even when pressure core technology is used (Chapter 2). A new tool is designed and built to obtain valuable reservoir information and parameters in-situ.

- The prototype currently available can measure: insertion force, temperature, hydraulic conductivity, fluid sampling, production test, gas extraction and electrical conductivity. The device can readily accommodate modules to determine: stiffness, thermal conductivity, and sediment video/photography.
- The tool includes two sediment samplers to recover specimens for index properties.
- This tool is designed for high water pressure ($u = 40$ MPa) and insertion forces ($F = 90$ kN). It can be deployed in a wide range of seafloor and reservoir conditions, with emphasis on hydrate bearing sediments.
- Its modular structure is specifically selected for versatility and adaptation.
- Available modules have been calibrated for the range of typical values expected in hydrate bearing sediments reservoirs.
- Its field deployment is expected in 2016.

CHAPTER 6

MAXIMUM RECOVERABLE GAS FROM HYDRATE BEARING SEDIMENTS (DEPRESSURIZATION)

6.1 Introduction

Natural gas hydrates are crystalline water and gas compounds. Stable thermodynamic conditions are met at high pressure and low temperature. Estimates of the global accumulation vary between $3 \times 10^{15} \text{ m}^3$ and 10^{17} m^3 while the technically recoverable volume is on the order of $3 \times 10^{14} \text{ m}^3$ (Sloan and Koh 2007; Boswell and Collett, 2011; Figure 6.1).

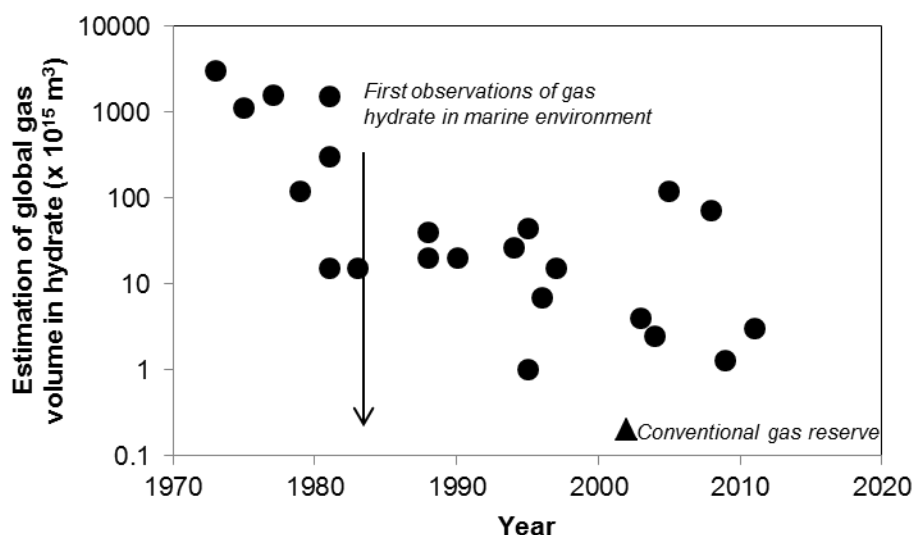


Figure 6.1. Estimation of global gas on the state of hydrate gas. From Sloan and Koh (2007); Boswell and Collett (2011). Notice conventional gas reserves are still orders of magnitude less than the worst of hydrate gas estimations.

Gas reservoirs in hydrate bearing sediments can be classified as (Moridis and Collett 2003; Moridis et al. 2011 and Moridis and Sloan 2007):

- **Class 1:** high hydrate saturation layer on top of a layer with free gas and water (i.e. Bottom Simulating Reflector BSR).

- **Class 2:** similar to class 1 but there is no free gas beneath (only mobile water).
- **Class 3:** absence of free fluids underneath (semi confined aquifer).
- **Class 4:** low hydrate saturation (< 10%), and lack of confining stratum.

Class 1 reservoirs are most desirable because they are next to the phase boundary and a low energy input is required for dissociation. Class 4 is least desirable because they lack confinement and can lead to very low recovery efficiency.

Sandy deposits are currently preferred because of their high permeability and low compressibility. Reservoirs that are considered to be commercially feasible given today's state of the art are listed in Table 6.1.

Table 6.1: Selected reservoirs gas volume estimation.

Location	Gas estimation [m ³]	Reference
Mallik (Canada)	3 10 ⁹ to 4 10 ⁹	Moridis, 2002
Gulf of Mexico	6 10 ¹⁴	BOEM report 2012
Mount Elbert (Alaska)	4 10 ⁹	BOEM report 2012
Atlantic coast USA	6 10 ¹⁴	BOEM report 2012
Pacific coast USA	2.3 10 ¹⁴	BOEM report 2012
Ulleung Basin (Korea)	10 ¹⁵ to 10 ¹⁸	Moridis, 2013
Nankai Trough(Japan)	5.6 10 ¹¹	Fujii et al 2013
ShenhuArea (China)	1.6 10 ⁹	Wu et al. 2010
Krishna-Godavari basin (India)	9.8 10 ⁸ to 5.6 10 ⁹	Shankar and Riedel 2011

Note: the amount of gas in place, technically and economically recoverable is still under discussion, and its values change with respect to authors and computation methods (Figure 6.1).

Methane gas can be produced from hydrate bearing sediments by (Moridis et al. 2008; Santamarina and Jang, 2009; Jang and Santamarina, 2011): (a) *depressurization*; (b) *thermal stimulation*; (c) *inhibitor's injection*, and (d) *CO₂-CH₄ replacement*. Several field tests have taken place as summarized in Table 6.2.

Table 6.2: Well tests summary in chronological order

Name	Loc.	Year	Dur.	Type	Form.	S _{hyd} [%]	Meas. k _{eff} [mD]	Gas produced [m ³]	Affected radius [m]	Observ.	Reference
Mallik	Canada	2002	123.7 hrs	Thermal stim.	Sand	60 to 85	0.001 to 0.1	468	3	Formation solids were produced	Hancock et al. (2005); Moridis et al. (2011)
Mt. Elbert	Alaska	2007	Several tests up to 13 hrs each	Depress.	Sand	50 to 70	0.12 to 0.17	7 10 ⁻⁴	0.05 to 0.15		Boswell et al. (2008); Hunter et al. (2011); Anderson et al (2008)
Mallik	Canada	2007	15hrs	Depress.	Sand	60 to 85	0.1 to 1	830	ND	Sand inflow causes operational problems	Dallimore et al. (2008)
		2008	6 days (139 hrs)	Depress.			ND	13000	ND		Yamamoto and Dallimore (2008)
Nankai Trough	Japan	2013	6 days	Depress.	Layered	ND	ND	120000	ND	First offshore production	www.jogmec.go.jp

mD = 10⁻¹² m²

ND = No data provided

The analysis of gas production requires complex coupled thermo-hydro-mechanical codes such as (Moridis et al. 2014; Hong and Pooladi-Darvish 2005; Moridis et al. 2008; Walsh et al. 2009; Konno et al. 2010; Pruess 2003; CMG 2012; Nagao 2011): TOUGH + HYDRATE (Lawrence National Lab), MH21-HYDRES (Japan Oil Engineering Company), CMG-STARs (Computer Modelling Group, Canada), STOMP-HYD (Pacific Northwest National Laboratory). These codes involve a large number of equations, constitutive relations and parameters. They are complex and suffer from time- and space-discretization errors (Pooladi-Darvish 2004). Table 6.3 shows some of the key parameters involved in these simulations.

Analytical solutions have been proposed to analyze local conditions (Kwon et al. 2008) thermal stimulation (Ullerich et al. 1987; Esmailzadeh et al. 2011; Klar et al., 2013), and depressurization (Goel et al, 2001; Ji et al., 2001; Hong et al. 2003; Tsyppin 2000). However these analyses remain complex, require iterative solution and hide explicit relations between governing parameters.

The pressure distribution in radial flow is inversely proportional to the logarithm of the radial distance to the well. Therefore there is a physical limit to the zone around a well that can experience pressure-driven dissociation. The study reported herein was conducted to develop a simple and robust set of equations to estimate limits for gas production from hydrate bearing sediments using depressurization.

Table 6.3: Summary of selected parameter used in numerical simulations

Well rad. [m]	Dom. radius [m]	Hyd. thick. [m]	Initial press. [MPa]	Well press. [MPa]	Initial temp. [K]	Intrinsic Perm. [m ² or mD]	Porosity [--]	Reference
0.1	10000	1	5.7	2.7	278.85	1 10 ⁻¹⁵ to 1 10 ⁻¹² m ²	0.30 to 0.60	Moridis and Sloan (2007)
ND	567.5	15	10	ND	286.65	1 10 ⁻¹²	0.3	Moridis and Kowalsky (2006)
0.1	45	23	13	2.93	274.2	1 10 ⁻¹⁵	0.3	Li et al (2012)
ND	ND	20, 16, 10	10.8, 9, 10.8	ND	285	2 10 ⁻¹⁴	0.28	Moridis et al (2002)
0.1	450 to 1500	200	(Varies)	2.7	ND	1000 mD	0.3 to 0.64	Myshakin et al (2012)
0.1	100	10	11.5	3, 4 and 5	287.15	1 10 ⁻¹⁴	0.38	Su et al (2012)
0.1	400	11.3	6.4	3	275.5	1 10 ⁻¹²	0.4	Moridis et al (2011)
0.1	250	20	23	3	289	5 10 ⁻¹³ (**)	0.45 to 0.65	Moridis et al (2013)
ND	120	70, 100	13, 8.7, 13	3	287	1000 to 0.1 mD	0.3 to 0.4 (***)	Kurihara et al (2009)
0.1	45	22	13.8	0.2 Po	287	7.5 10 ⁻¹⁴	0.41	Li et al (2010)
0.1	250	50	6.7 to 12.13	4	282 to 287	10 to 500 mD	0.4	Konno et al (2010)

(*) computed from model proposed by Stone (1970) $r_A = (S^*_A)^n$; $S^*_A = (S_A - S_{irA})/(1-S_{irA})$; $k_{rG} = (S^*_G)^n$; $S^*_G = (S_G - S_{irG})/(1-S_{irG})$

(**) estimated value

(***) varies for clay, silt and sand

(****) For the case of Class 3, 14deg C and $k_o = 500\text{mD}$

ND = no data provided

Table 6.3: Summary of selected parameter used in numerical simulations (cont.)

Relative permeability

(*)

Water Gas

Hydrate saturation [--]	n [--]	S_{irA} [--]	S_{irG} [--]	Observations	Reference
0.02 to 0.1	4	0.2	0.02	Parametric study –Dissoc. pressure is computed by the software	Moridis and Sloan (2007)
0.7	3	0.25	0.02	Class 1 and 2 hydrate deposit studied	Moridis and Kowalsky (2006)
0.4	3.57	0.25	0.05	Simulating Qilian Mountain Permafrost - China	Li et al (2012)
0.8, 0.5, 0.8	4.2	0.2	0.05	Simulating different zones @ Mallik reservoir - Canada - vertical and horizontal wells	Moridis et al (2002)
0.05 to 0.80	3.16	0.18	0.02	Simulating layered sediments in Gulf of Mexico Walker Ridge 313 site	Myshakin et al (2012)
0.1, 0.2 and 0.3	5	0.3	0.03	Parametric study of Shenhu Area China	Su et al (2012)
0.65	4.2	0.2	0.02	Parametric study of Mount Albert, Alaska	Moridis et al (2011)
0.3 to 0.7	3.5	0.2	0.01	Simulating layered sediments Ulleung Basin, Korea	Moridis et al (2013)
0.1 to 0.96	ND	ND	ND	Layered system of sand, silt and clay of Nankai Trough, Japan	Kurihara et al (2009)
0.44	3.57	0.3	0.05	Sea of south of China, Shenhu	Li et al (2010)
0.6		$k = k_o (1-S_h)^2$		Class 1, 2 and 3 reservoirs	Konno et al (2010)

(*) computed from model proposed by Stone (1970) $k_{rA} = (S^*_A)^n$; $S^*_A = (S_A - S_{irA})/(1-S_{irA})$; $k_{rG} = (S^*_G)^n$; $S^*_G = (S_G - S_{irG})/(1-S_{irG})$

(**) estimated value

(***) varies for clay, silt and sand

(****) For the case of Class 3, 14deg C and $k_o = 500\text{mD}$

ND = no data provided

6.2 Analytical Solution

Consider a gas hydrate reservoir in a host sediment under high water pressure and low temperature. Gas production starts as soon as the decreasing pressure brings the hydrate outside stability conditions. The host sediment will experience: permeability changes, settlement, fines migration, unsaturation and gas expansion (Jang and Santamarina, 2011).

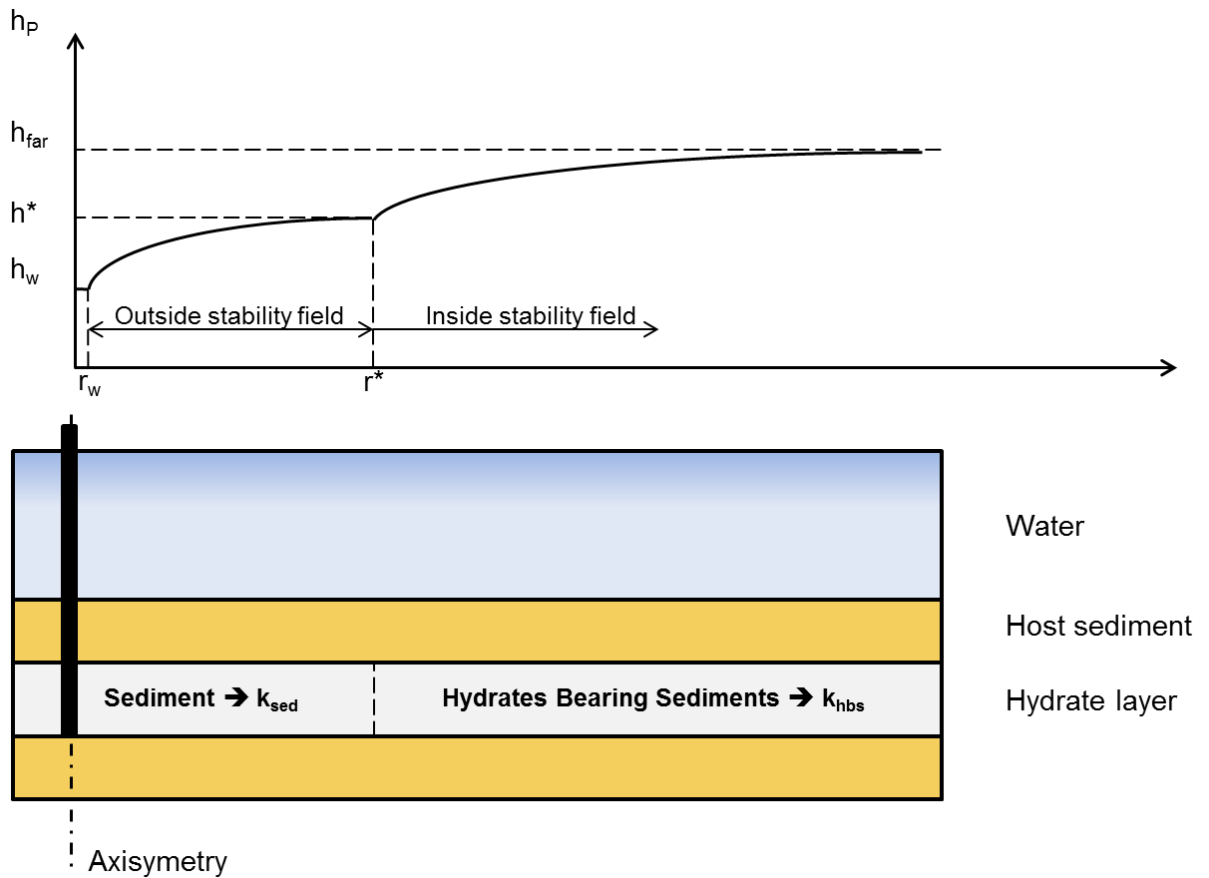


Figure 6.2. General description of the problem. Below the seafloor, a hydrate layer is located immersed in a generic host sediment. As soon as the production pipe decreases the pressure to h_w , two zones can be defined. The first one from the well to the dissociation front and beyond the dissociation front; both with different permeability values.

Note: sub-indices: w = well; far = far field; * = dissociation front

Two zones can be identified under steady state conditions when the pressure drop

is kept constant and hydrate stops dissociating (Figure 6.2): the inner zone where hydrate has been depleted, and the outer zone where hydrate remains stable. Let's define the size of the produced zone as r^* [m], and the total head pressure in the far field as h_{far} [m]. The inner zone is characterized by the permeability of the sediment without hydrates (k_{sed}) and the outer zone by the permeability of the hydrate bearing sediment (k_{hbs}). Clearly, gas was produced from the inner zone $r \leq r^*$.

6.2.1 Thin or Deep Reservoir Condition

The pressure field around a production well when continuity and Darcian conditions are satisfied is defined by Laplace's equation, in terms of the total energy E_{tot} , or of the total head $h_t = E_{tot}/mg$, where mg define the fluid unit weight; then, in cartitian coordinates:

$$\nabla E_{tot} = \nabla^2 h_t = 0 \quad (6.1)$$

However, stability conditions and the dissociation front are determined by the pore water pressure $u = (h_t - h_e) \gamma_w$, where u is the pore pressure, h_e elevation pressure. In most cases, the thickness of the hydrate bearing sediment layer is much smaller than the depth at which the hydrate layer is located or depressurization is much greater than the affected geometry $\Delta u \gg \Delta h_e$. Then we can assume that the effect of elevation on total head is negligible, and we link total head h_t directly to pressure head $u = h_t$. Then fluid pressure becomes $u = h_t \gamma_w$. Spherical and axisymmetric flow conditions are analyzed next.

6.2.2 Homogeneous Formation: Spherical Flow Condition

Radial flow. Laplace's equation in spherical coordinates is (Figure 6.3):

$$\nabla^2 h = \frac{1}{r^2} \frac{\partial}{\partial r} \left(r^2 \frac{\partial h}{\partial r} \right) + \frac{1}{r^2 \sin(\theta)} \frac{\partial}{\partial \theta} \left(\sin(\theta) \frac{\partial h}{\partial \theta} \right) + \frac{1}{r^2 \sin^2(\theta)} \frac{\partial^2 h}{\partial \xi^2} = 0 \quad (6.2)$$

where the azimuthal angle θ , the polar angle ξ and the radius r define the location of any point on a sphere.

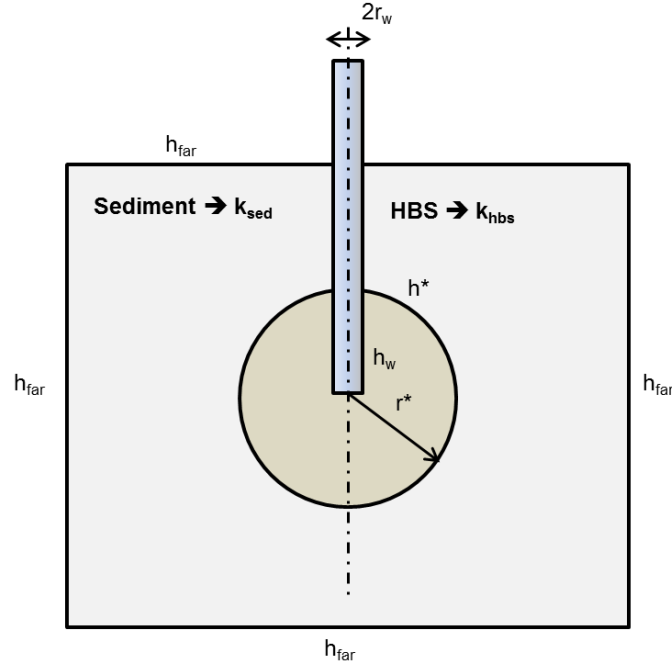


Figure 6.3. General description for the spherical dissociation front case.

Radial flow tangential derivatives are zero and the equation simplifies to:

$$\nabla^2 h = \frac{1}{r^2} \frac{\partial}{\partial r} \left(r^2 \frac{\partial h}{\partial r} \right) = 0 \quad (6.3)$$

Which means:

$$r^2 \frac{\partial h}{\partial r} = \text{constant} = C_1 \quad (6.4)$$

Hence:

$$h = -\frac{C_1}{r} + C_2 \quad (6.5)$$

Let's select the following boundary conditions:

$$\text{At the well: } h = h_w : \quad r = r_w \quad (6.6)$$

$$\text{At far field: } h = h_{far} : \quad r = r_{far}$$

Where r_w [m] is the well radius and r_{far} [m] is the radius of influence of the well. Then:

$$h_w = -\frac{C_1}{r_w} + C_2 \quad \text{and} \quad h_{far} = -\frac{C_1}{r_{far}} + C_2 \quad (6.7)$$

Which gives us:

$$h = \frac{h_{far} - h_w}{\frac{1}{r_{far}} - \frac{1}{r_w}} \left(\frac{1}{r} - \frac{1}{r_w} \right) + h_w \quad (6.8)$$

The velocity can be computed from Darcy's law:

$$v_r = -k \frac{\partial h}{\partial r} = k \frac{h_{far} - h_w}{\frac{1}{r_{far}} - \frac{1}{r_w}} \frac{1}{r^2} \quad (6.9)$$

where k [m/sec] is the permeability. The flow rate q [m³/sec] becomes:

$$q = -k \int_0^{2\pi} d\xi \int_0^\pi r^2 v_r \sin(\theta) d\theta \quad (6.10)$$

If the total head is known at two radial distances r_1 and r_2 , then the flow rate is:

$$q = k \frac{4\pi(h_2 - h_1)}{\frac{1}{r_1} - \frac{1}{r_2}} \quad (6.11)$$

Dissociation Boundary r^* . At state conditions, the dissociation front stops expanding at the terminal position r^* , there is no more dissociation, and water flow rate continuity is satisfied at the boundary between the inner hydrate-free sediment and outer hydrate bearing medium. Hence:

$$q_{sed} = q_{hbs} \quad (6.12)$$

$$\frac{(h^* - h_w)k_{sed}}{\frac{1}{r_w} - \frac{1}{r^*}} = \frac{(h_{far} - h^*)k_{hbs}}{\frac{1}{r^*} - \frac{1}{r_{far}}} \quad (6.13)$$

Since $1/r_{far} \rightarrow 0$, this equation predicts that the size of the dissociation front r^* can be estimated as (Figure 6.4):

$$r^* = r_w \left(1 + \frac{k_{sed}}{k_{hbs}} \frac{h^* - h_w}{h_{far} - h^*} \right) \quad (6.14)$$

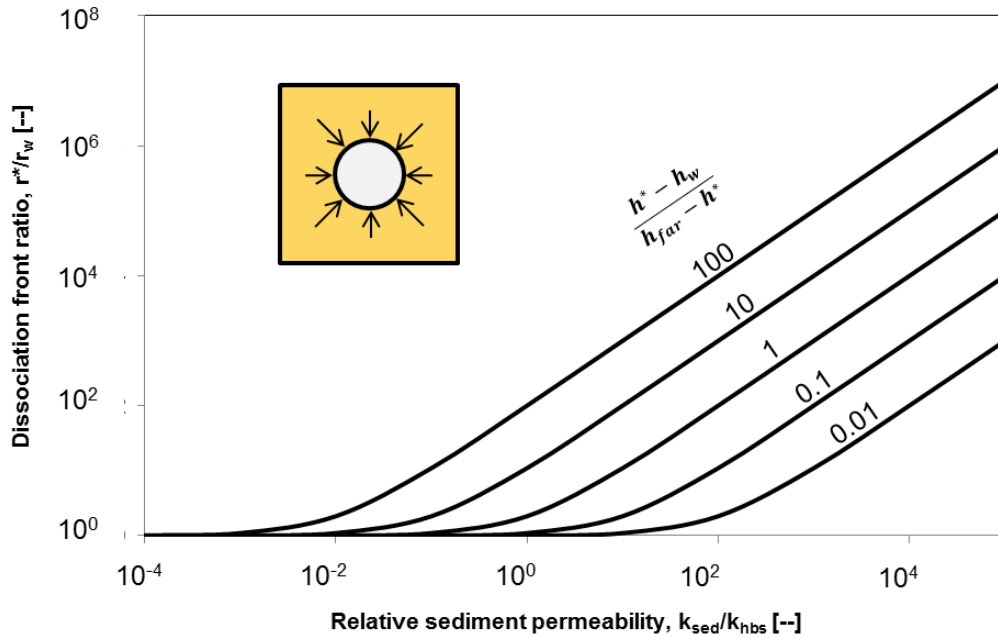


Figure 6.4. Spherical dissociation front. Relationship between dissociation radius, permeabilities and pressure.

6.2.3 Layered Formation: Axisymmetric Flow with Leak-in Condition

Consider a hydrate bearing sandy reservoir confined between two low permeability layers (Figure 6.5-a).

The conservation of mass in this annulus is:

$$q_r = q_{r+dr} + \Delta q \quad (6.15)$$

$$V_r 2\pi r H = V_{r+dr} 2\pi (r + dr) H + \pi [(r + dr)^2 - r^2] V^+ \quad (6.16)$$

where V^+ [m/sec] is the velocity perpendicular to the horizontal plane. Once again, this equation is in terms of h_t , however we consider small changes in elevation so that $h_t \approx u$.

Applying Darcy's law:

$$k \left. \frac{\partial h}{\partial r} \right|_r 2rH = k \left. \frac{\partial h}{\partial r} \right|_{r+dr} 2(r + dr)H + 2r dr k' \frac{h^+ - h}{b} \quad (6.17)$$

where h is the total head at any point evaluated at a determined distance, k' [m/s] is the aquitar permeability, b [m] the aquitard layer thickness and h^+ is the total head outside

the semi-confined aquifer.

$$\frac{\frac{\partial h}{\partial r}\Big|_r - \frac{\partial h}{\partial r}\Big|_{r+dr}}{dr} rH = \frac{\partial h}{\partial r}\Big|_{r+dr} H + r \frac{k'}{k} \frac{h^+ - h}{b} \quad (6.18)$$

$$\frac{\partial^2 h}{\partial r^2} = \frac{1}{r} \frac{\partial h}{\partial r} + \frac{k'}{k} \frac{h^+ - h}{Hb} \quad (6.19)$$

The solution of this equation is (De Glee 1951):

$$q = \frac{2 \pi k H}{K_0 \left(\frac{r}{\sqrt{\frac{k H b}{kr}}} \right)} \quad (6.20)$$

where K_0 is the modified hyperbolic Bessel function of the second kind and order zero.

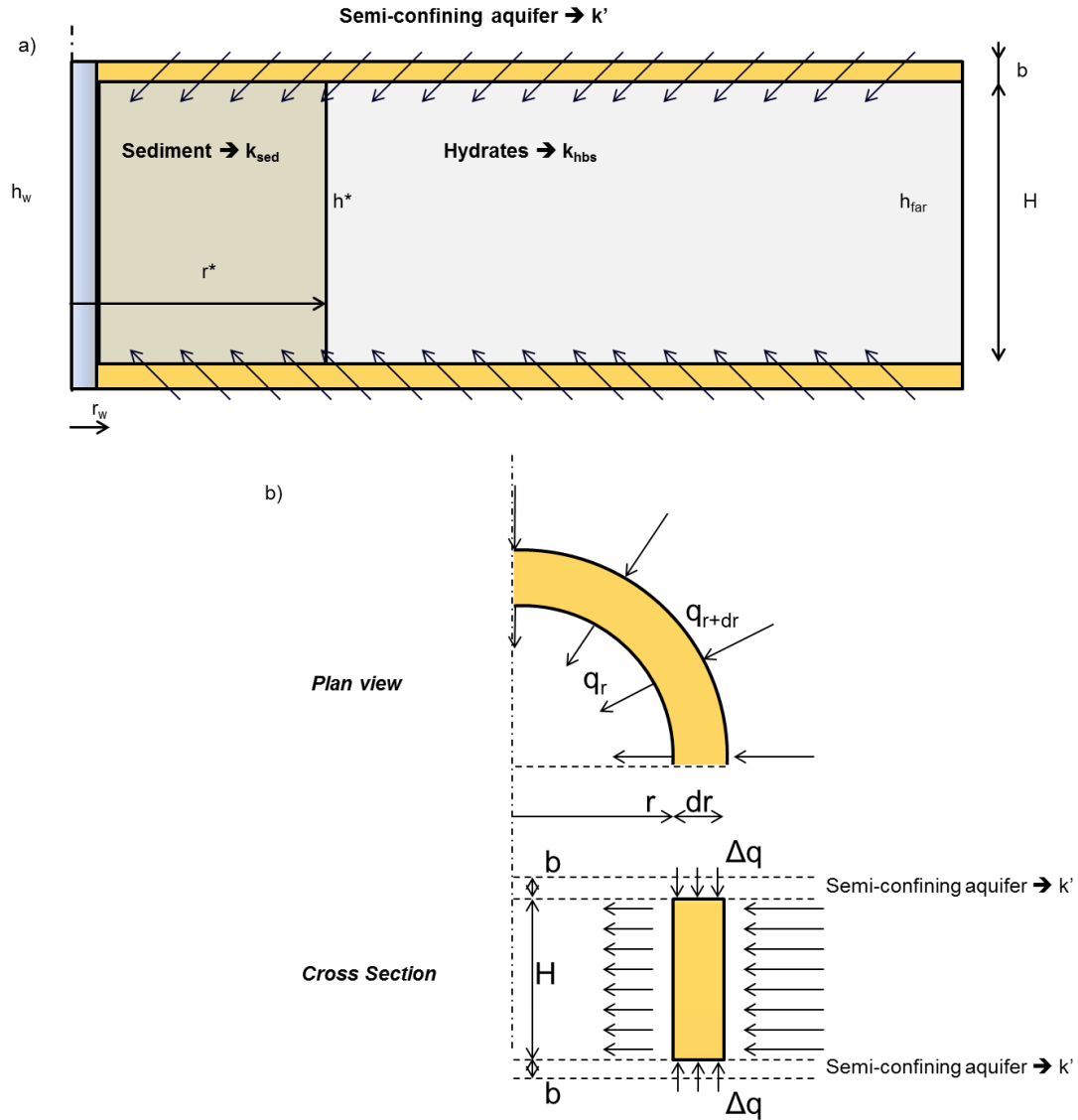


Figure 6.5: Leaky aquifer case. a) General description, where H = hydrate layer thickness, k_{sed} = sediment permeability, k_{hyd} = hydrate layer permeability, h_w = well water pressure, h^* = dissociation pressure, h_{far} = far field water pressure, r^* = dissociation front, r_w = well radius. b = aquitard thickness, k' = aquitard permeability. (b) General description for the double semi-confined aquifer.

For steady state conditions, the water flow rates at the boundary between the hydrate free inner zone and outer hydrate bearing sediment zones satisfy mass conservation:

$$q_{sed} = q_{hbs} \quad (6.21)$$

$$\frac{k_{sed} (h^* - h_w)}{K_0 \left(\frac{r_w}{\sqrt{\frac{k_{sed} H b}{k'}}}} = \frac{k_{hbs} (h_{far} - h^*)}{K_0 \left(\frac{r^*}{\sqrt{\frac{k_{hbs} H b}{k'}}}} \right)} \quad (6.22)$$

$$\frac{k_{sed} (h^* - h_w)}{k_{hbs} (h_{far} - h^*)} = \frac{K_0 \left(\sqrt{\frac{k'}{k_{sed}} \frac{r_w^2}{H b}} \right)}{K_0 \left(\sqrt{\frac{k'}{k_{hbs}} \frac{r^{*2}}{H b}} \right)} \quad (6.23)$$

Different approximations to Bessel functions are identified for different ranges of the argument. Figure 6.6 shows the hyperbolic Bessel function of the second kind and order zero, and two different approximations: a logarithmic function fits best for the argument < 0.5 , while the exponential fits best for $0.3 < \text{argument} < 7$.

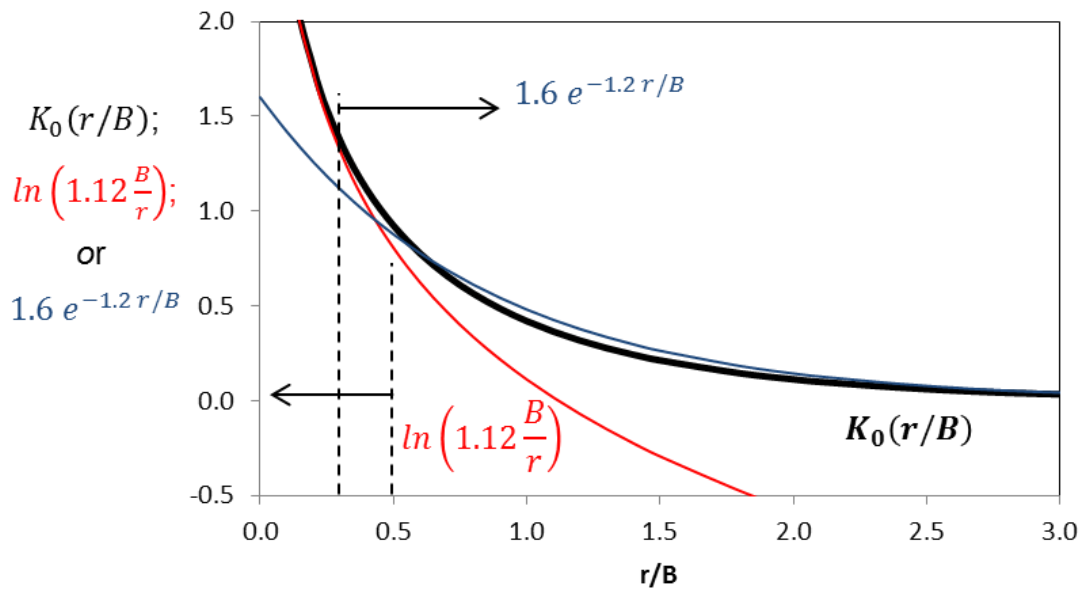


Figure 6.6. Leaky aquifer case. Best fit for Bessel equation (K_0) for $r/B < 0.5$ and $r/B > 0.3$.

Note: $B = \sqrt{\frac{k H b}{k'}}$

Then the following explicit equations apply to different scenarios:

$$\text{Case A: } \sqrt{\frac{k' r_w^2}{k_{sed} H b}} < 0.5 \quad \text{and} \quad \sqrt{\frac{k' r^{*2}}{k_{hbs} H b}} < 0.5$$

$$\frac{k_{sed}}{k_{hbs}} \frac{h^* - h_w}{h_{far} - h^*} = \frac{\text{Ln} \left(1.12 \sqrt{\frac{k_{sed} H b}{k' r_w^2}} \right)}{\text{Ln} \left(\frac{1.12 \sqrt{\frac{k_{hbs} H b}{k'}}}{r^*} \right)} \quad (6.24)$$

$$\frac{r^*}{r_w} = \frac{1.12 \sqrt{\frac{k_{hbs} H b}{k' r_w^2}}}{\left(1.12 \sqrt{\frac{k_{sed} H b}{k' r_w^2}} \right)^{\left(\frac{k_{sed}}{k_{hbs}} \frac{h^* - h_w}{h_{far} - h^*} \right)^{-1}}} \quad (6.25)$$

$$\text{Case B: } \sqrt{\frac{k' r_w^2}{k_{sed} H b}} > 0.3 \quad \text{and} \quad \sqrt{\frac{k' r^{*2}}{k_{hbs} H b}} > 0.3$$

$$\frac{k_{sed}}{k_{hbs}} \frac{h^* - h_w}{h_{far} - h^*} = \frac{1.6 e^{\left(\frac{-1.2 r_w}{\sqrt{\frac{k_{sed} H b}{k'}}}} \right)}{1.6 e^{\left(\frac{-1.2 r^*}{\sqrt{\frac{k_{hbs} H b}{k'}}}} \right)}} \quad (6.26)$$

$$\frac{r^*}{r_w} = \sqrt{\frac{k_{hbs}}{k_{sed}}} \left[1 + \frac{1}{1.2} \sqrt{\frac{k_{sed} H b}{k' r_w^2}} \text{Ln} \left(\frac{k_{sed}}{k_{hbs}} \frac{h^* - h_w}{h_{far} - h^*} \right) \right] \quad (6.27)$$

$$\text{Case C: } \sqrt{\frac{k' r_w^2}{k_{sed} H b}} < 0.5 \quad \text{and} \quad \sqrt{\frac{k' r^{*2}}{k_{hbs} H b}} > 0.3$$

$$\frac{k_{sed}}{k_{hbs}} \frac{h^* - h_w}{h_{far} - h^*} = \frac{\text{Ln} \left(1.12 \sqrt{\frac{k_{sed} H b}{k' r_w^2}} \right)}{1.6 e^{\left(\frac{-1.2}{\sqrt{\frac{k_{hbs} H b}{k' r^{*2}}}} \right)}} \quad (6.28)$$

$$\frac{r^*}{r_w} = \frac{1}{1.2} \sqrt{\frac{k_{hbs} H b}{k' r_w^2}} \text{Ln} \left[\frac{1.6 \frac{k_{sed}}{k_{hbs}} \frac{h^* - h_w}{h_{far} - h^*}}{\text{Ln} \left(1.2 \sqrt{\frac{k_{sed} H b}{k' r_w^2}} \right)} \right] \quad (6.29)$$

6.3 Discussion

The spherical is the simplest case, in which the relative sediment permeability k_{sed}/k_{hbs} and relative pressure dissociation control the dissociation front. Near the phase boundary ($h_{far} - h^*$) $\rightarrow 0$ and sediments with high hydrate saturation so that $k_{sed} \gg k_{hbs}$ lead to larger production zones r^* . The critical role of the “effective well radius” r_w is also highlighted.

For the leaky aquifer case scenario, the equations are defined with 10 variables controls the dissociation front: dissociation radius r^* , well effective radius r_w , hydrate layer thickness H , aquitard thickness b , hydrate bearing sediment permeability k_{hbs} , aquitard permeability k' , sediment permeability k_{sed} , dissociation pressure h^* , well pressure h_w and far field pressure h_{far} . Nevertheless, only two units are involved: [L] and [T], which means that there are 8 possible dimensionless ratios (Buckingham’s theorem). The equations for all cases already show important dimensionless ratios as: relative

sediment permeability $k_{\text{sed}}/k_{\text{hbs}}$, relative leak-in permeability k_{sed}/k' , relative pressure dissociation $(h^* - h_w)/(h_{\text{far}} - h^*)$ and a geometrical ratio $H b/r_w^2$. The comments for the spherical case also apply for the leak-in condition. The geometrical ratio represents the importance of the leaky aquifer respect to the hydrate bearing sediment layer, as H increases the production zone.

6.4 Recoverable Gas: Energy

The energy density of gas methane is $E_d = 46$ MJ/kg STP, while the density for hydrate is just $E_d = 4.8$ MJ/kg of hydrate mass (Hermann, 2005). The recoverable energy RE [J] from a hydrate bearing sediment with hydrate saturation S_{hyd} [--] when V [m^3] is:

$$RE = V n S_{\text{hyd}} E_d \rho_{\text{hyd}} e \quad (6.30)$$

where n is the porosity, and e the gas recovery efficiency. The recovery efficiency e depends on the interaction of gas with other fluids (such as water) in the reservoir as a function of pore size distribution and connectivity (Jang and Santamarina 2011). For the case when gas is the only fluid displaced and water remains in the reservoir (represents the case with maximum gas recovery).

$$e = \frac{\beta - 1}{\beta - 0.79} \quad (6.31)$$

where β is the fluid expansion factor as the ratio of the combined gas and water volumes to the initial volume of hydrate. Typical values are $\beta = 1.3$ ($u = 30$ MPa) and $e = 0.6$; and $\beta = 6$ ($u = 3$ MPa) and $e = 0.96$. Figure 6.7 shows the profit per hydrate thickness vs. radius of dissociation r^* estimated for selected reservoirs. The most profitable extraction reservoirs are the Ulleung Basin and Nankai Trough where the cost of gas is almost 4 times the price in USA (FERC: Federal Energy Regulatory Commission - www.ferc.gov). The low costs of gas extraction in USA hinder the possibility of gas extraction in the near future. Table 6.4 summarizes values used for these computations.

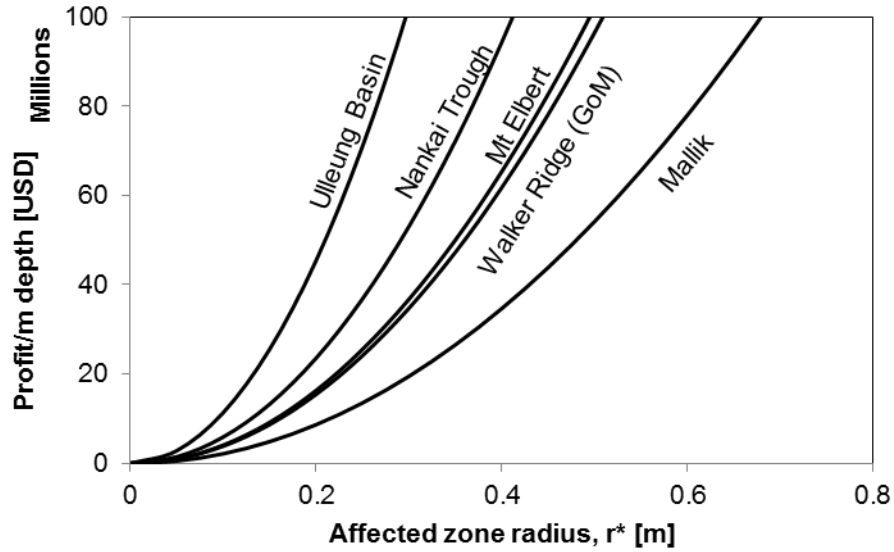


Figure 6.7. Economical analysis. Profit per hydrate thickness with respect to dissociation front for selected potential locations.

Table 6.4: Profit analysis

Parameter	Unit	Reservoir				
		Mallik	Walker Ridge (GoM)	Mt Elbert	Korea	Japan
H_{hyd}	[m]	10	200	11	20	100
k_{sed}	[m/s]	10^{-7}	10^{-7}	10^{-6}	10^{-6}	10^{-7}
k_{hbs}	[m/s]	10^{-9}	10^{-8}	10^{-9}	10^{-9}	10^{-8}
n	[--]	0.28	0.5	0.4	0.5	0.35
S_{hyd}	[--]	0.5	0.7	0.65	0.5	0.5
E_d	[MJ/kg]			46		
ρ_{hyd}	[kg/m ³]			920		
β	[--]	2.5	1.35	2.7	1.4	1.2
e	[--]	0.88	0.63	0.89	0.66	0.49
RE	[MJ/m ³]*	1703.7	3034.8	3210.5	2274.3	1184.3
Price (**)	[USD/MJ]		4220		16563.5	16510.75

(*) MJ per volume of dissociated gas

(**) Data from www.ferc.gov, 2013

6.5 Comparison with Literature

Numerical simulations show the time evolution of gas production typically for several years. However, the analysis conducted here is for steady state conditions at the end of gas production. Table 6.5 shows input values and numerical simulations results. Figure 6.8 compares numerical and analytical results. The close-form analytical solutions presented here predicts ultimate radius of dissociation to be within 1 and 1.15 the numerically computed value. The difference may be due to the fact that none of the numerical simulations are run to the ultimate radius, but a radius close to the final value.

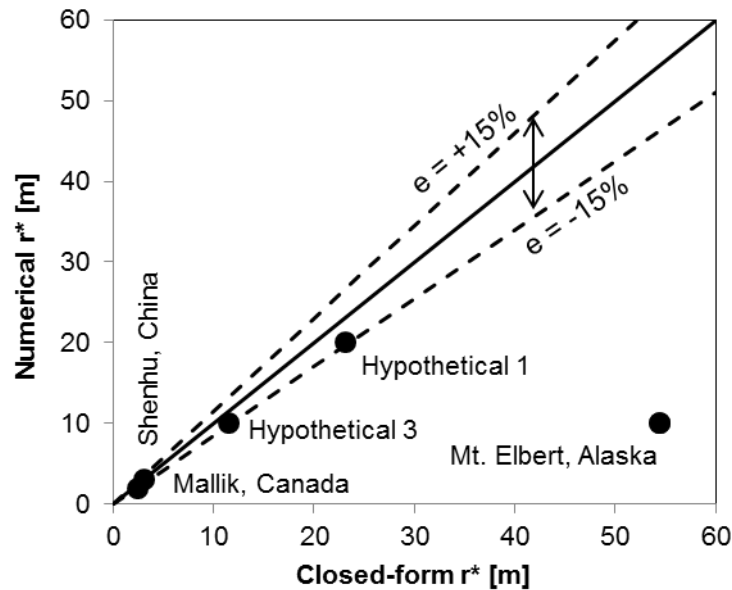


Figure 6.8. Comparison with literature cases. Dissociation front computed tends to be larger than the values from the literature but contained in a 15% error area. Note that Mt. Elbert simulations were stopped after 10800 days of production, therefore no ultimate radius of dissociation was reached.

Table 6.5: Data input for equations for selected cases

Case	H [m]	r _w [m]	b (*) [m]	k _{sed} [m/s]	k _{hbs} [m/s]	k' [m/s]	S _{hyd} [--]	h _w [MPa]	h _{far} [MPa]	h* (**) [MPa]	Data based on:	Solution	
												r* [m]	Vol gas [m3]
Hypothetical 1	1	0.1	1	6.5 10 ⁻⁹	3.810 ⁻⁹	1.010 ⁻¹⁴	0.10	2.70	5.70	4.70	Moridis et al (2007)	23.1	1.210 ⁴
Hypothetical 2	15	0.1	1	6.5 10 ⁻⁶	1.910 ⁻⁹	1.010 ⁻¹⁴	0.70	3.00	12.00	11.20	Moridis et al (2006)	3750.0	2.510 ¹⁰
Hypothetical 3	50	0.1	1	3.2 10 ⁻⁶	5.110 ⁻⁷	3.010 ⁻⁶	0.60	4.00	12.00	11.80	Konno et al (2010)	11.5	9.110 ⁵
Mallik, Canada	20	0.1	1	1.310 ⁻⁷	2.110 ⁻⁹	1.010 ⁻⁷	0.50	3.00	11.00	9.40	Moridis et al (2004)	2.5	1.05E+04
Mt Elbert, Alaska	11.3	0.1	1	6.510 ⁻⁶	5.7 10 ⁻⁹	1.010 ⁻¹⁰	0.65	3.00	6.40	3.20	Moridis et al (2011)	54.4	5.0 10 ⁶
Shenhu, China	10	0.1	1	6.510 ⁻⁸	3.910 ⁻⁹	1.010 ⁻⁷	0.30	3.00	12.00	11.84	Su et al (2012)	3.2	6.910 ³
Ulleung Basin, Korea	70	0.1	1	3.210 ⁻⁶	2.210 ⁻⁹	1.010 ⁻¹²	0.70	3.00	23.00	11.60	Moridis et al (2013)	1600.0	3.8 10 ¹⁰
Nankai Trough, Japan	22	0.1	1	6.510 ⁻⁷	1.310 ⁻⁸	1.010 ⁻¹²	0.50	3.00	13.00	11.60	Kurihara et al (2009)	1700.0	7.510 ⁹

(*) Assumed values

(**) Computed from temperature following Kwon et al (2008)

(***) Obtained from hydrate saturation front figures

H = hydrate bearing sediment layer thickness; r* = radius of dissociation; r_w = radius of the well; b = aquitard thickness; k_{sed} = sediment hydraulic conductivity; k_{hbs} = hydrate bearing sediment hydraulic conductivity; k' = aquitard hydraulic conductivity; S_{hyd} = hydrate saturation; h_w = well pressure; h_{far} = far field pressure, h* = dissociation pressure

ND = no data provided

Table 6.5: Data input for equations for selected cases (cont.)

Solutions from numerical simulations				
Case	r* (***) [m]	Vol gas [m3]	Observations	Reference
Hypothetical 1	20.0	$5 \cdot 10^3$	Confined aquifer	Moridis et al (2007)
Hypothetical 2	ND	$1 \cdot 10^8$	Class 1 reservoir: free gas zone - Confined aquifer	Moridis et al (2006)
Hypothetical 3	10.0	$1 \cdot 10^8$	Class 3 reservoir - non confined aquifer	Konno et al (2010)
Mallik, Canada	2.0	ND		Moridis et al (2004)
Mt Elbert, Alaska	10.0	$5.5 \cdot 10^6$	Simulation stopped after 10800 production days (not ultimate radius)	Moridis et al (2011)
Shenhu, China	4.0	$9 \cdot 10^3$		Su et al (2012)
Ulleung Basin, Korea	250.0	$9 \cdot 10^7$	r* reaches the boundary of the simulations - Confined aquifer	Moridis et al (2013)
Nankai Trough, Japan	120.0	$3 \cdot 10^7$	r* reaches the boundary of the simulations - Confined aquifer	Kurihara et al (2009)

(*) Assumed values

(**) Computed from temperature following Kwon et al (2008)

(***) Obtained from hydrate saturation front figures

ND = no data provided

6.6 Discussion: Real Case Scenario

The decrease in pore water pressure causes an increase in effective stress, volume compaction and the decreased sediment permeability k_{sed} . This is demonstrated next for the case of radial flow. Water pressure distribution is (Muskat 1946):

$$u(r) = \frac{h_{far} - h_w}{\log\left(\frac{r_{far}}{r_w}\right)} \log\left(\frac{r}{r_w}\right) + h_w \quad (6.32)$$

Effective stress is a function of the initial total stress σ_o at the depth of the reservoir. The change in void ratio for large stress is estimated as (e_{1kPa} is the void ratio at $\sigma' = 1$ kPa and β a soil parameter):

$$e(\sigma') = e_{1MPa} \left(\frac{\sigma'}{1MPa}\right)^{-\beta} \quad (6.33)$$

Where e_{1kPa} is an arbitrary reference value of void ratio; β a soil parameter.

Permeability can be found from (Ren and Santamarina; k_{1kPa} is the reference permeability at $\sigma' = 1$ kPa and b is a soil parameter which depends on specific surface – for the case of coarse grained soils $b = 3.5$):

$$k(e) = k_{1MPa} \left(\frac{e}{e_{1MPa}}\right)^b \quad (6.34)$$

With this new change in permeabilities, the pore water pressure distribution will be modified again. Note that the new pore water pressure distribution will lead a change in effective stress, void ratio and permeability. Figure 6.9 shows an example for the data from Nankai Trough (summarized in Table 6.6). Figure 6.9-a represents the initial pore pressure and effective stress distribution on the well and its impact on the void ratio, hydraulic conductivity and flow rate for a steady state condition (Figure 6.9-b, –c and –d). The permeability and flow rate fall several orders of magnitude.

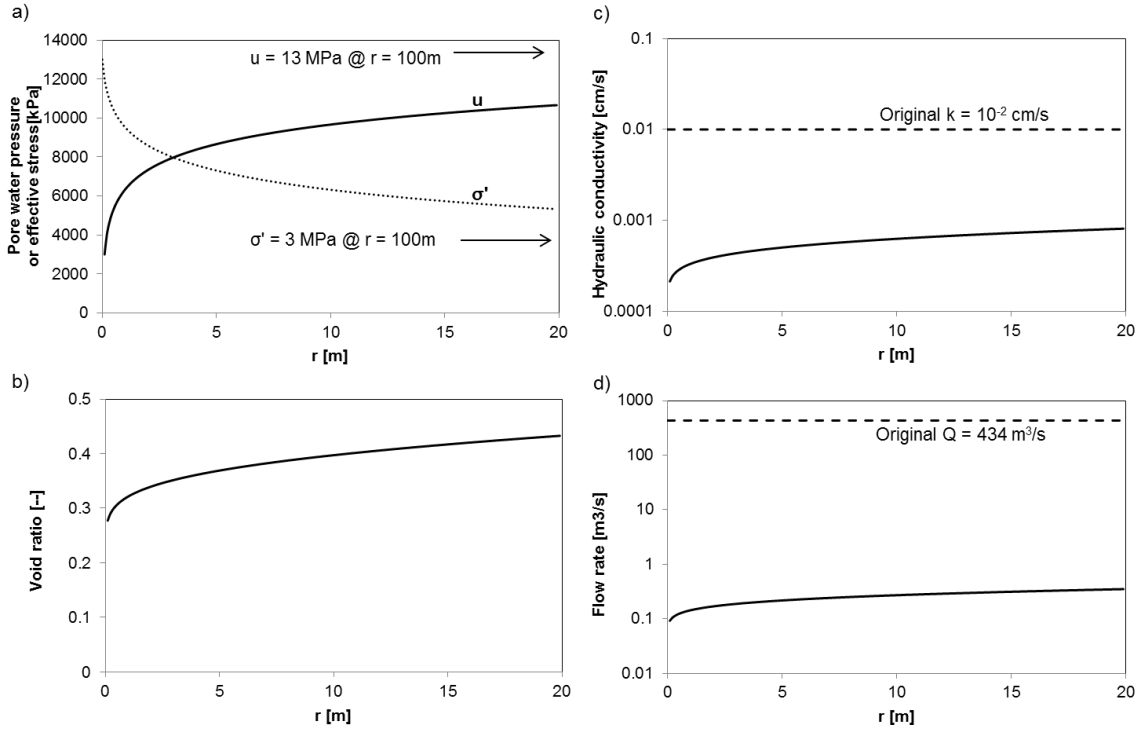


Figure 6.9. Example of gas hydrate production from a marine environment under depressurization strategy (Summary of parameters used can be found in Table 6.6).

Table 6.6: Summary of parameters for the example in Figure 6.9

Parameter	Symbol	Units	Value
Total stress in the reservoir	σ	[kPa]	16000
Initial water pressure	h_{far}	[kPa]	13000
Well water pressure	h_{w}	[kPa]	3000
Radius of influence	r_{far}	[m]	100
Radius of the well	r_{w}	[m]	0.1
Reservoir thickness	H	[m]	1
Permeability exponent	b	[--]	3.5
Void ratio exponent	β	[--]	0.5
Reference void ratio	$e_{1\text{MPa}}$	[--]	1
Reference permeability	$k_{1\text{MPa}}$	[cm/s]	10^{-2}

6.7 Conclusions

- Gas production by depressurization is limited by the size of the zone that can be taken outside the stability field. Two cases are analyzed: homogeneous spherical flow conditions and layered leaky aquifer. Close form solutions predict the size of the affected zone within 15% values estimated with complex numerical simulators.
- The analytical solutions show the interplay between the variables: relative sediment permeabilities $k_{\text{sed}}/k_{\text{hbs}}$, the leakage in the aquifer k'/k_{sed} , relative pressure dissociation $(h^* - h_w)/(h_{\text{far}} - h^*)$ and a geometrical ratio $H b/r_w^2$.
- Results reflect the complexity of gas recovery from deep sediments included limited affected zone, large changes in effective stress and associated reductions in permeability.

CHAPTER 7

CONCLUSIONS

The purpose of this thesis is to gain fundamental understanding of hydrate bearing sediments as a potential energy source. To this end, part of this study was devoted to develop unprecedented devices for hydrate bearing sediment characterization under in-situ pressure, temperature and effective stress conditions, sampling effects and gas production implications. In addition to pressure core technology, index properties from disturbed samples and in-situ testing are needed to conduct a comprehensive study of methane hydrate bearing sediments.

The key insights from this work are presented below:

Sampling and coring effects:

- A correct design of coring equipment is critical to guarantee good samples. The internal gap determines the balance between lateral relaxation and wall friction.
- In the context of hydrate bearing sediments, plugging should be expected during coring. As a first estimation, recoverable length of $z/r_s = 10-15$ is advised.
- Soil-sampler interaction parameters affect the predicted plugging length.

Pressure Core Technology:

- Pressure core technology is needed for the proper evaluation of natural hydrate bearing sediments.
- The PCCTs described allow the manipulation, sub-sampling, and extensive assessment of natural gas hydrate bearing sediments under in situ pressure, temperature, and effective stress conditions.
- In addition to pressure core testing, comprehensive characterization programs

should include testing on remolded specimens and in-situ characterization.

- Pressure core technology can also be deployed to study other gas rich hydrocarbon formations such as deep sea sediments, coal bed methane and gas shales.

Nankai Trough Deployment of the DSC:

- The DSC was first deployed to test pressure cores from the Nankai Trough. These hydrate bearing sediments, recovered during the July 2012 expedition were tested to determine P-wave velocity, shear strength, compressibility, relaxation, gas saturation and volume contraction upon dissociation.
- The results obtained with the DSC tend to be lower values compared with the published literature. The discrepancy may be due to the core disturbances during sampling and biased sample preparation practices used to reform hydrate.
- Deliberate steps must be taken to prevent fines migration/removal in laboratory tests as well as field production studies.
- Data gathered with pressure core characterization tools play a central role for hydrate bearing sediments. Additional information is gained from borehole logging measurements (in-situ tests – Chapter 5) and through post decompression sediment analyses including index properties.

In-situ tool characterization:

- The prototype currently available can measure: insertion force, temperature, hydraulic conductivity, fluid sampling, production test, gas extraction and electrical conductivity. The device can readily accommodate modules to determine: stiffness, thermal conductivity, and sediment video/photography. Samplers are included.
- It can be deployed in a wide range of seafloor and reservoir conditions, with

emphasis on hydrate bearing sediments.

- Its modular structure is specifically selected for versatility and adaptation.

Gas Production Implications:

- Gas production by depressurization is limited by the size of the zone that can be taken outside the stability field.
- The analytical solutions show the interplay between the variables: relative sediment permeabilities k_{sed}/k_{hbs} , the leakage in the aquifer k'/k_{sed} , relative pressure dissociation $(h^* - h_w)/(h_{far} - h^*)$ and a geometrical ratio $H b/r_w^2$.
- Results reflect the complexity of gas recovery from deep sediments included limited affected zone, large changes in effective stress and associated reductions in permeability.

REFERENCES

- Abegg, F., Hohnberg, H.-J., Pape, T., Bohrmann, G., and Freitag, J. (2008). "Development and application of pressure-core-sampling systems for the investigation of gas-and gas-hydrate-bearing sediments." *Deep Sea Research Part I: Oceanographic Research Papers*, 55(11), 1590-1599.
- Amann, H., Hohnberg, H., and Reinelt, R. (1997). "HYACE—a novel autoclave coring equipment for systematic offshore gashydrate sampling Deutsche Wissenschaftliche Gesellschaft für Erdgas und Kohle eV (DGMK)." Report, 9706, 37-49.
- Amundsen, T., Lunne, T., Christophersen, H., Bayne, J., and Barnwell, C. (1985). Advanced deep-water soil investigation at the Troll East Field. Proc. of International Conference Advances in Underwater Technology and Offshore Engineering, 3, 165-168
- Anderson, B. J., Wilder, J. W., Kurihara, M., White, M. D., Moridis, G. J., Wilson, S. J., Pooladi-Darvish, M., Masuda, Y., Collett, T. S., and Hunter, R. (2008). "Analysis of modular dynamic formation test results from the Mount Elbert 01 stratigraphic test well, Milne Point Unit, North Slope, Alaska." 6th International Conference on Gas Hydrates (ICGH 2008) Vancouver, British Columbia, Canada.
- American Society for Testing Materials (2008), ASTM D6519, "Standard Practice for Sampling of Soil Using the Hydraulically Operated Stationary Piston Sampler." West Conshohocken, PA.
- American Society for Testing Materials (2008), ASTM D1587, "Standard Practice for Thin-Walled Tube Sampling of Soils for Geotechnical Purposes." West Conshohocken, PA.
- Baligh, M. M. (1985). "Strain path method." *Journal of Geotechnical Engineering*, 111(9), 1108-1136.
- Baligh, M. M., Azzouz, A. S., and Chin, C.-T. (1987). "Disturbances due to "ideal" tube sampling." *Journal of Geotechnical Engineering*, 113(7), 739-757.

- Berg, A. (1984). "Developments in static cone penetrometry of the seabed." *Underwater Systems Design*, 6(5), 28-31.
- Blackwell, J. (1954). "A Transient- Flow Method for Determination of Thermal Constants of Insulating Materials in Bulk Part I—Theory." *Journal of Applied Physics*, 25(2), 137-144.
- Bogges, R., and Robertson, P. "CPT for soft sediments and deepwater investigations." *CPT'10: 2nd International Symposium on Cone Penetration Testing*, Huntington Beach, CA.
- Boswell, R., and Collett, T. S. (2011). "Current perspectives on gas hydrate resources." *Energy & Environmental Science*, 4(4), 1206-1215.
- Brucy, F., Meunier, J., and Nauroy, J. "Behavior of pile plug in sandy soils during and after driving." *Proc., 23rd Annual Offshore Technology Conference*, 145-154.
- Budhu, M., and Wu, C. S. (1992). "Numerical analysis of sampling disturbances in clay soils." *International journal for numerical and analytical methods in geomechanics*, 16(7), 467-492.
- Bureau of Ocean Energy and Management -BOEM- (2012). "Assessment of In-Place Gas Hydrate Resources of the Lower 48 United States Outer Continental Shelf." BOEM, 4.
- Burns, S., and Mayne, P. (1998). "Penetrometers for soil permeability and chemical detection." Report No. GIT-CEECEO-98-1, Georgia Institute of Technology, 144.
- Burns, S. E., and Mayne, P. W. (2002). "Interpretation of seismic piezocone results for the estimation of hydraulic conductivity in clays." *ASTM geotechnical testing journal*, 25(3), 334-341.
- Carroll, J. (2009). *Natural gas hydrates: a guide for engineers*, Gulf Professional Publishing, London.
- Chartier, M. G. (2005). "The design and field evaluation of a new dual pressure and temperature tapered probe." Master of Science, Massachusetts Institute of Technology, Boston.

- Chirlin, G. R. (1989). "A critique of the Hvorslev method for slug test analysis: The fully penetrating well." *Groundwater Monitoring & Remediation*, 9(2), 130-138.
- Cho, G. C., Lee, J. S., and Santamarina, J. C. (2004). "Spatial Variability: High-resolution Assessment with Electrical Needle Probe." *Geotechnical and Geoenvironmental Engineering*, 130(8), 843-850.
- Chung, S. F., Randolph, M. F., and Schneider, J. A. (2006). "Effect of penetration rate on penetrometer resistance in clay." *Journal of geotechnical and geoenvironmental engineering*, 132(9), 1188-1196.
- Clarke, B. G. (1994). *Pressuremeters in geotechnical design*, Blackie Academic & Professional, London.
- Clayton, C., and Siddique, A. (1999). "Tube sampling disturbance—forgotten truths and new perspectives." *Proceedings of the ICE-Geotechnical Engineering*, 137(3), 127-135.
- Clayton, C., Siddique, A., and Hopper, R. (1998). "Effects of sampler design on tube sampling disturbance—numerical and analytical investigations." *Geotechnique*, 48(6), 847-867.
- Clayton, C. R., Simons, N. E., and Matthews, M. C. (1995). *Site investigation*, Blackwell Science, Oxford.
- Coddington, E. A. (1961). *An introduction to ordinary differential equations*, Prentice-Hall Inc., New Jersey.
- Collett, T. S., and Lee, M. W. (2011). "Downhole well log characterization of gas hydrates in nature—a review." *Manuscript*, 203, 17-22.
- Cortes, D. D., Martin, A. I., Yun, T. S., Francisca, F. M., Santamarina, J. C., and Ruppel, C. (2009). "Thermal conductivity of hydrate-bearing sediments." *Journal of Geophysical Research: Solid Earth*, 114(B11).
- Dallimore, S. R., Wright, J. F., Nixon, F. M., Kurihara, M., Yamamoto, K., Fujii, T., Fujii, K., Numasawa, M., Yasuda, M., and Imasato, Y. "Geologic and porous media factors affecting the 2007 production response characteristics of the JOGMEC/NRCAN/AURORA Mallik Gas Hydrate Production Research Well."

Proc., Proceedings of the 6th International Conference on Gas Hydrates (ICGH 2008), 10.

Darnell, K., Andrews, M., Flemings, P., Germaine, J., Polito, P., and Brooks, D. (2012). "The temperature 2 pressure probe (T2P): Technical Manual." The University of Texas at Austin, Austin, TX, 47.

De Glee, G. (1951). "Berekeningsmethoden voor de winning van grondwater." Drinkwatervoorziening, 3e Vacantiecursus, 38-80.

De Nicola, A., and Randolph, M. (1997). "The plugging behaviour of driven and jacked piles in sand." *Geotechnique*, 47(4), 841-856.

DeGroot, D. J. (2003) "Laboratory measurement and interpretation of soft clay mechanical behavior." Proc., Proceedings of the 2001 Ladd Symposium on Soil Behavior and Soft Ground Construction, ASCE, 167-200.

DeJong, J.T. and Frost, J.D. (2002). "A multisleeve friction attachment for the cone penetrometer." *Geotechnical Testing Journal*, 25(2), 111-127.

Denver, H., and Riis, H. "CPT offshore rig." Proc., Proc. 11th Nordic Geotechnical Meeting, , 261-266.

Díaz-Rodríguez, J. A., Martínez-Vasquez, J. J., and Santamarina, J. C. (2009). "Strain-rate effects in Mexico City soil." *Journal of geotechnical and geoenvironmental engineering*, 135(2), 300-305.

Dickens, G. R., Schroeder, K. U., Hinrichs, and Party, L. S. (2003) "The Pressure Core Sampler (PCS) on ODP Leg201: General operations and gas release." Proc., Proceedings of the Ocean Drilling Program, Initial Reports, 1-22.

Eide, O. (1974). "Marine soil mechanics." Report No. 103, NGI, Oslo.

Elsewort, D and Lee, D.S. (2005). "Permeability determination from on-the-fly piezocone sounding". *Journal of Geotechnical and Geoenvironmental Engineering*, 131(5), 643-653.

- Esmailzadeh, F., Zeighami, M. E., and Kaljahi, J. F. (2011). "1-D Mathematical Modeling of Hydrate Decomposition in Porous Media by Depressurization and Thermal Stimulation." *Journal of Porous Media*, 14(1).
- Farouki, O. T. (1981). "Thermal properties of soils." U.S. Army Cold Regions Research and Engineering Laboratory, Hanover, NH, 151.
- Flemings, P., Long, H., Dugan, B., Germaine, J., John, C., Behrmann, J. H., Sawyer, D., and Expedition, I. (2008). "Pore pressure penetrometers document high overpressure near the seafloor where multiple submarine landslides have occurred on the continental slope, offshore Louisiana, Gulf of Mexico." *Earth and Planetary Science Letters*, 269(3), 309-325.
- Freudenthal, T., and Wefer, G. (2007). "Scientific drilling with the sea floor drill rig MeBo." *Scientific Drilling*, 5, 63-66.
- Frost, J.D. and DeJong J.T. (2005). "In situ assessment of role of surface roughness on interface response." *Journal of Geotechnical and Geoenvironmental Engineering*, 131 (4), 498-511.
- Fujii, T., Noguchi, S., Takayama, T., Suzuki, K., Yamamoto, K., and Saeki, T. "Site Selection and Formation Evaluation at the 1st Offshore Methane Hydrate Production Test Site In the Eastern Nankai Trough, Japan." *Proc., 75th EAGE Conference & Exhibition-Workshops, London.*
- Fujii, T., Saeki, T., Kobayashi, T., Inamori, T., Hayashi, M., Takano, O., Takayama, T., Kawasaki, T., Nagakubo, S., and Nakamizu, M. "Resource assessment of methane hydrate in the Eastern Nankai Trough Japan." *Proc., 6th International Conference on Gas Hydrates (ICGH 2008)*, 68.
- Geise, J., and Kolk, H. (1983). "The Use of Submersible for Geotechnical Investigations". *The Design and Operation of Underwater Vehicles. Paper 7.3 Society for Underwater Technology, London.*
- Goel, N., Wiggins, M., and Shah, S. (2001). "Analytical modeling of gas recovery from in situ hydrates dissociation." *Journal of Petroleum Science and Engineering*, 29(2), 115-127.
- Guide, C.-S. U. s. (2012). "Computer Modeling Group Ltd."

- Hancock, S., Collett, T., Dallimore, S., Satoh, T., Inoue, T., Huenges, E., Hennings, J., and Weatherill, B. (2005). "Overview of thermal-stimulation production-test results for the JAPEX/JNOC/GSC et al. Mallik 5L-38 gas hydrate production research well." Geological Survey of Canada, 135.
- Hawkins, R., and Narkus, A. "New Development in Offshore Geotechnical Investigation." Proc., Proceedings of an International Conference Offshore Site Investigation and Foundation Behaviour, Society of Underwater Technology, 259-276.
- Hermann, W. A. (2006). "Quantifying global exergy resources." *Energy*, 31(12), 1685-1702.
- Hird, C., and Hajj, A. (1995). "A simulation of tube sampling effects on the stiffness of clays." *Geotechnical Testing Journal*, 18(1), 3-14.
- Hong, H., and Pooladi-Darvish, M. (2005). "Simulation of depressurization for gas production from gas hydrate reservoirs." *Journal of Canadian Petroleum Technology*, 44(11), 39-46.
- Hong, H., Pooladi-Darvish, M., and Bishnoi, P. (2003). "Analytical modelling of gas production from hydrates in porous media." *Journal of Canadian Petroleum Technology*, 42(11), 45-56.
- Horng, V., Tanaka, H., and Obara, T. (2010). "Effects of sampling tube geometry on soft clayey sample quality evaluated by nondestructive methods." *Soils and Foundations*, 50(1), 93-107.
- Hryciw, R. D., Ghalib, A., and Raschke, S. A. (1998). "In situ soil characterization using Vision Cone Penetrometer (VisCPT)." 1st. Int. Conf. on Site Characterization (ISC98) Balkema, Rotterdam, Netherlands, 1081-1086.
- Hryciw, R. D., Shin, S., and Ghalib, A. M. "High resolution site characterization by VisCPT with application to hydrogeology." Proc. of the 12th Panamerican Conference on Soil Mechanics and Geotechnical Engineering, 293-298.
- Huey, D. P. (2009). "IODP Drilling and Coring Technology." IODP, ed., Stress Engineering Services, Inc., Houston.

- Hvorslev, M. J. (1949). Subsurface exploration and sampling of soils for civil engineering purposes, US Army Waterways Experiment Station, Vicksburg, Mississippi.
- Hvorslev, M. J. (1951). "Time lag and soil permeability in ground-water observations." Bulletin 36, US Corps of Engineering, Waterways Exp. Station, Vicksburg, Mississippi, 50.
- Hyndman, R., Davis, E., and Wright, J. (1979). "The measurement of marine geothermal heat flow by a multi-penetration probe with digital acoustic telemetry and in-situ thermal conductivity." *Marine Geophysical Researches*, 4(2), 181-205.
- Hyodo, M., Yoneda, J., Nakata, Y., and Yoshimoto, N. "Strength and dissociation property of methane hydrate bearing sand." *Proceedings of the 7th International Conference on Gas Hydrates*.
- Iskander, M. (2011). Behavior of pipe piles in sand. Wu and Borja (eds.), Springer.
- Jang, J., and Santamarina, J. C. (2011). "Recoverable gas from hydrate-bearing sediments: Pore network model simulation and macroscale analyses." *Journal of Geophysical Research: Solid Earth*, 116(B8).
- Jefferies, M., and Been, K. (1987). "Experience with measurement of horizontal geostatic stress in sand during cone penetration test profiling." *Geotechnique*, 37(4), 483-498.
- Ji, C., Ahmadi, G., and Smith, D. H. (2001). "Natural gas production from hydrate decomposition by depressurization." *Chemical Engineering Science*, 56(20), 5801-5814.
- Karim, U. F. (1984). "Large deformation analysis of penetration problems involving piles and sampling tubes in soils." State University of New York at Buffalo, New York.
- Kawasaki, M., Umezu, S., and Yasuda, M. (2006). "Pressure Temperature Core Sampler (PTCS)." *Journal of the Japanese Association for Petroleum Technology*, 71(1).
- Kirsch, G. (1898). "Die theorie der elastizität und die bedürfnisse der festigkeitslehre." *Ver. Deutsch Ingenieure*, 42, 797-807.

- Klar, A., Uchida, S., Soga, K., and Yamamoto, K. (2013). "Explicitly coupled thermal flow mechanical formulation for gas-hydrate sediments." *SPE Journal*, 18(02), 196-206.
- Kleinberg, R., Flaum, C., Griffin, D., Brewer, P., Malby, G., Peltzer, E., and Yesinowski, J. (2003). "Deep sea NMR: Methane hydrate growth habit in porous media and its relationship to hydraulic permeability, deposit accumulation, and submarine slope stability." *Journal of Geophysical Research: Solid Earth* 108(B10).
- Koh, C. A., Sum, A. K., and Sloan, E. D. (2012). "State of the art: natural gas hydrates as a natural resource." *Journal of Natural Gas Science and Engineering*, 8, 132-138.
- Kolk, H., and Wegerif, J. "Offshore Site Investigations: New Frontiers." *Proc., Proceedings of the First International Symposium on Frontiers in Offshore Geotechnics*, 19-21.
- Kolymbas, D. (2005). *Tunnelling and tunnel mechanics: A rational approach to tunnelling*, 2nd edition. Springer, Berlin.
- Konno, Y., Masuda, Y., Hariguchi, Y., Kurihara, M., and Ouchi, H. (2010). "Key factors for depressurization-induced gas production from oceanic methane hydrates." *Energy & Fuels*, 24(3), 1736-1744.
- Kubo, Y., Mizuguchi, Y., Inagaki, F., and Yamamoto, K. (2014). "A new hybrid pressure-coring system for the drilling vessel Chikyu." *Scientific Drilling*, 17, 37-43.
- Kurihara, M., Sato, A., Ouchi, H., Narita, H., Masuda, Y., Saeki, T., and Fujii, T. (2009). "Prediction of gas productivity from Eastern Nankai Trough methane-hydrate reservoirs." *SPE Reservoir Evaluation & Engineering*, 12(03), 477-499.
- Kvenvolden, K., Barnard, L., and Cameron, D. (1983). "Pressure core barrel - Application to the study of gas hydrates, deep-sea project site 533, Leg 76." *Initial Reports of the Deep Sea Drilling Project*, 76, 367-375.
- Kwon, T. H., Cho, G. C., and Santamarina, J. C. (2008). "Gas hydrate dissociation in sediments: Pressure- temperature evolution." *Geochemistry, Geophysics, Geosystems*, 9(3).

- Ladd, C., and DeGroot, D. "Recommended practice for soft ground site characterization: Arthur Casagrande Lecture." Proc., Proceedings of the 12th Pan American Conference on Soil Mechanics and Geotechnical Engineering, MIT, Cambridge, Mass.
- Ladd, C. C., and Foott, R. (1974). "New design procedure for stability of soft clays." *Journal of the Geotechnical Engineering Division*, 100(7), 763-786.
- Lee, J., Schultheiss, P., Druce, M., and Lee, J. (2009). "Pressure core sub sampling for GH production tests at in situ effective stress." *Fire in the Ice*, 9(4), 16-17.
- Lee, J., Yun, T., Santamarina, J., and Ruppel, C. (2007). "Observations related to tetrahydrofuran and methane hydrates for laboratory studies of hydrate-bearing sediments." *Geochemistry, Geophysics, Geosystems*, 8(6).
- Lee, J.-S., and Santamarina, J. C. (2005). "Bender elements: performance and signal interpretation." *Journal of Geotechnical and Geoenvironmental Engineering*, 131(9), 1063-1070.
- Lee, J.-S., and Santamarina, J. C. (2005). "P-wave reflection imaging." *Geotechnical Testing Journal*, 28(2), 197-206.
- Leong, E., and Randolph, M. (1991). "Finite element analyses of soil plug response." *International Journal for Numerical and Analytical Methods in Geomechanics*, 15(2), 121-141.
- Li, G., Moridis, G. J., Zhang, K., and Li, X.-S. (2010). "Evaluation of gas production potential from marine gas hydrate deposits in Shenhu area of South China Sea." *Energy & Fuels*, 24(11), 6018-6033.
- Li, X., Holland, J., Wang, G., and Roblee, C. (1997). "Analysis of stress-change disturbance caused by ideal drilling in clay." *Journal of Geotechnical and Geoenvironmental Engineering*, 123(7), 626-634.
- Li, X.-S., Yang, B., Li, G., and Li, B. (2012). "Numerical simulation of gas production from natural gas hydrate using a single horizontal well by depressurization in Qilian Mountain permafrost." *Industrial & Engineering Chemistry Research*, 51(11), 4424-4432.

- Lightner, E., and Purdy, C. (1995) "Cone penetrometer development and testing for environmental applications." *Proceedings of International Symposium on Cone Penetration Testing*, 2, 41-48.
- Liu, L., Jiang, G. S., Ning, F. L., Yu, Y. B., Zhang, L., and Tu, Y. Z. (2012). "Well Logging in Gas Hydrate-Bearing Sediment: A Review." *Advanced Materials Research*, 524, 1660-1670.
- Long, M. (2002). "The quality of continuous soil samples." *ASTM Geotechnical Testing Journal*, 25(3), 234-253.
- Long, M. (2003) "Sampling disturbance in soft laminated clay." *Proc. Inst. Civ. Eng. Geotech Eng.*, 156, 213-224.
- Lunne, T. "The CPT in offshore soil investigations-a historic perspective." *Proc., 2nd International symposium on cone penetration testing (CPT'10)*, www.cpt10.com.
- Lunne, T., Andersen, K. H., Low, H. E., Randolph, M. F., and Sjørsen, M. (2011). "Guidelines for offshore in situ testing and interpretation in deepwater soft clays." *Canadian Geotechnical Journal*, 48(4), 543-556.
- Lunne, T., and Long, M. (2006). "Review of long seabed samplers and criteria for new sampler design." *Marine Geology*, 226(1), 145-165. Mathias, S., and Butler, A. (2006). "An improvement on Hvorslev's shape factors." *Geotechnique*, 56(10), 705-706.
- Matsumoto, R., Tomaru, H., and Lu, H. (2004). "Detection and evaluation of gas hydrates in the eastern Nankai Trough by geochemical and geophysical methods." *Resource Geology*, 54(1), 53-67.
- Mayne, P. W. "Stress-strain-strength-flow parameters from enhanced in-situ tests." *Proc., Int. Conf. on In Situ Measurement of Soil Properties and Case Histories*, 27-47.
- McClelland, B. (1975). "Trends in marine site investigations: A perspective." *Offshore Europe Conference*, Spearhead Publications, Aberdeen.
- Meunier, J., Sangouard, D., and Lhuillier, B. (2000) "A new seabed penetrometer." *Proc., Offshore Technology Conference*. Paper 12095.

- Meyer, B. J., Harman, D. E., and King, P. G. (1982) "Introduction of a New Offshore Cone Penetrometer (CPT) Device for the Gulf of Mexico." Proc., Offshore Technology Conference, 10-16.
- Miyazaki, K., Masui, A., Sakamoto, Y., Aoki, K., Tenma, N., and Yamaguchi, T. (2011). "Triaxial compressive properties of artificial methane hydrate bearing sediment." Journal of Geophysical Research: Solid Earth, 116(B6).
- Miyazaki, T. (2005). Water flow in soils, Taylor and Francis, London.
- Moridis, G., and Collett, T. (2003). "Strategies for gas production from hydrate accumulations under various geologic conditions." Lawrence Berkeley National Laboratory, Lawrence Berkeley National Laboratory, Berkeley, CA.
- Moridis, G. J. (2014). "TOUGH+ HYDRATE v1. 2 User's Manual: A Code for the Simulation of System Behavior in Hydrate-Bearing Geologic Media." R. LBNL-3185, ed., Lawrence Berkeley National Laboratory, Berkeley, CA.
- Moridis, G. J., Collett, T., Boswell, R., Kurihara, M., Reagan, M. T., Koh, C., and Sloan Jr, E. D. (2008). "Toward production from gas hydrates: current status, assessment of resources, and simulation-based evaluation of technology and potential." SPE 114163, Keystone, Colo.
- Moridis, G. J., Collett, T., Pooladi-Darvish, M., Hancock, S., Santamarina, J. C., Boswell, R., Kneafsey, T. J., Rutqvist, J., Kowalsky, M. B., Reagan, M. T., Sloan Jr, E. D., Sum, A. K., and Koh, C. (2011). "Challenges, uncertainties and issues facing gas production from gas hydrate deposits." SPE Reservoir Evaluation & Engineering, 14(1), 76-112.
- Moridis, G. J., Collett, T. S., Dallimore, S. R., Satoh, T., Hancock, S., and Weatherhill, B. (2002). "Numerical simulation studies of gas production scenarios from hydrate accumulations at the Mallik Site, McKenzie Delta, Canada." 4th Int.Conf. Gas Hydrates, 239-244.
- Moridis, G. J., Kim, J., Reagan, M. T., and Kim, S.-J. (2013). "Feasibility of gas production from a gas hydrate accumulation at the UBGH2-6 site of the Ulleung basin in the Korean East Sea." Journal of Petroleum Science and Engineering, 108, 180-210.

- Moridis, G. J., Kowalsky, M. B., and Pruess, K. (2007). "Depressurization-induced gas production from class-1 hydrate deposits." *SPE Reservoir Evaluation & Engineering*, 10(5), 458-481.
- Moridis, G. J., and Sloan, E. D. (2007). "Gas production potential of disperse low-saturation hydrate accumulations in oceanic sediments." *Energy Conversion and Management*, 48(6), 1834-1849.
- Murff, J., Raines, R., and Randolph, M. (1990) "Soil plug behavior of piles in sand." *Proc., 22nd Offshore Technology Conference*, 25-32.
- Muskat, M. (1965). *Flow of homogeneous fluids*. JW Edwards, J.W. Edwards Inc., Ann Arbor, Michigan.
- Myshakin, E. M., Gaddipati, M., Rose, K., and Anderson, B. J. (2012). "Numerical simulations of depressurization-induced gas production from gas hydrate reservoirs at the Walker Ridge 313 site, northern Gulf of Mexico." *Marine and Petroleum Geology*, 34(1), 169-185.
- Noguchi, S., Shimoda, N., Takano, O., Oikawa, N., Inamori, T., Saeki, T., and Fujii, T. (2011). "3-D internal architecture of methane hydrate-bearing turbidite channels in the eastern Nankai Trough, Japan." *Marine and Petroleum Geology*, 28(10), 1817-1828.
- O'Neill, D., Baldi, G., and Della Torre, A. (1996) "The multifunctional Envirocone test system." *Proc., International Conference of Advances in Site Investigation Practice*, 421-437.
- Paik, K., Salgado, R., Lee, J., and Kim, B. (2003). "Behavior of open-and closed-ended piles driven into sands." *Journal of Geotechnical and Geoenvironmental Engineering*, 129(4), 296-306.
- Paikowsky, S. (1990) "The mechanism of pile plugging in sand." *Proc., 22nd Offshore Technology Conference*, 4, 593-604.
- Paikowsky, S. G., and Whitman, R. V. (1990). "The effects of plugging on pile performance and design." *Canadian Geotechnical Journal*, 27(4), 429-440.

- Paikowsky, S. G., Whitman, R. V., and Baligh, M. M. (1989). "A new look at the phenomenon of offshore pile plugging." *Marine Georesources & Geotechnology*, 8(3), 213-230.
- Parkes, R. J., Sellek, G., Webster, G., Martin, D., Anders, E., Weightman, A. J., and Sass, H. (2009). "Culturable prokaryotic diversity of deep, gas hydrate sediments: first use of a continuous high- pressure, anaerobic, enrichment and isolation system for seafloor sediments (DeepIsoBUG)." *Environmental microbiology*, 11(12), 3140-3153.
- Pasten, C., and Santamarina, J. C. (2012). "Energy and quality of life." *Energy Policy*, 49, 468-476.
- Pennington, D., and Kelleher, P. (2007). "PROD Delivers an Accurate Site Investigation at Maari." *SUT Conference, Offshore Site Investigation and Geotechnics*, 81-90.
- Peterson, L., and Johnson, G. (1985) "Deep water site investigations." *Proc. 3rd Offshore Technology Conference*.
- Pettigrew, T. (1992). "Design and operation of a wireline pressure core sampler (PCS)." *Technical Note No. 17, Ocean drilling progr., T. A.& M. Univ.*
- Peuchen, J. (2012). "Site characterization in nearshore and offshore geotechnical projects." *Geotechnical and Geophysical Site Characterization*, 1, 83-111.
- Peuchen, L., and Raap, C. (2007) "Logging, Sampling, and Testing for Offshore Geohazards." *Proc., Offshore Technology Conference 2007*, 30-35.
- Pfender, M., and Villinger, H. (2002). "Miniaturized data loggers for deep sea sediment temperature gradient measurements." *Marine Geology*, 186(3), 557-570.
- Pinero, E., Marquardt, M., Hensen, C., Haeckel, M., and Wallmann, K. (2013). "Estimation of the global inventory of methane hydrates in marine sediments using transfer functions." *Biogeosciences*, 10(2), 959-975.
- Pooladi-Darvish, M. (2004). "Gas production from hydrate reservoirs and its modeling." *Journal of Petroleum Technology*, 56(6), 65-71.

- Power, P., and Geise, J. (1994) "Offshore soil investigation techniques and equipment for the next century." Proc., Proceedings of BOSS'94 Behaviour of Offshore Structures Conference, 97-109.
- Qin, H., Gu, L., Li, S., Zhu, L., and Chen, Y. (2005). "Pressure Tight Piston Corer--A New Approach on Gas Hydrate Investigation." *China Ocean Engineering*, 19(1), 121-128.
- Randolph, M., Leong, E., and Houlsby, G. (1991). "One-dimensional analysis of soil plugs in pipe piles." *Geotechnique*, 41(4), 587-598.
- Randolph, M. F. (2012). "Offshore Geotechnics--the Challenges of Deepwater Soft Sediments." *Geotechnical Engineering State of the Art and Practice: Keynote Lectures from GeoCongress 2012(226)*, 241.
- Randolph, M. F., Gaudin, C., Gourvenec, S. M., White, D. J., Boylan, N., and Cassidy, M. J. (2011). "Recent advances in offshore geotechnics for deep water oil and gas developments." *Ocean Engineering*, 38(7), 818-834.
- Raschke, S. A., and Hryciw, R. D. (1997). "Vision cone penetrometer for direct subsurface soil observation." *Journal of Geotechnical and Geoenvironmental Engineering*, 123(11), 1074-1076.
- Reichel, N., Evans, M., Allioli, F., Mauborgne, M.-L., Nicoletti, L., Haranger, F., Laporte, N., Stoller, C., Cretoiu, V., and El Hehiawy, E. (2012) "Neutron Gamma Density (NGD): Principles, field test results and log quality control of radioisotope-free bulk density measurement." Proc., SPWLA 53rd Annual Logging Symposium, 16-20.
- Robertson, P., and Cabal, K. (2010). "Guide to cone penetration testing for geotechnical engineering." Gregg Drilling and Testing Inc.
- Robertson, P., Lunne, T., and Powell, J. (1996) "Applications of penetration tests for geo-environmental purposes." C. Craig (Ed.), *Advances in site investigation practice*. Thomas Telford Publishing, London, 407-420.
- Rochelle, P. L., Sarrailh, J., Tavenas, F., Roy, M., and Leroueil, S. (1981). "Causes of sampling disturbance and design of a new sampler for sensitive soils." *Canadian Geotechnical Journal*, 18(1), 52-66.

- Rogers, J. D. (2006). "Subsurface exploration using the standard penetration test and the cone penetrometer test." *Environmental & Engineering Geoscience*, 12(2), 161-179.
- Rosenbaum, E. J., English, N. J., Johnson, J. K., Shaw, D. W., and Warzinski, R. P. (2007). "Thermal conductivity of methane hydrate from experiment and molecular simulation." *The Journal of Physical Chemistry*, 111(46), 13194-13205.
- Ruppel, C. (2003). "Thermal state of the gas hydrate reservoir." *Natural Gas Hydrate*, Springer, 29-42.
- Sacchetto, M., Trevisan, A., Elmgren, K., and Melander, K. (2004). "CPTWD (Cone Penetration Test While Drilling) a new method for deep geotechnical surveys." *Proc. ISC-2 on Geotechnical and Geophysical Site Characterization*, V. d. F. Mayne, ed., 787.
- Safaqah, O., and Riemer, M. (2006). "Minimizing sampling disturbance using a new in situ device." *Soil Dynamics and Earthquake Engineering*, 26(2), 153-161.
- Santagata, M., and Germaine, J. (2002). "Sampling disturbance effects in normally consolidated clays." *Journal of Geotechnical and Geoenvironmental Engineering*, 128(12), 997-1006.
- Santagata, M., and Germaine, J. T. (2005). "Effect of OCR on sampling disturbance of cohesive soils and evaluation of laboratory reconsolidation procedures." *Canadian Geotechnical Journal*, 42(2), 459-474.
- Santamarina, J., and Jang, J. (2009). "Gas production from hydrate bearing sediments: geomechanical implications." *DOE-NETL Fire in the Ice*, 9(4), 18-22.
- Santamarina, J. C., Dai, S., Jang, J., and Terzariol, M. (2012). "Pressure core characterization tools for hydrate-bearing sediments." *Scientific Drilling*, 14, 44-48.
- Schmertmann, J. H., and Palacios, A. (1979). "Energy dynamics of SPT." *Journal of the Geotechnical Engineering Division*, 105(8), 909-926.

- Schultheiss, P., Francis, T., Holland, M., Roberts, J., Amann, H., Parkes, R., Martin, D., Rothfuss, M., Tyunder, F., and Jackson, P. (2006). "Pressure coring, logging and subsampling with the HYACINTH system." *New Techniques in Sediment Core Analysis*, R. G, ed., Geological Society, Special Publications 267, London, 151-163.
- Schultheiss, P., Holland, M., and Humphrey, G. (2009). "Wireline coring and analysis under pressure: Recent use and future developments of the HYACINTH system." *Scientific Drilling*, 7, 44-50.
- Shankar, U., and Riedel, M. (2011). "Gas hydrate saturation in the Krishna–Godavari basin from P-wave velocity and electrical resistivity logs." *Marine and Petroleum Geology*, 28(10), 1768-1778.
- Shelton, J. T. "OMNI-Maxtrade anchor development and technology." *Proc., Oceans Conference, IEEE*, 1900-1999.
- Siddique, A., Clayton, C., and Hopper, R. (1999). "The effect of varying the centerline tube sampling disturbance on the behavior of reconstituted clay." *Geotechnical Testing Journal*, 22(3), 245-256.
- Skempton, A., and Sowa, V. (1963). "The behaviour of saturated clays during sampling and testing." *Geotechnique*, 13(4), 269-290.
- Sloan Jr, E. D., and Koh, C. (2007). *Clathrate hydrates of natural gases*, Marcel Dekker, New York.
- Steiner, A., L'Heureux, J.-S., Kopf, A., Vanneste, M., Longva, O., Lange, M., and Haflidason, H. (2012). "An in-situ free-fall piezocone penetrometer for characterizing soft and sensitive clays at Finneidfjord (northern Norway)." *Submarine mass movements and their consequences*, Springer, 99-109.
- Stokoe, K. H., and Santamarina, J. C. (2000) "Seismic-wave-based testing in geotechnical engineering." *Proc., GeoEng 2000, International Society for Rock Mechanics*, 1490-1536.
- Stone, H. (1970). "Probability model for estimating three-phase relative permeability." *Journal of Petroleum Technology*, 22(02), 214-218.

- Su, Z., He, Y., Wu, N., Zhang, K., and Moridis, G. J. (2012). "Evaluation on gas production potential from laminar hydrate deposits in Shenhu Area of South China Sea through depressurization using vertical wells." *Journal of Petroleum Science and Engineering*, 86, 87-98.
- Sun, Y., Goldberg, D., Collett, T., and Hunter, R. (2011). "High-resolution well-log derived dielectric properties of gas-hydrate-bearing sediments, Mount Elbert Gas Hydrate Stratigraphic Test Well, Alaska North Slope." *Marine and Petroleum Geology*, 28(2), 450-459.
- Tanaka, H. (2000). "Sample quality of cohesive soils: lessons from three sites, Ariake, Bothkennar and Drammen." *Soils and Foundations*, 40(4), 57-74.
- Tanaka, H., Ritoh, F., and Omukai, N. (2002). "Quality of samples retrieved from great depth and its influence on consolidation properties." *Canadian Geotechnical Journal*, 39(6), 1288-1301.
- Tang, X., Dubinsky, V., Wang, T., Bolshakov, A., and Patterson, D. (2003). "Shear-velocity measurement in the logging-while-drilling environment: modeling and field evaluations." *Petrophysics*, 44(2), 79-89.
- Torstensson, B. A. (1984). "A new system for ground water monitoring." *Groundwater Monitoring & Remediation*, 4(4), 131-138.
- Tsuji, Y., Fujii, T., Hayashi, M., Kitamura, R., Nakamizu, M., Ohbi, K., Saeki, T., Yamamoto, K., Namikawa, T., and Inamori, T. (2009). "Methane-hydrate occurrence and distribution in the eastern Nankai Trough, Japan: Findings of the Tokai-oki to Kumano-nada methane-hydrate drilling program." *Natural Gas Hydrates – Energy Resource Potential and Associated Geologic Hazards: AAPG Memoir*, A. J. T. Collett, C. Knapp, R. Boswell (Eds.), ed., 228–246.
- Tsytkin, G. G. (2000). "Mathematical models of gas hydrates dissociation in porous media." *Annals of the New York Academy of Sciences*, 912(1), 428-436.
- Ullerich, J., Selim, M., and Sloan, E. (1987). "Theory and measurement of hydrate dissociation." *AIChE Journal*, 33(5), 747-752.
- Vermeiden, J. (1977). "The diving bell." Report. Delft Soil Mechanics, Laboratory.

- Von Herzen, R., and Maxwell, A. (1959). "The measurement of thermal conductivity of deep- sea sediments by a needle probe method." *Journal of Geophysical Research*, 64(10), 1557-1563.
- Waite, W. F., Santamarina, J. C., Cortes, D. D., Dugan, B., Espinoza, D., Germaine, J., Jang, J., Jung, J., Kneafsey, T. J., and Shin, H. (2009). "Physical properties of hydrate- bearing sediments." *Reviews of Geophysics*, 47(4).
- Walsh, M. R., Hancock, S. H., Wilson, S. J., Patil, S. L., Moridis, G. J., Boswell, R., Collett, T. S., Koh, C. A., and Sloan, E. D. (2009). "Preliminary report on the commercial viability of gas production from natural gas hydrates." *Energy Economics*, 31(5), 815-823.
- Webb, J. (1956). "Thermal conductivity of soil." *Nature*, 177:989.
- Wu, N., Yang, S., Zhang, H., Liang, J., Wang, H., and Lu, J. a. (2010) "Gas Hydrate System of Shenhu Area Northern South China Sea: Wire-line Logging Geochemical Results and Preliminary Resources Estimates." Paper 20485. Proc., Offshore Technology Conference.
- Xu, W., and Ruppel, C. (1999). "Predicting the occurrence, distribution, and evolution of methane gas hydrate in porous marine sediments." *Journal of Geophysical Research: Solid Earth*, 104(B3), 5081-5095.
- Yamamoto, K., and Dallimore, S. (2008). "Aurora-JOGMEC-NRCan Mallik 2006-2008 gas hydrate research project progress." *Natural Gas & Oil*, 304, 285-4541.
- Yamamoto, K., Inada, N., Kubo, S., Fujii, T., and Suzuki, K. (2012). "Pressure core sampling in the eastern Nankai Trough." *Natural Gas & Oil*, 304, 285-4541.
- Yun, T., Narsilio, G., Santamarina, J., and Ruppel, C. (2006). "Instrumented pressure testing chamber for characterizing sediment cores recovered at in situ hydrostatic pressure." *Marine Geology*, 229(3), 285-293.
- Yun, T. S., Fratta, D., and Santamarina, J. C. (2010). "Hydrate-Bearing Sediments from the Krishna– Godavari Basin: Physical Characterization, Pressure Core Testing, and Scaled Production Monitoring." *Energy & Fuels*, 24(11), 5972-5983.

- Yun, T. S., Lee, C., Lee, J. S., Bahk, J. J., and Santamarina, J. C. (2011). "A pressure core based characterization of hydrate-bearing sediments in the Ulleung Basin, Sea of Japan (East Sea)." *Journal of Geophysical Research: Solid Earth*, 116(B2).
- Zhu, H., Liu, Q., Wong, G., Xiao, X., Zhu, X., Jiang, Z., and Zhang, D. (2013). "A Pressure and Temperature Preservation System for Gas-hydrate-bearing Sediments Sampler." *Petroleum Science and Technology*, 31(6), 652-662.
- Zimmerman, E. H., Smith, M., and Shelton, J. T. (2009) "Efficient gravity installed anchor for deepwater mooring." *Proc., Offshore Technology Conference*.
- Zuidberg, H. (1975). "Seacalf: A submersible cone penetrometer rig." *Marine Georesources & Geotechnology*, 1(1), 15-32.
- Zuidberg, H., Richards, A., and Geise, J. (1986) "Soil exploration offshore." *Proc., Proceedings Fourth International Geotechnical Seminar, Field Instrumentation and In-situ Measurements*, 3-11.